

# **Laser backscattering imaging in agriculture**

**Dissertation to obtain the doctoral degree of  
Agricultural Sciences (Dr. sc. agr.)**

**Faculty of Agricultural Sciences  
University of Hohenheim**

Institute of Agricultural Engineering

submitted by

Zhangkai Wu

from Hubei, P.R.China

2023

This thesis was accepted as a doctoral thesis (Dissertation) in fulfillment of the regulations to acquire the doctoral degree "Doktor der Agrarwissenschaften" by the Faculty of Agricultural Sciences at University of Hohenheim on 13.12.2023.

Date of the oral examination: 23.02.2024

**Examination Committee**

Chairperson of the oral examination	Prof. Dr. Thilo Streck
Supervisor and Reviewer	Prof. Dr. Joachim Müller
Co-Reviewer	Prof. Dr. Xiongkui He
Additional examiner	Prof. Dr. Stefan Böttinger

*As one droplet of the ocean*

# Acknowledgements

First and foremost, I wish to express profound gratitude towards human civilization. With every piece of knowledge I acquire, I feel an ever-deepening connection to all humans who have ever lived, or will live, in this world. This dissertation, focuses on laser backscattering imaging, is an example of this connection. The principle of laser, stimulated emission, was put forth by Prof. Dr. Albert Einstein. His pioneering research, in turn, was made possible by farmers who contributed to his food. This intricate interconnection is just a small representation of our vast human web of relationships. While our individual lives span approximately a hundred years, we are also part of a civilization that extends across thousands. We enjoy beautiful music composed by renowned artists, benefit from a robust food supply chain, and relish the warmth of sunlight, knowing it is a product of nuclear fusion within the sun. This realization imbues me with a profound sense of gratitude and good fortune for being a part of the human race. I find it rewarding to continue learning from our civilization, to strive to improve our world, and to extend this bounty and gratitude to our future generations.

My esteemed supervisor, Prof. Dr. Joachim Müller, once expressed his wish not to make the world worse. Although our phrases may differ, these two notions are essentially similar. I am deeply grateful to him for offering me the opportunity to study in our 440e group, and for his guidance and unwavering support throughout my PhD journey.

I extend my thanks to Dr. Klaus Spohrer, my daily supervisor, for his timely assistance and guidance during the most challenging periods of my PhD. My heartfelt appreciation also goes to Sabine Nugent, the secretary of our group, for her support with administrative matters and in personal aspects of my life. Further thanks are due to Dr. Zhichong Wang and Dr. Sebastian Romuli for their valuable suggestions and cooperation during my research.

I am grateful to my office mates Farah Marabet, Yang Zhang, Dr. Victor Torres Toledo, and Dr. Parika Rungpichayapichet for their assistance and camaraderie. Special thanks to Catalina Alejandra Acuña-Gutiérrez for guiding me through the publication process. I am also thankful for my wonderful colleagues: Alice Reineke, Dr. Klaus Meissner, Iris Ramaj, Janvier Ntwali, Ute Waldeck, Olga Gotra, Sarah Fleischmann, Steffen Schock, Dr. Ana Salvatierra-Rojas, Dr. Kiatkamjon Intani, Prof. Dr. Marcus Nagle, Stephanie Tutsch, Leon Oehme, Dr. Shamaila Kan,

Boris Mandrapa, Haimanot Ayele, Sawittree Chai Areekitwat, Dr. Supaporn Klaykruayat, Dr. Adnan Mukhtar, Dr. Toyin Ayetigbo, Dr. Nilobon Komonsing. I sincerely thank you all and feel privileged to be part of such a group.

Special thanks are extended to the China Scholarship Council (CSC) for awarding me a grant to study in Germany.

Finally, my deepest gratitude is reserved for my parents, who have always been by my side, who constantly wish for me to be both happy and healthy. Their enduring love and support are the foundations of my strength.

Zhangkai Wu

---

# Table of Contents

Acknowledgements.....	I
Table of Contents .....	III
List of figures.....	VII
List of tables .....	X
1	
General introduction.....	1
1.1 Non-destructive optical sensor technology (NDOST) in agriculture .....	1
1.2 Laser technology in agriculture .....	2
1.3 Laser backscattering imaging (LBI) in agriculture.....	5
1.3.1 Laser selection .....	6
1.3.2 Image processing .....	6
1.3.3 Prediction models .....	7
1.3.4 Optical parameters.....	8
1.3.5 Applications.....	8
1.4 Prospects and challenges .....	10
1.5 Objectives .....	10
1.6 References .....	11
2	
Investigating the influence of pore size, pore fluid and wavelength on backscattering images with sintered glass filter matrices as experimental models.....	20
2.1 Abstract .....	21
2.2 Introduction.....	21
2.3 Materials and Methods .....	23
2.3.1 Sintered glass matrix.....	23
2.3.2 Chemical solutions .....	24

---

2.3.3	LBI system .....	25
2.3.4	Image analysis .....	26
2.3.5	Statistical analysis .....	29
2.4	Results .....	29
2.4.1	Influence of pore size .....	29
2.4.2	Influence of type and concentration of solute .....	30
2.4.3	Synopsis of pore size, solute and wavelength.....	33
2.5	Discussion .....	36
2.5.1	Backscattering area .....	36
2.5.2	Influencing and non-influencing experimental factors.....	36
2.6	Conclusions.....	39
2.7	References .....	40
3	Investigating crude sesame oil sedimentation and its monitoring using laser backscattering imaging (LBI) .....	44
3.1	Abstract .....	45
3.2	Introduction.....	45
3.3	Materials and Methods .....	47
3.3.1	Sesame Oil.....	47
3.3.2	Experimental Setup for Discontinuous LBI Measurement.....	47
3.3.3	Experimental Setup for Continuous LBI Measurement .....	48
3.3.4	Image Analysis.....	49
3.3.5	Chemical Analysis.....	50
3.3.6	Statistical Analysis .....	50
3.4	Results and Discussion .....	51
3.4.1	Discontinuous LBI Measurement.....	51

---

3.4.2	Continuous LBI Measurement .....	52
3.5	Conclusions.....	58
3.6	References .....	59
4	A novel method for leaf wetness measurement with laser-induced light reflection and RGB imaging.....	64
4.1	Abstract .....	65
4.2	Introduction.....	65
4.3	Materials and methods .....	66
4.3.1	Experiment platform set-up.....	66
4.3.2	Experimental procedure .....	67
4.3.3	Deposition measurement .....	68
4.3.4	Image analysis and features extraction .....	69
4.3.5	Model building.....	70
4.4	Results and discussion.....	70
4.4.1	Droplet size distribution.....	70
4.4.2	Water deposition on the leaves.....	70
4.4.3	Image analysis.....	74
4.4.4	The prediction of <i>LW values</i> .....	78
4.5	Conclusions.....	80
4.6	References .....	81
5	General discussion .....	85
5.1	The effects of pore size and pore fluid on LBI .....	85
5.2	Applying LBI to oil sedimentation process .....	86
5.3	Applying LBI to leaf wetness measurement.....	87
5.4	Conclusion .....	88



5.5 Outlook.....	89
5.6 References .....	90
Summary.....	93
Zusammenfassung .....	95
Annex 3: Declaration in lieu of an oath on independent work.....	98
Curriculum Vitae .....	99

## List of figures

<b>Figure 1.1</b>	Interaction of light with material whose size is much larger than the wavelength (modified from Friebel et al., 2008a).....	2
<b>Figure 1.2</b>	Principle (a) and setup (b) of laser backscattering imaging (LBI) (Mohd Ali et al., 2020b; Qin and Lu, 2009).....	5
<b>Figure 2.1</b>	Approximate pore size distribution of the sintered glass discs ( <i>ROBU GmbH, 2022a</i> ). .....	24
<b>Figure 2.2</b>	Refractive indexes of the matrix of the porous discs (massive glass) used, and of the NaCl and NaH <sub>2</sub> PO <sub>4</sub> aqueous solutions with different concentrations (sodium D line, 20°C) (Haynes, 2014). .....	25
<b>Figure 2.3</b>	Setup of laser backscattering imaging system. ....	26
<b>Figure 2.4</b>	Laser light backscattering imaging (LBI) of a P100 disc saturated with distilled water; (a) original images with identification of area A and transects O-L1, O-L2, O-L3, and O-L4. The average intensity of these four transects was used to plot the histograms; (b) enlargements according to the length of the transects; (c) corresponding intensity profiles of the red, green and blue channel (0-255); and (d) grey value intensity profiles (0-255). The dashed ochre lines mark the ranges of the histograms, the full ochre lines mark the radius of the illuminated area and the corresponding intensity values. ....	28
<b>Figure 2.5</b>	LBI of porous discs of different pore size saturated with distilled water: (a) RGB images of P1.6 – P160; and correlation between backscattering area and pore diameter $P$ ; and intensity profiles for 450 nm (b), 635 nm (c), and 780 nm (d). The logarithm regression lines were estimated omitting P160 as an outlier. RMSE represents root mean square error, RRMSE represents relative root mean square error.....	31
<b>Figure 2.6</b>	(a) Grey value intensity profiles at 635 nm of P100 saturated with NaCl and NaH <sub>2</sub> PO <sub>4</sub> solution with five different concentrations; (b) grey value intensity differences between results obtained with different concentrations and distilled water; and (c) $R^2$ and slope of linear regression between concentration and intensity at different radii, with the solid curve representing $R^2$ and the dotted curve representing slope. ....	32
<b>Figure 2.7</b>	Correlations of backscattering area $A$ and two different saline solutions (NaCl, NaH <sub>2</sub> PO <sub>4</sub> ) with varying concentrations $C$ for five different pore diameters (P1.6 – P160) and three different laser light wavelengths (405, 635, 780 nm). Joint regression equations for both NaCl and NaH <sub>2</sub> PO <sub>4</sub> were given when the slope of NaCl and NaH <sub>2</sub> PO <sub>4</sub> were not significantly different. ....	35

<b>Figure 3.1</b>	(a) The imaging system setup employed for discontinuous LBI (laser backscattering imaging) measurement; (b) the experimental phenomena with clean sesame oil when subjected to red laser illumination. ....	48
<b>Figure 3.2</b>	The system setup used for continuous LBI measurements, with an example image captured by camera 1 and segmented by an $80 \times 80$ pixel box.....	49
<b>Figure 3.3</b>	Backscattering images of oil samples under (a) the 635 nm laser and (b) the 405 nm laser. The crosses in the images indicate the incident points where the laser light entered the surface of the oil. Note that the light from the 635 nm laser transmitted from left to right, reaching the bottom of the container as the oil became cleaner. The 405 nm laser transmitted light from right to left. ....	51
<b>Figure 3.4</b>	Images of the entire tank during the sedimentation process. ....	53
<b>Figure 3.5</b>	Plot of the (a) interface height vs. time and (b) the sedimentation velocity vs. time. ....	53
<b>Figure 3.6</b>	(a) Backscattering images during sedimentation in in situ experiment. (b) Plot of mean grey value of the segmented image vs. time. ....	55
<b>Figure 3.7</b>	(a) Regression between interface height and mean grey value intensity $I_{mean}$ of segmented images. (b) Regression when the interface height is less than 100 mm. ....	56
<b>Figure 4.1</b>	Experimental setup with a balance supporting a leaf, a sprayer used to apply water droplets on the leaf surface and an optical device to measure its wetness. ....	67
<b>Figure 4.2</b>	Experiment procedure. ....	68
<b>Figure 4.3</b>	Droplet size distribution after the 1 <sup>st</sup> spray.....	71
<b>Figure 4.4</b>	Initial mass of a leaf before spraying and the stepwise increase in leaf mass after each of the 6 sprays. The red arrows indicate the times of image acquisition.....	71
<b>Figure 4.5</b>	Leaf area segmented from the laser image ( $A_{leaf}$ ) vs leaf area measured by the scanner ( $A_{reference}$ ).....	72
<b>Figure 4.6</b>	Distribution of the measured leaf wetness ( $LW$ ) values after each spray. ....	73
<b>Figure 4.7</b>	Image of a leaf and zoomed-in view of the marked area with no spray (a) and after the 6 <sup>th</sup> spray (b); (c) The profiles of red channel intensities ( $I_{red}$ ) and green channel intensities ( $I_{green}$ ). ....	75
<b>Figure 4.8</b>	Profiles of the red channel intensity $I_{red}$ of the same leaf area (marked with ellipse) with and without droplet.....	76

---

<b>Figure 4.9</b> Smoothed intensity distributions (moving average of period 9) of a leaf's red channel at different spraying status (0 – 6 sprays). .....	77
<b>Figure 4.10</b> Droplets Identified by image processing on a leaf before spraying (left) and after the 6 <sup>th</sup> spray (right). .....	78
<b>Figure 4.11</b> Prediction results of the GAM model, using different combinations of input image features: (a) $A_{leaf}$ , $I_{red\ mean}$ ; (b) $A_{leaf}$ , $N_{droplet}$ ; (c) $A_{leaf}$ , $I_{red\ mean}$ , $N_{droplet}$ , where $A_{leaf}$ represents image leaf area, $I_{red\ mean}$ represents mean red channel intensity, $N_{droplet}$ represents identified number of droplets. The $R^2$ , RMSE and rRMSE shown in the figures are the average of 1000 times modeling. ....	79

---

## List of tables

Table 1.1	Examples of non-destructive optical sensor technology used in agriculture. ....	3
Table 1.2	Examples of laser technology used in agriculture. ....	4
Table 1.3	Applications of LBI in agriculture since 2017. ....	9
Table 2.1	Pore properties of the sintered glass discs (ROBU GmbH, 2022a, 2022b). ....	24
Table 2.2	Coefficient of determination ( $R^2$ ) for linear relationships between concentration and backscattering area $A$ (data of Figure 2.7). ....	34
Table 2.3	Regression equations for backscattering area $A$ as a function of pore diameter $P$ ( $\mu\text{m}$ ) and refractive index difference RID between solutions and porous disc material. ....	34
Table 2.4	Reported cell sizes found in common horticultural crops: apple, cucumber and potato. ....	34
Table 3.1	Measurement methods used for continuous LBI measurement. ....	50
Table 3.2	Chemical values of sesame oil measured before (Day 0) and after sedimentation (Day 30). ....	57

# 1

## General introduction

### 1.1 Non-destructive optical sensor technology (NDOST) in agriculture

Information collected by sensors plays a fundamental role in both current and future agriculture (King, 2017). In precision farming, information about field spatial and temporal variation is a prerequisite for subsequent applications (Beluhova-Uzunova and Dunchev, 2019). In post-harvest management, product information aids in optimizing the delivery chain and mitigating harmful aspects (Friebel et al., 2008b). NDOST is one of the technologies that collect these information. When compared to traditional chemical analysis, NDOST can save labor, time, and processes (Hussain et al., 2018; S. El-Mesery et al., 2019). Therefore, research about NDOST is essential in the field of agriculture.

The physical principle of NDOST is as follows: a) electromagnetic radiation (EMR) from a light source interacts with a target material (e.g., soil, leaf and fruit), yielding informative EMR output, b) optical sensors receive and convert the EMR into a specific form suitable for human observation and computational analysis. Occasionally, the light source can be omitted if the target material emits its own EMR.

The interaction between the target material and EMR can involve regular reflectance, diffuse reflectance, refraction, and transmission, as illustrated in Figure 1.1. Despite the varied behaviors of EMR, theorems such as the "Ewald–Oseen Extinction" and "Huygens' Principle" suggest that these macro behaviors are underpinned by the same micro-level principles. The scope of these theorems are continually expanded by researchers (Lian, 2018). Furthermore, materials can also emit EMR without an external source of radiation, e.g., thermal radiation. Table 1.1 lists some typical NDOST used in agriculture.

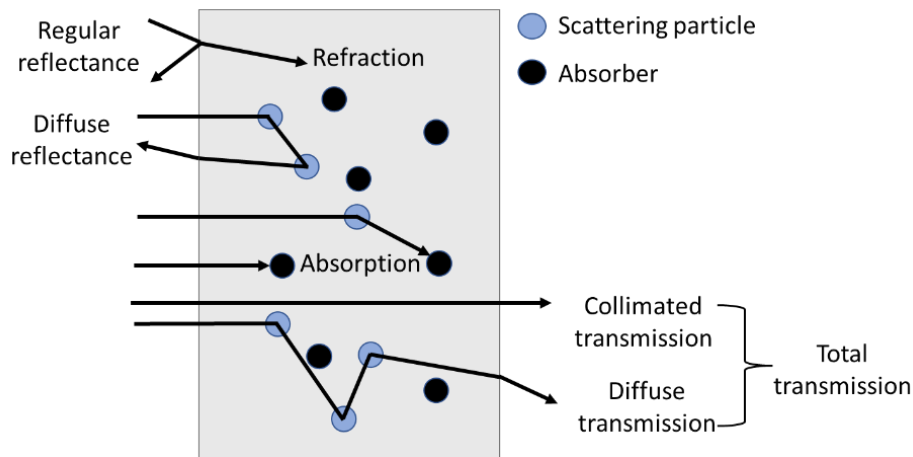


**Figure 1.1** Interaction of light with material whose size is much larger than the wavelength (modified from Friebel et al., 2008a).

## 1.2 Laser technology in agriculture

"Laser" is an acronym for "light amplification by stimulated emission of radiation." The concept of stimulated emission was first proposed theoretically by Einstein (1917). In the 1950s and 1960s, stimulated emission was realized in the microwave and visible light spectrum, respectively, followed by rapid developments of laser technology (Zinth et al., 2011). The application of lasers in agriculture began soon after these inventions (Paleg and Aspinall, 1970).

**Table 1.1 Examples of non-destructive optical sensor technology used in agriculture.**

Technology	Wavelength	Applications	References
Soft X-ray imaging	0.1 – 10 nm	Defect and foreign objects detection	(Banga et al., 2018; Divyanth et al., 2022; Sood et al., 2016)
RGB imaging	400 – 760 nm	Plant protection, classification, ripeness assessment	(Abrougui et al., 2022; Li et al., 2018; Velesaca et al., 2021)
NIR and MIR spectroscopy	0.76 – 25 $\mu$ m	Classification, adulteration, chemical analysis	(Bureau et al., 2019; Tinti et al., 2015; Tsuchikawa et al., 2022)
Thermal imaging	8 - 14 $\mu$ m	Plant status monitoring, yield prediction, irrigation planning	(Ishimwe et al., 2014; Messina and Modica, 2020; Vadivambal and Jayas, 2011)
Microwave imaging	0.01 - 1 m	Food contamination, defect detection, fruit ripeness assessment	(Farina et al., 2019; Ghavami et al., 2021; Korostynska et al., 2018)

Acronyms: NIR, Near-Infrared; MIR, Mid-Infrared.

Laser beams are characterized by their directional accuracy, narrow wavelength range, and high intensity. Due to these unique features, numerous applications based on lasers have been developed for agricultural use. Lasers can be used for food processing tasks such as material pretreatment, microbial inhibition, and marking (Teng et al., 2021). The ability to tune the wavelength of a laser makes it possible to use laser light sources for various types of spectral analysis (Childs et al., 2015; Granzow, 2019; Steinfeld and Zare, 1975). Examples of laser technology can be found in Table 1.2, illustrating the increasing importance of lasers in the field of agriculture.



**Table 1.2 Examples of laser technology used in agriculture.**

<b>Technology</b>	<b>Applications</b>	<b>Destructive or contacting</b>	<b>References</b>
Laser biotechnology	Crop yield and quality increasing	Yes	(Klimek-Kopyra et al., 2021)
Laser induced breakdown spectroscopy	Soil and plant elements detection	Yes	(Yu et al., 2020)
Laser-induced graphene	Soil nitrogen and plant transpiration detection	Yes	(Garland et al., 2018; Lan et al., 2020)
Laser diffraction method	Droplet and soil particle size measurement	No	(Sijs et al., 2021; Yang et al., 2019)
Laser induced fluorescence	Plant nitrogen, adulteration, pollens floating, and food contamination detection	No	(Li et al., 2020; Saito et al., 2018; Wu et al., 2019; Yang et al., 2018)
Laser direct infrared	Soil microplastics and food adulteration identification	No	(da Costa Filho et al., 2020; Jia et al., 2022)
Lidar	Plant phenomics, production estimation, and vehicle navigation	No	(Di Stefano et al., 2021; Iqbal et al., 2020; Jin et al., 2021)
Raman spectroscopy	Adulteration, plant diseases, and pesticide residues detection	No	(Weng et al., 2019, 2021; Yang et al., 2021a)
Laser land leveling	Crop yield and resource efficiencies increasing	No	(Hashimi et al., 2017; Jat et al., 2014)
Biospeckle	Damage or contamination detection, aging, and drying process monitoring	No	(Arefi et al., 2023; Pandiselvam et al., 2020; Rahmanian et al., 2020)

### 1.3 Laser backscattering imaging (LBI) in agriculture

Among all NDOST and laser technology, LBI is considered to be a low-cost technique, making it promising for use in the agricultural field. The fundamental components of this technique include a laser, a camera, and a computer (Figure 1.2). When a laser is pointed at a biological organism or turbid material, the light is scattered inside the material due to its inhomogeneous nature. This scattering creates a distinct light pattern on the surface of the biological material. By analyzing this light pattern, information about the biological organism can be obtained. Studies have reported that factors such as cell size, heterogeneity caused by suspended particles, and cell wall characteristics can influence this scattering phenomenon (McGlone et al., 1997; Nicolai et al., 2007; Qing et al., 2007b). In principle, any structural or compositional changes along the laser path can alter the scattering pattern, potentially resulting in a different surface light pattern.

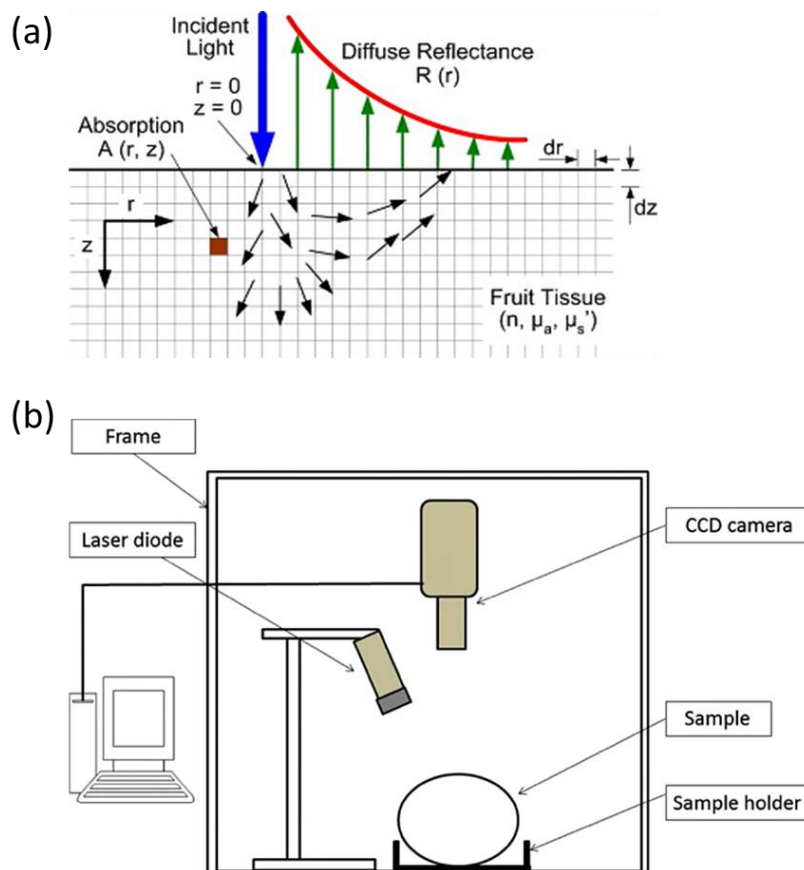


**Figure 1.2** Principle (a) and setup (b) of laser backscattering imaging (LBI) (Mohd Ali et al., 2020b; Qin and Lu, 2009).

### **1.3.1 Laser selection**

As the light source of an LBI system, several critical factors must be considered when selecting a laser. These factors include wavelength, incident angle, and power. A laser emits light at a single wavelength. When bio-organisms interact with lasers, they can produce a strong signal at one wavelength and a weaker signal at another. It is good practice to first use spectral technology or conduct a literature review to determine the sensitive wavelengths of the target object, then decide which wavelengths to use (Qing et al., 2007a; 2008). When economic factors are also a consideration, the market popularity of certain wavelengths should be kept in mind. For instance, a 650 nm laser is more common than a 600 nm laser (Picotronic GmbH, 2023).

The incident angle is generally preferred to be as small as possible to obtain a symmetrical scattering pattern, which is easier to analyze. However, it shouldn't be too small, as the reflectance effect may impact the camera and interfere with signal detection (Hashim et al., 2013). In cases where the analysis does not rely on the symmetry of the laser backscattering pattern, a larger angle could also be chosen (Udomkun et al., 2014). It should also be noted that the incident angle might influence the depth of the laser light traveling inside the bio-organism.

Naturally, higher laser power can result in higher signal intensity. However, the trade-off is that more attention must be paid to safety considerations. There are safety levels that apply to lasers, and depending on their safety levels, specific safety measures must be implemented (DIN EN 60825-1, 2022). As Smalley (2011) pointed out, complacency is the most dangerous factor when using a laser.

### **1.3.2 Image processing**

After capturing the scattering image, image preprocessing techniques can be applied to enhance the signal-to-noise ratio. Although conventional image preprocessing approaches such as median filtering are frequently utilized, LBI in food applications presents a unique challenge: the curvature of the food surface. This curvature can result in image distortion, which arises from two main factors: (i) When laser light is projected from the food surface to

camera, it may be captured by the camera in a way that underestimates the scattering area or intensity. This issue can be addressed by applying the surface integral and the Lambertian cosine law equation (Iida et al., 2023; Qing et al., 2007b). (ii) The curved surface could make the scattered light reach the food surface with shorter path length. This factor is difficult to estimate and is often omitted in current research.

After preprocessing, it is typical to extract features from the backscattering images. Two prevalent methods are employed in LBI: (i) The backscattering image can be segmented into background and the scattering area by a threshold value. Features of the scattering area such as mean intensity and perimeter are then extracted (Mohd Ali et al., 2020a; 2020b; Onwude et al., 2018). (ii) The center of the scattering pattern can be located and a one-dimensional profile can be extracted. Features about this profile can then be extracted (Geng et al., 2019; Lorente et al., 2015; Verdú et al., 2021a).

### **1.3.3 Prediction models**

The goal of prediction models is to establish a mathematical relationship between the numerical features extracted from backscattered images and the target values, such as moisture content or ripeness levels (Núñez et al., 2011). Techniques such as partial least squares regression (PLSR), principal component analysis (PCA), linear discriminant analysis (LDA), and support vector machines (SVM) have recently been widely used in LBI (Table 1.3). MathWorks (2023) suggests that PCA is more suitable for explaining feature variability, while PLSR could use fewer components to build the prediction model. Lately, convolutional neural networks (CNN) have become one of the most popular deep learning models in image analysis (Alzubaidi et al., 2021). The primary advantage of CNN is that they can bypass the feature extraction process and automatically learn the appropriate features to build a model.

It is essential to divide the dataset into a calibration set and a validation set to evaluate the model's performance. The validation process involves assessing the model's performance using specific metrics. Despotovic et al. (2016) used ten metrics to evaluate the quality of a prediction model. Moreover, the mean absolute percentage error (MAPE) is often used when the value to be predicted consistently remains above zero (de Myttenaere et al., 2016). Chicco et al., (2021) suggested that R-squared is a better metric compared to MAPE, mean square

error (MSE), and root mean square error (RMSE) for regression models. For classification model evaluation, the F1 score is also used in addition to accuracy (Yang et al., 2021b).

### **1.3.4 Optical parameters**

There are four optical parameters considered to influence the scattering pattern (Mollazade et al., 2012): refractive index, absorption coefficient, scattering coefficient, and anisotropy factor. The refractive index dictates the extent to which light is bent when it enters different materials. The absorption coefficient and the scattering coefficient determine the probability of light being absorbed or scattered per unit distance. Lastly, the anisotropy factor quantifies the degree to which light retains its forward directionality during a single scattering event.

Currently, scientists typically use two methods to link these optical parameters to backscattering images: the Farrell equation (Lorente et al., 2015; Yang et al., 2021b; Zude-Sasse et al., 2019) and Monte Carlo simulation (Baranyai and Zude, 2008, 2009; Qin and Lu, 2009). The Farrell equation is based on steady-state diffusion theory (Farrell et al., 1992), while Monte Carlo simulations aim to imitate the activity of each photon to gather statistics from a large number of photons. The two methods can be utilized to identify the optical parameters of the target object in practice (Nishida et al., 2020). This is achieved by aligning the calculated image (derived from optical parameters) with the observed scattering image. Compared to the Farrell equation, Monte Carlo simulation require more computational resources, but offer greater flexibility and accuracy. Currently, when using either the Farrell equation or Monte Carlo simulation, the assumption of spatial uniformity for optical parameters is often made (Baranyai and Zude, 2009; Lorente et al., 2015; Zude-Sasse et al., 2019), which could be questionable for biological materials.

### **1.3.5 Applications**

Adebayo et al. (2016) reviewed the applications of LBI prior to 2016, reporting that LBI was used for determining soluble solids content and firmness, monitoring drying parameters, identifying defects, evaluating mechanical properties, and assessing optical properties of fruits and vegetables. Table 1.3 provides a summary of the applications of LBI in agriculture

**Table 1.3 Applications of LBI in agriculture since 2017.**

Wavelengths (nm)	Food	Applications	Prediction models	References
658, 705	Cocoa Pods	Color and maturity detection	LR, MLR, LDA	(Lockman et al., 2019)
658	Watermelon	Grading and quality measurement	PLSR, LDA	(Mohd Ali et al., 2017, 2020b)
850	Potato	Foreign materials identification	SVM, MDD, LDA	(Geng et al., 2021)
658	Sweet potato	Moisture content and color detection during drying	PLSR, PCA	(Onwude et al., 2018)
450, 520, 635	Mango	Moisture content detection during drying	MLR	(Bai et al., 2021)
650	Dairy matrix	Curdling process management	PCA, SVM-R	(Verdú et al., 2021a, 2021b)
658	Sweet potato	Grading and quality accessing	PLSR, PCA, LDA	(Sanchez et al., 2020)
520	Kiwifruit	Chilling injury detection	FDA	(Yang et al., 2021b)
635	Apple	Defect detection	CNN	(Wu et al., 2020)
658	Banana	Maturity detection	LDA	(Zulkifli et al., 2019)
658	Oil palm fresh fruit	Maturity detection	PLSR, PCA, LDA, QDA, PCA	(Mohd Ali et al. 2020a)
650	Vegetable-based creams	Quality control	PCA, SVM-R	(Verdú et al., 2019)
650	Apricot	Quality and maturity detection	ANN, PLSR	(Mozaffari et al., 2022)

Acronyms: LR, Linear Regression; MLR, Multiple Linear Regression; LDA, Linear Discriminant Analysis; QDA, Quadratic Discriminant Analysis; FDA, Flexible Discriminant Analysis; PLSR, Partial Least Squares Regression; PCA, Principal Component Analysis; SVM, Support Vector Machine; SVM-R, Support Vector Machines for Regression; MDD, Mahalanobis Distance Discrimination; ANN, Artificial Neural Network; CNN, Convolutional Neural Network.

since 2017. It is noteworthy that many scientists seem to prefer specific wavelengths, such as 658 nm. Yet, there is no definitive research suggesting that 658 nm is the ideal wavelength for a variety of food types. This preference is likely driven by the high availability of this wavelength in the laser market (Picotronic GmbH, 2023). In general, scientists have been endeavoring to extend similar applications to a wider variety of food. Nevertheless, its use in the curdling process (Verdú et al., 2021b) and in identifying foreign materials (Geng et al., 2021) demonstrates further potential application scenarios.

## **1.4 Prospects and challenges**

The challenges of LBI can be categorized into two main areas. The first challenge involves accurately linking optical theory with practical backscattering images. Food or bio-organisms are essentially complex, heterogeneous optical systems. Though understanding this complexity is daunting, it is vital for providing a theoretical framework that guides LBI development. The second challenge involves identifying additional application scenarios for LBI. While many current applications primarily focus on fruits and vegetables, the scattering phenomenon also occurs in other scenarios in agriculture. Thus, exploring new opportunities for LBI can greatly benefit the field.

## **1.5 Objectives**

The aims of this study include deepening our foundational knowledge of LBI and identifying additional application scenarios for the technology. Three detailed objectives are presented in sections 2-4, respectively. Section 2 pertains to foundational research, while sections 3 and 4 explore new application scenarios for LBI:

(i) Section 2: To understand the effect of cell size and cell content on backscattering images, sintered glass filter matrices were utilized as test models due to their distinct, stable, and consistent attributes. Section 2 focused on three primary factors that might impact backscattering images: the size of the matrix pore, the solution's characteristics (including solute type and concentration), and the wavelength.

(ii) Section 3: The oil sedimentation process is a method for purifying crude plant oil, transforming it from a cloudy, impure state to a cleaner, more refined one. This transformation indicates changes in scattering properties, suggesting that LBI could potentially be applied in this context. In Section 3, we delved into the sedimentation process of crude sesame oil and used an LBI system to monitor the changes occurring throughout the process.

(iii) Section 4: Assessing leaf wetness is crucial for predicting and mitigating fungal diseases, as it identifies conditions that encourage the proliferation. Green leaves have the capability to absorb and scatter red light, while water droplets on the leaf surface tend to strongly reflect red light. The goal of this study was to explore the potential of using LBI technology to quantify leaf wetness. For this purpose, the weight of water droplets per leaf area was used as a reference value. The accuracy and reliability of measuring this value using LBI were evaluated in this context.

## 1.6 References

- Abrougui, K., Boughattas, N. E. H., Belhaj, M., Buchaillot, M. L., Segarra, J., Dorbolo, S., Amami, R., Chehaibi, S., Tarchoun, N., & Kefauver, S. C. (2022). Assessing Phytosanitary Application Efficiency of a Boom Sprayer Machine Using RGB Sensor in Grassy Fields. *Sustainability (Switzerland)*, *14*(6), 1–15. <https://doi.org/10.3390/su14063666>
- Adebayo, S. E., Hashim, N., Abdan, K., & Hanafi, M. (2016). Application and potential of backscattering imaging techniques in agricultural and food processing – A review. *Journal of Food Engineering*, *169*, 155–164. <https://doi.org/10.1016/J.JFOODENG.2015.08.006>
- Alzubaidi, L., Zhang, J., Humaidi, A. J., Al-Dujaili, A., Duan, Y., Al-Shamma, O., Santamaría, J., Fadhel, M. A., Al-Amidie, M., & Farhan, L. (2021). Review of deep learning: concepts, CNN architectures, challenges, applications, future directions. In *Journal of Big Data* (Vol. 8, Issue 1). Springer International Publishing. <https://doi.org/10.1186/s40537-021-00444-8>
- Arefi, A., Sturm, B., Raut, S., von Gersdorff, G., & Hensel, O. (2023). NIR laser-based imaging techniques to monitor quality attributes of apple slices during the drying process: Laser-light backscattering & biospeckle imaging techniques. *Food Control*, *143*(April 2022), 109289. <https://doi.org/10.1016/j.foodcont.2022.109289>
- Bai, J. W., Zhang, L., Cai, J. R., Wang, Y. C., & Tian, X. Y. (2021). Laser light backscattering image to predict moisture content of mango slices with different ripeness during drying



- process. *Journal of Food Process Engineering*, 44(12), 1–10.  
<https://doi.org/10.1111/jfpe.13900>
- Banga, K. S., Kotwaliwale, N., Mohapatra, D., & Giri, S. K. (2018). Techniques for insect detection in stored food grains: An overview. *Food Control*, 94, 167–176.  
<https://doi.org/10.1016/j.foodcont.2018.07.008>
- Baranyai, L., & Zude, M. (2008). Analysis of laser light migration in apple tissue by Monte Carlo simulation. *Progress in Agricultural Engineering Sciences*, 4(1), 45–59.  
<https://doi.org/10.1556/Progress.4.2008.3>
- Baranyai, L., & Zude, M. (2009). Analysis of laser light propagation in kiwifruit using backscattering imaging and Monte Carlo simulation. *Computers and Electronics in Agriculture*, 69(1), 33–39. <https://doi.org/10.1016/j.compag.2009.06.011>
- Beluhova-Uzunova, R., & Dunchev, D. (2019). Precision Farming – Concepts and Perspectives. *Problems of Agricultural Economics*, 360(3), 142–155.  
<https://doi.org/10.30858/zer/112132>
- Bureau, S., Cozzolino, D., & Clark, C. J. (2019). Contributions of Fourier-transform mid infrared (FT-MIR) spectroscopy to the study of fruit and vegetables: A review. *Postharvest Biology and Technology*, 148(September 2018), 1–14.  
<https://doi.org/10.1016/j.postharvbio.2018.10.003>
- Chicco, D., Warrens, M. J., & Jurman, G. (2021). The coefficient of determination R-squared is more informative than SMAPE, MAE, MAPE, MSE and RMSE in regression analysis evaluation. *PeerJ Computer Science*, 7, 1–24. <https://doi.org/10.7717/PEERJ-CS.623>
- Childs, D. T. D., Hogg, R. A., Revin, D. G., Rehman, I. U., Cockburn, J. W., & Matcher, S. J. (2015). Sensitivity Advantage of QCL Tunable-Laser Mid-Infrared Spectroscopy over FTIR Spectroscopy. *Applied Spectroscopy Reviews*, 50(10), 822–839.  
<https://doi.org/10.1080/05704928.2015.1075208>
- da Costa Filho, P. A., Cobuccio, L., Mainali, D., Rault, M., & Cavin, C. (2020). Rapid analysis of food raw materials adulteration using laser direct infrared spectroscopy and imaging. *Food Control*, 113(October 2019), 107114.  
<https://doi.org/10.1016/j.foodcont.2020.107114>
- de Myttenaere, A., Golden, B., Le Grand, B., & Rossi, F. (2016). Mean Absolute Percentage Error for regression models. *Neurocomputing*, 192, 38–48.  
<https://doi.org/10.1016/j.neucom.2015.12.114>
- Despotovic, M., Nedic, V., Despotovic, D., & Cvetanovic, S. (2016). Evaluation of empirical models for predicting monthly mean horizontal diffuse solar radiation. *Renewable and Sustainable Energy Reviews*, 56, 246–260. <https://doi.org/10.1016/j.rser.2015.11.058>
- Di Stefano, F., Chiappini, S., Gorreja, A., Balestra, M., & Pierdicca, R. (2021). Mobile 3D scan LiDAR: a literature review. *Geomatics, Natural Hazards and Risk*, 12(1), 2387–2429.  
<https://doi.org/10.1080/19475705.2021.1964617>

- DIN EN 60825-1. (2022). *Safety of laser products - Part 1: Equipment classification and requirements (IEC 60825-1:2014)*.
- Divyanth, L. G., Chelladurai, V., Loganathan, M., Jayas, D. S., & Soni, P. (2022). Identification of Green Gram (*Vigna radiata*) Grains Infested by *Callosobruchus maculatus* Through X-ray Imaging and GAN-Based Image Augmentation. *Journal of Biosystems Engineering*. <https://doi.org/10.1007/s42853-022-00147-9>
- Einstein, A. (1917). Zur Quantentheorie der Strahlung. *Physik Zeitschrift XVIII*, 121–128.
- El-Mesery, H.S., Mao, H., & Abomohra, A. (2019). Applications of Non-destructive Technologies for Agricultural and Food Products Quality Inspection. *Sensors*, 19(4), 846. <https://doi.org/10.3390/s19040846>
- Farina, L., Scapaticci, R., Tobon Vasquez, J. A., Rivero, J., Litman, A., Crocco, L., & Vipiana, F. (2019). Microwave imaging technology for in-line food contamination monitoring. *2019 IEEE International Symposium on Antennas and Propagation and USNC-URSI Radio Science Meeting, APSURSI 2019 - Proceedings*, 817–818. <https://doi.org/10.1109/APUSNCURSINRSM.2019.8889369>
- Farrell, T. J., Patterson, M. S., & Wilson, B. (1992). A diffusion theory model of spatially resolved, steady-state diffuse reflectance for the noninvasive determination of tissue optical properties in vivo. *Medical Physics*, 19(4), 879–888. <https://doi.org/10.1118/1.596777>
- Friebel, M., Kroh, L. W., Lurie, S., Meinke, M., Rohn, S., & Torricelli, A. (2008a). Optical sensing. In M. Zude (Ed.), *Optical monitoring of fresh and processed agricultural crops* (pp. 44–78). CRC Press.
- Friebel, M., Kroh, L. W., Lurie, S., Meinke, M., Rohn, S., & Torricelli, A. (2008b). Quality parameters of fresh fruit and vegetable at harvest and self life. In M. Zude (Ed.), *Optical monitoring of fresh and processed agricultural crops* (pp. 2–17). CRC Press.
- Garland, N. T., McLamore, E. S., Cavallaro, N. D., Mendivelso-Perez, D., Smith, E. A., Jing, D., & Claussen, J. C. (2018). Flexible Laser-Induced Graphene for Nitrogen Sensing in Soil. *ACS Applied Materials and Interfaces*, 10(45), 39124–39133. <https://doi.org/10.1021/acsami.8b10991>
- Geng, J., Min, H., & Rao, X. (2021). Separation of clods and stones from harvested potatoes using laser backscattering imaging technique. *Journal of Food Measurement and Characterization*, 15(4), 3262–3273. <https://doi.org/10.1007/s11694-021-00896-9>
- Geng, J., Xiao, L., He, X., & Rao, X. (2019). Discrimination of clods and stones from potatoes using laser backscattering imaging technique. *Computers and Electronics in Agriculture*, 160(March), 108–116. <https://doi.org/10.1016/j.compag.2019.03.014>
- Ghavami, N., Sotiriou, I., Cano-Garcia, H., & Kosmas, P. (2021). An experimental microwave imaging prototype for food quality assessment. *2021 34th General Assembly and Scientific Symposium of the International Union of Radio Science, URSI GASS 2021*,

- September, 2021–2023. <https://doi.org/10.23919/URSIGASS51995.2021.9560644>
- Granzow, N. (2019). *Supercontinuum white light lasers: a review on technology and applications*. 1114408(September 2019), 49. <https://doi.org/10.1117/12.2533094>
- Hashim, N., Pflanz, M., Regen, C., Janius, R. B., Abdul Rahman, R., Osman, A., Shitan, M., & Zude, M. (2013). An approach for monitoring the chilling injury appearance in bananas by means of backscattering imaging. *Journal of Food Engineering*, 116(1), 28–36. <https://doi.org/10.1016/j.jfoodeng.2012.11.018>
- Hashimi, S., Ganji, H., Kondo, M., Ito, R., & Kajisa, T. (2017). Laser land leveling for crop yield and water efficiency in eastern Afghanistan. *International Journal of GEOMATE*, 13(36), 116–121. <https://doi.org/10.21660/2017.36.2869>
- Hussain, A., Pu, H., & Sun, D. W. (2018). Innovative nondestructive imaging techniques for ripening and maturity of fruits – A review of recent applications. *Trends in Food Science and Technology*, 72, 144–152. <https://doi.org/10.1016/j.tifs.2017.12.010>
- Iida, D., Kokawa, M., & Kitamura, Y. (2023). Estimation of Apple Mealiness by Means of Laser Scattering Measurement. *Food and Bioprocess Technology*, 0123456789. <https://doi.org/10.1007/s11947-023-03068-3>
- Iqbal, J., Xu, R., Sun, S., & Li, C. (2020). Simulation of an autonomous mobile robot for LiDAR-based in-field phenotyping and navigation. *Robotics*, 9(2), 1–19. <https://doi.org/10.3390/robotics9020046>
- Ishimwe, R., Abutaleb, K., & Ahmed, F. (2014). Applications of Thermal Imaging in Agriculture—A Review. *Advances in Remote Sensing*, 03(03), 128–140. <https://doi.org/10.4236/ars.2014.33011>
- Jat, M. L., Singh, Y., Gill, G., Sidhu, H., Aryal, J. P., Stirling, C., & Gerard, B. (2014). Laser assisted precision land leveling: Impacts in irrigated intensive production systems of South Asia. *Advances in Soil Science*, 22, 323–352.
- Jia, W., Karapetrova, A., Zhang, M., Xu, L., Li, K., Huang, M., Wang, J., & Huang, Y. (2022). Automated identification and quantification of invisible microplastics in agricultural soils. *Science of The Total Environment*, 844, 156853. <https://doi.org/https://doi.org/10.1016/j.scitotenv.2022.156853>
- Jin, S., Sun, X., Wu, F., Su, Y., Li, Y., Song, S., Xu, K., Ma, Q., Baret, F., Jiang, D., Ding, Y., & Guo, Q. (2021). Lidar sheds new light on plant phenomics for plant breeding and management: Recent advances and future prospects. *ISPRS Journal of Photogrammetry and Remote Sensing*, 171(20), 202–223. <https://doi.org/10.1016/j.isprsjprs.2020.11.006>
- King, A. (2017). Technology: The Future of Agriculture. *Nature*, 544(7651), S21–S23. <https://doi.org/10.1038/544S21a>
- Klimek-Kopyra, A., Dobrowolski, J. W., Czech, T., Neugschwandtner, R. W., Gambuś, F., &

- Kot, D. (2021). The use of laser biotechnology in agri-environment as a significant agronomical advance increasing crop yield and quality. *Advances in Agronomy*, *170*, 1–33. <https://doi.org/10.1016/bs.agron.2021.06.001>
- Korostynska, O., Mason, A., & From, P. J. (2018). *Electromagnetic Sensing for Non-Destructive Real-Time Fruit Ripeness Detection: Case-Study for Automated Strawberry Picking*. 980. <https://doi.org/10.3390/proceedings2130980>
- Lan, L., Le, X., Dong, H., Xie, J., Ying, Y., & Ping, J. (2020). One-step and large-scale fabrication of flexible and wearable humidity sensor based on laser-induced graphene for real-time tracking of plant transpiration at bio-interface. *Biosensors and Bioelectronics*, *165*(June), 112360. <https://doi.org/10.1016/j.bios.2020.112360>
- Li, B., Lecourt, J., & Bishop, G. (2018). Advances in non-destructive early assessment of fruit ripeness towards defining optimal time of harvest and yield prediction—a review. *Plants*, *7*(1), 1–20. <https://doi.org/10.3390/plants7010003>
- Li, Y., Chen, S., Chen, H., Guo, P., Li, T., & Xu, Q. (2020). Effect of thermal oxidation on detection of adulteration at low concentrations in extra virgin olive oil: Study based on laser-induced fluorescence spectroscopy combined with KPCA–LDA. *Food Chemistry*, *309*(October 2019). <https://doi.org/10.1016/j.foodchem.2019.125669>
- Lian, R. (2018). On Huygens' principle, extinction theorem, and equivalence principle (Metal-Material Combined System in Inhomogeneous Anisotropic Environment). *ArXiv*. <https://doi.org/10.48550/arXiv.1802.02096>
- Lockman, N. A., Hashim, N., & Onwude, D. I. (2019). Laser-Based imaging for Cocoa Pods Maturity Detection. *Food and Bioprocess Technology*, *12*(11), 1928–1937. <https://doi.org/10.1007/s11947-019-02350-7>
- Lorente, D., Zude, M., Idler, C., Gómez-Sanchis, J., & Blasco, J. (2015). Laser-light backscattering imaging for early decay detection in citrus fruit using both a statistical and a physical model. *Journal of Food Engineering*, *154*, 76–85. <https://doi.org/10.1016/j.jfoodeng.2015.01.004>
- MathWorks. (2023). Partial Least Squares Regression and Principal Components Regression. <https://www.mathworks.com/help/stats/partial-least-squares-regression-and-principal-components-regression.html>. Accessed May 2, 2023
- McGlone, V. A., Abe, H., & Kawano, S. (1997). Kiwifruit firmness by near infrared light scattering. *Journal of Near Infrared Spectroscopy*, *5*(2), 83–89. <https://doi.org/10.1255/jnirs.102>
- Messina, G., & Modica, G. (2020). Applications of UAV thermal imagery in precision agriculture: State of the art and future research outlook. *Remote Sensing*, *12*(9). <https://doi.org/10.3390/RS12091491>
- Mohd Ali, M., Hashim, N., & Abdul Hamid, A. S. (2020a). Combination of laser-light backscattering imaging and computer vision for rapid determination of oil palm fresh

- fruit bunches maturity. *Computers and Electronics in Agriculture*, 169, Article 105235. <https://doi.org/10.1016/j.compag.2020.105235>
- Mohd Ali, M., Hashim, N., Bejo, S. K., & Shamsudin, R. (2017). Quality evaluation of watermelon using laser-induced backscattering imaging during storage. *Postharvest Biology and Technology*, 123, 51–59. <https://doi.org/10.1016/j.postharvbio.2016.08.010>
- Mohd Ali, M., Hashim, N., Bejo, S. K., & Shamsudin, R. (2020b). Comparison of laser backscattering imaging and computer vision system for grading of seedless watermelons. *Journal of Food Measurement and Characterization*, 14(1), 69–77. <https://doi.org/10.1007/s11694-019-00268-4>
- Mollazade, K., Omid, M., Tab, F. A., & Mohtasebi, S. S. (2012). Principles and Applications of Light Backscattering Imaging in Quality Evaluation of Agro-food Products: a Review. *Food and Bioprocess Technology*, 5, 1465–1485. <https://doi.org/10.1007/s11947-012-0821-x>
- Mozaffari, M., Sadeghi, S., & Asefi, N. (2022). Prediction of the quality properties and maturity of apricot by laser light backscattering imaging. *Postharvest Biology and Technology*, 186, 111842. <https://doi.org/https://doi.org/10.1016/j.postharvbio.2022.111842>
- Nicolaï, B. M., Beullens, K., Bobelyn, E., Peirs, A., Saeys, W., Theron, K. I., & Lammertyn, J. (2007). Nondestructive measurement of fruit and vegetable quality by means of NIR spectroscopy: A review. *Postharvest Biology and Technology*, 46(2), 99–118. <https://doi.org/10.1016/j.postharvbio.2007.06.024>
- Nishida, K., Kato, Y., Kudo, N., & Shimizu, K. (2020). Nonlinear inversion technique for absorption tomography of turbid media using spatially resolved backscattered light. *Optics and Lasers in Engineering*, 126(October 2019). <https://doi.org/10.1016/j.optlaseng.2019.105891>
- Núñez, E., Steyerberg, E. W., & Núñez, J. (2011). Regression Modeling Strategies. *Revista Española de Cardiología (English Edition)*, 64(6), 501–507. <https://doi.org/10.1016/j.rec.2011.01.017>
- Onwude, D. I., Hashim, N., Abdan, K., Janius, R., & Chen, G. (2018). Combination of computer vision and backscattering imaging for predicting the moisture content and colour changes of sweet potato (*Ipomoea batatas* L.) during drying. *Computers and Electronics in Agriculture*, 150(February), 178–187. <https://doi.org/10.1016/j.compag.2018.04.015>
- Paleg, L. G., & Aspinall, D. (1970). Field Control of Plant Growth and Development through the Laser Activation of Phytochrome. *Nature*, 228(5275), 970–973. <https://doi.org/10.1038/228970a0>
- Pandiselvam, R., Mayookha, V. P., Kothakota, A., Ramesh, S. V., Thirumdas, R., & Juvvi, P. (2020). Biospeckle laser technique – A novel non-destructive approach for food quality

- and safety detection. *Trends in Food Science and Technology*, 97(June 2019), 1–13. <https://doi.org/10.1016/j.tifs.2019.12.028>
- Picotronic GmbH. (2023). *Laser searching from Picotronic GmbH*. <https://www.picotronic.de/picopage/en/product/search>. Accessed March 31, 2022
- Qin, J., & Lu, R. (2009). Monte Carlo simulation for quantification of light transport features in apples. *Computers and Electronics in Agriculture*, 68(1), 44–51. <https://doi.org/10.1016/j.compag.2009.04.002>
- Qing, Z., Ji, B., & Zude, M. (2007a). Wavelength selection for predicting physicochemical properties of apple fruit based on near-infrared spectroscopy. *Journal of Food Quality*, 30(4), 511–526. <https://doi.org/10.1111/j.1745-4557.2007.00139.x>
- Qing, Z., Ji, B., & Zude, M. (2007b). Predicting soluble solid content and firmness in apple fruit by means of laser light backscattering image analysis. *Journal of Food Engineering*, 82(1), 58–67. <https://doi.org/10.1016/j.jfoodeng.2007.01.016>
- Qing, Z., Ji, B., & Zude, M. (2008). Non-destructive analyses of apple quality parameters by means of laser-induced light backscattering imaging. *Postharvest Biology and Technology*, 48(2), 215–222. <https://doi.org/10.1016/j.postharvbio.2007.10.004>
- Rahmanian, A., Mireei, S. A., Sadri, S., Gholami, M., & Nazeri, M. (2020). Application of biospeckle laser imaging for early detection of chilling and freezing disorders in orange. *Postharvest Biology and Technology*, 162(January), 111118. <https://doi.org/10.1016/j.postharvbio.2020.111118>
- Saito, Y., Ichihara, K., Morishita, K., Uchiyama, K., Kobayashi, F., & Tomida, T. (2018). Remote detection of the fluorescence spectrum of natural pollens floating in the atmosphere using a laser-induced-fluorescence spectrum (LIFS) lidar. *Remote Sensing*, 10(10). <https://doi.org/10.3390/rs10101533>
- Sanchez, P. D. C., Hashim, N., Shamsudin, R., & Mohd Nor, M. Z. (2020). Laser-light backscattering imaging approach in monitoring and classifying the quality changes of sweet potatoes under different storage conditions. *Postharvest Biology and Technology*, 164, Article 111163. <https://doi.org/10.1016/j.postharvbio.2020.111163>
- Sijs, R., Kooij, S., Holterman, H. J., Van De Zande, J., & Bonn, D. (2021). Drop size measurement techniques for sprays: Comparison of image analysis, phase Doppler particle analysis, and laser diffraction. *AIP Advances*, 11(1). <https://doi.org/10.1063/5.0018667>
- Smalley, P. J. (2011). Laser safety: Risks, hazards, and control measures. *Laser Therapy*, 20(2), 95–106. <https://doi.org/10.5978/islsm.20.95>
- Sood, S., Mahajan, S., Doegar, A., & Das, A. (2016). Internal crack detection in kidney bean seeds using X-ray imaging technique. *2016 International Conference on Advances in Computing, Communications and Informatics, ICACCI 2016*, 2258–2261.

<https://doi.org/10.1109/ICACCI.2016.7732388>

- Steinfeld, J. I., & Zare, R. N. (1975). Tunable lasers and their application in analytical chemistry. *C R C Critical Reviews in Analytical Chemistry*, 5(3), 225–241. <https://doi.org/10.1080/10408347508542685>
- Teng, X., Zhang, M., & Mujumdar, A. S. (2021). Potential application of laser technology in food processing. *Trends in Food Science and Technology*, 118(PA), 711–722. <https://doi.org/10.1016/j.tifs.2021.10.031>
- Tinti, A., Tugnoli, V., Bonora, S., & Francioso, O. (2015). Recent applications of vibrational mid-infrared (IR) spectroscopy for studying soil components: A review. *Journal of Central European Agriculture*, 16(1), 1–22. <https://doi.org/10.5513/JCEA01/16.1.1535>
- Tsuchikawa, S., Ma, T., & Inagaki, T. (2022). Application of near-infrared spectroscopy to agriculture and forestry. *Analytical Sciences*, 38(4), 635–642. <https://doi.org/10.1007/s44211-022-00106-6>
- Udomkun, P., Nagle, M., Mahayothee, B., & Müller, J. (2014). Laser-based imaging system for non-invasive monitoring of quality changes of papaya during drying. *Food Control*, 42, 225–233. <https://doi.org/10.1016/j.foodcont.2014.02.010>
- Vadivambal, R., & Jayas, D. S. (2011). Applications of Thermal Imaging in Agriculture and Food Industry-A Review. *Food and Bioprocess Technology*, 4(2), 186–199. <https://doi.org/10.1007/s11947-010-0333-5>
- Velesaca, H. O., Suárez, P. L., Mira, R., & Sappa, A. D. (2021). Computer vision based food grain classification: A comprehensive survey. *Computers and Electronics in Agriculture*, 187(July). <https://doi.org/10.1016/j.compag.2021.106287>
- Verdú, S., Perez, A. J., Barat, J. M., & Grau, R. (2021a). Laser-backscattering imaging for characterising the dairy matrix in different phases during curd processing. *Food Control*, 128, Article 108193. <https://doi.org/10.1016/j.foodcont.2021.108193>
- Verdú, S., Pérez, A. J., Barat, J. M., & Grau, R. (2019). Laser backscattering imaging as a control technique for fluid foods: Application to vegetable-based creams processing. *Journal of Food Engineering*, 241, 58–66. <https://doi.org/10.1016/j.jfoodeng.2018.08.003>
- Verdú, S., Pérez, A. J., Barat, J. M., & Grau, R. (2021b). Non-destructive control in cheese processing: Modelling texture evolution in the milk curdling phase by laser backscattering imaging. *Food Control*, 121, Article 107638. <https://doi.org/10.1016/j.foodcont.2020.107638>
- Weng, S., Hu, X., Wang, J., Tang, L., Li, P., Zheng, S., Zheng, L., Huang, L., & Xin, Z. (2021). Advanced Application of Raman Spectroscopy and Surface-Enhanced Raman Spectroscopy in Plant Disease Diagnostics: A Review. *Journal of Agricultural and Food Chemistry*, 69(10), 2950–2964. <https://doi.org/10.1021/acs.jafc.0c07205>

- Weng, S., Zhu, W., Zhang, X., Yuan, H., Zheng, L., Zhao, J., Huang, L., & Han, P. (2019). Recent advances in Raman technology with applications in agriculture, food and biosystems: A review. *Artificial Intelligence in Agriculture*, 3, 1–10. <https://doi.org/10.1016/j.aiia.2019.11.001>
- Wu, A., Zhu, J., & Ren, T. (2020). Detection of apple defect using laser-induced light backscattering imaging and convolutional neural network. *Computers and Electrical Engineering*, 81, 106454. <https://doi.org/10.1016/j.compeleceng.2019.106454>
- Wu, Q., Xu, J., & Xu, H. (2019). Discrimination of aflatoxin B 1 contaminated pistachio kernels using laser induced fluorescence spectroscopy. *Biosystems Engineering*, 179, 22–34. <https://doi.org/10.1016/j.biosystemseng.2018.12.009>
- Yang, J., Du, L., Gong, W., Shi, S., Sun, J., & Chen, B. (2018). Potential of vegetation indices combined with laser-induced fluorescence parameters for monitoring leaf nitrogen content in paddy rice. *PLoS ONE*, 13(1), 1–15. <https://doi.org/10.1371/journal.pone.0191068>
- Yang, Y., Wang, L., Wendroth, O., Liu, B., Cheng, C., Huang, T., & Shi, Y. (2019). Is the Laser Diffraction Method Reliable for Soil Particle Size Distribution Analysis? *Soil Science Society of America Journal*, 83(2), 276–287. <https://doi.org/10.2136/sssaj2018.07.0252>
- Yang, Y., Creedon, N., O’Riordan, A., & Lovera, P. (2021a). Surface Enhanced Raman Spectroscopy: Applications in Agriculture and Food Safety. *Photonics*, 8(12). <https://doi.org/10.3390/photonics8120568>
- Yang, Z., Li, M., East, A. R., & Zude-Sasse, M. (2021b). Application of absorption and scattering properties obtained through image pre-classification method using a laser backscattering imaging system to detect kiwifruit chilling injury. *Foods*, 10(7). <https://doi.org/10.3390/foods10071446>
- Yu, K., Ren, J., & Zhao, Y. (2020). Principles, developments and applications of laser-induced breakdown spectroscopy in agriculture: A review. *Artificial Intelligence in Agriculture*, 4, 127–139. <https://doi.org/10.1016/j.aiia.2020.07.001>
- Zinth, W., Laubereau, A., & Kaiser, W. (2011). The long journey to the laser and its rapid development after 1960. *European Physical Journal H*, 36(2), 153–181. <https://doi.org/10.1140/epjh/e2011-20016-0>
- Zude-Sasse, M., Hashim, N., Hass, R., Polley, N., & Regen, C. (2019). Validation study for measuring absorption and reduced scattering coefficients by means of laser-induced backscattering imaging. *Postharvest Biology and Technology*, 153(March), 161–168. <https://doi.org/10.1016/j.postharvbio.2019.04.002>
- Zulkifli, N., Hashim, N., Abdan, K., & Hanafi, M. (2019). Application of laser-induced backscattering imaging for predicting and classifying ripening stages of “Berangan” bananas. *Computers and Electronics in Agriculture*, 160(January), 100–107. <https://doi.org/10.1016/j.compag.2019.02.0>



# 2

## **Investigating the influence of pore size, pore fluid and wavelength on backscattering images with sintered glass filter matrices as experimental models**

Zhangkai Wu <sup>a</sup>, Klaus Spohrer <sup>a</sup>, Marcus Nagle <sup>b</sup>, Joachim Müller <sup>a</sup>

<sup>a</sup> University of Hohenheim, Institute of Agricultural Engineering, Tropics and Subtropics Group, Stuttgart, 70599, Germany

<sup>b</sup> Central State University, Agricultural Research and Development Program, Wilberforce Ohio 45384, USA

*Published in Postharvest Biology and Technology, 200, 112329, March 2023*  
<https://doi.org/10.1016/j.postharvbio.2023.112329>

## 2.1 Abstract

Laser backscattering imaging (LBI) is an economic, energy-saving method, which can be applied to characterize bio-organisms in postharvest processes. When applying LBI to horticultural crops, scientists seldom report the cell size of their samples, and often consider the scattering coefficient as constant. The objective of this research was to investigate the influence of pore size, the pore filling for different solutes and concentrations, and wavelength under controlled conditions. Porous glass discs with five different pore diameters from 1 to 160  $\mu\text{m}$  were used as reproducible experimental models for the experiment. NaCl aqueous solutions (0, 1, 2, 3 and 4 mol/L) and  $\text{NaH}_2\text{PO}_4$  aqueous solutions (0, 0.8, 1.6, 2.4 and 3.2 mol/L) were applied as pore fills. The LBI system used laser modules at three wavelengths (405, 635, 780 nm). The results revealed that three of the four investigated experimental factors influence LBI, specifically: i) the pore diameter, ii) the solutes and iii) their concentrations. In contrast, the three wavelengths applied did not show clear differences in the LBI patterns. Thus, when applying LBI on fruit for example, the cell size at different depths from the fruit surface needs to be carefully considered.

## 2.2 Introduction

Laser backscattering imaging (LBI) is an emerging non-destructive imaging technology, capable of providing fast and characteristic information about the properties of translucent materials (Hussain et al., 2018; Verdú et al., 2019). The principle of LBI is as follows: focused light that penetrates a translucent sample is absorbed and scattered inside the sample, which finally leads to a halo-like light spot on the sample's surface. The size and light intensity distribution of the surface light spot are influenced by certain sample properties. LBI is currently investigated as an economic, energy-efficient method, which can be applied to biological materials (Romano et al., 2011; Sanchez et al., 2020b).

A review about the potential of LBI was provided by Adebayo et al. (2016). Hashim et al. (2013) reported that LBI at wavelengths of 660 and 785 nm were able to detect chilling injuries in bananas. The bruising of apples cv. "Golden Delicious" was detected with a LBI system at 670

nm (Baranyai and Zude, 2008). LBI could distinguish healthy from decaying parts of oranges cv. "Valencia Late" at five different wavelengths (Lorente et al., 2015). LBI was also applied to detect the maturity of tomatoes (Tu et al., 2000), to grade seedless watermelons during storage (Mohd Ali et al., 2020b), to determinate the maturity of oil palm fruit bunches (Mohd Ali et al., 2020a) and to monitor quality changes in sweet potatoes (Sanchez et al., 2020a). Romano et al. (2012) used wavelengths of 532 and 635 nm to derive the moisture content of yellow bell peppers during the drying process. In addition, a 635 nm laser was used to predict the moisture content and soluble solids content (SSC) of apples during drying (Romano et al., 2011), similar research about mango slices was also performed (Bai et al., 2021). Onwude et al. (2018) used a neural network to combine digital images and LBI to predict the drying process. Moreover, the potential to use LBI to characterize the curdling process of milk has been demonstrated (Verdú et al., 2021a, 2021b). Although cell size is generally thought to influence the scattering phenomenon in fruit, few researchers have reported the cell size of their samples, which may be in part because they do not know the extent to which cell size affects the outcome.

To improve a LBI system, image processing algorithms were tested to deal with the curvature of fruit surfaces (Qing et al., 2007). A bimodal threshold was used to segment the grey value histogram output from the image into the area of interest and the background (Qing et al., 2008). The Gaussian–Lorentzian cross product distribution function was applied to describe LBI results and linear discriminant analysis was used to find an optimal wavelength combination for its prediction (Lorente et al., 2013). LBI was analyzed by conducting partial least squares regression and principal component analysis (Verdú et al., 2022).

Some efforts have already been made to explain the underlying physical principles of LBI. Farrell's diffusion theory was used to calculate the absorption coefficients ( $\mu_a$ ) and reduced scattering coefficients ( $\mu'_s$ ) (Lorente et al., 2015). Baranyai and Zude (2009) applied Monte Carlo simulation to LBI and investigated the anisotropy factor ( $g$ ) of kiwifruit. Martelli et al. (2016) calculated the penetration depth of light in arbitrary media. These calculations assumed that  $\mu_a$  or  $\mu'_s$  was generally spatially uniform inside turbid media, which is questionable for biological materials. To build better models for simulating light behaviour in biological systems, understanding the influence of cell size and the interactive impact of cell

size and cell contents is essential.

Up to now, the focus of LBI research in postharvest processes has mainly focused on empirical quality detection and control. Although many authors reported on the influencing factors like pore sizes and solution properties (dissolved substances and their concentrations) (Onwude et al., 2018; Romano et al., 2012, Mollazade et al. 2012), as well the particular suitability of certain laser wavelengths (Adebayo et al., 2016; Hashim et al., 2013), how these influencing factors affect the scattering phenomenon still needs warrants investigation. Previous research was typically performed on biological material with natural inhomogeneity and temporal changes in properties. Therefore, the objective of this research is using a matrix material with defined, stable and reproducible properties to investigate the influence of the following factors on LBI: i) the matrix pore size, ii) the properties of the solution, such as solute type and concentration, within the pores and iii) wavelength.

## **2.3 Materials and Methods**

### **2.3.1 Sintered glass matrix**

Standardized sintered glass filter discs (VitraPOR, ROBU Glasfilter-Geräte GmbH, Hattert, Germany) were used as a reproducible experimental model, in which different, standardized pore size distributions could be selected and the aqueous solution for the pore filling could be set in terms of solute and concentration. As shown in Table 2.1 and Figure 2.1, porous discs with five different pore diameters from 1 to 160  $\mu\text{m}$  (ISO 4793:1980) were used in the experiments, representing the range of cell sizes of plant tissues. The porous discs had a diameter of 40 mm and a thickness of 3.5 mm. The refractive index (sodium D line) was 1.474 and the visible light transmission was 91 %. Three porous discs per pore size category were used for replication, i.e. 15 porous discs were used in total.

**Table 2.1 Pore properties of the sintered glass discs (ROBU GmbH, 2022a, 2022b).**

Code	P1.6	P16	P40	P100	P160
Pore diameter range, $\mu\text{m}$	1 – 1.6	10 - 16	16 - 40	40 - 100	100 - 160
Pore diameter median, $\mu\text{m}$	1.3	11	23	70	141
Internal surface, $\text{m}^2/\text{cm}^3$	2.03	0.65	0.46	0.19	0.13

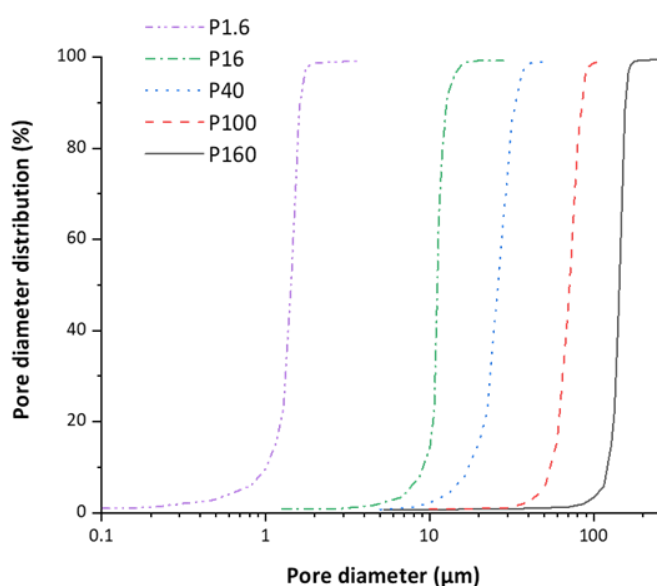


**Figure 2.1** Approximate pore size distribution of the sintered glass discs (ROBU GmbH, 2022a).

### 2.3.2 Chemical solutions

Two different aqueous sodium-solutions, namely NaCl in concentrations of 1, 2, 3 and 4 mol/L, and  $\text{NaH}_2\text{PO}_4$  in concentrations of 0.8, 1.6, 2.4 and 3.2 mol/L were tested as pore fluids to provide a range of different refractive indexes because refraction is considered as a basic principle for the laser backscattering under investigation (McGlone et al., 1997). Different intervals were chosen due to the solubility difference of the two solutes. The respective solutions were prepared by dissolving 58.44 g, 116.88 g, 175.32 g and 233.76 g of NaCl (Merck, New Jersey, USA), as well as 124.81 g, 249.62 g, 374.42 g and 499.23 g of  $\text{NaH}_2\text{PO}_4 \cdot 2\text{H}_2\text{O}$  (Applichem, Darmstadt, Germany) in 1 L of distilled water. There is a linear relationship between solution concentration and refractive index (Glover and Goulden, 1963). The

corresponding refractive indexes (sodium D line, 20°C) are shown in Figure 2.2 (Haynes, 2014). Since water is a major component of agricultural products, and when modeling light propagation in food, an average refractive index of 1.4 is often assumed (Mollazade et al., 2012). As mentioned in section 2.3.1, the material of the porous disc has a refractive index of 1.474, so we used aqueous solutions with a refractive index less than 1.4 in this study.

The porous discs were saturated by soaking them in the respective solution for 17 h. Shortly before the measurements, the discs were taken out and the surplus solution on their surface was removed. After the measurements, the porous discs were soaked and rinsed in distilled water to wash out the tested solution, dried in an oven and then soaked with the next solution until saturation.

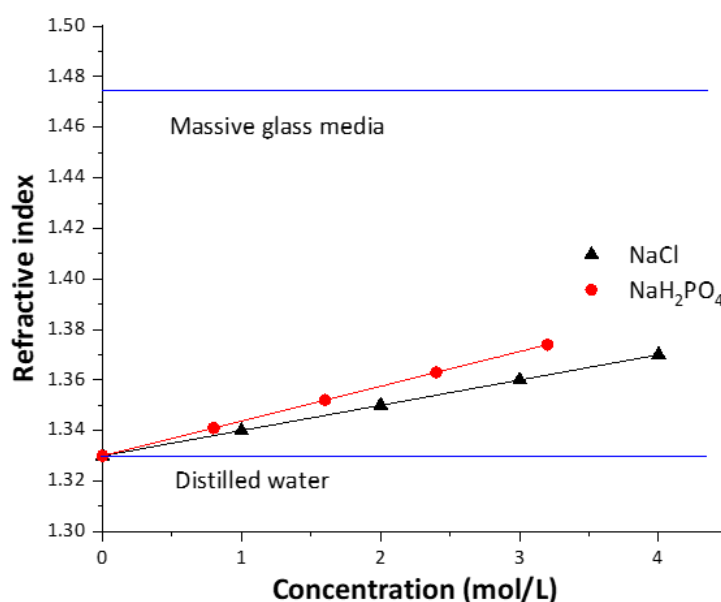


**Figure 2.2** Refractive indexes of the matrix of the porous discs (massive glass) used, and of the NaCl and NaH<sub>2</sub>PO<sub>4</sub> aqueous solutions with different concentrations (sodium D line, 20°C) (Haynes, 2014).

### 2.3.3 LBI system

The LBI system consisted of a microscope camera (PX5-CM, PAX cam, Villa Park, IL, USA) with a zoom lens, three laser modules (Picotronic, Koblenz, Germany) for blue, red and infrared light with wavelengths of 405 nm (DD405-1-3,  $\Phi$ 2 mm), 635 nm (LFD635-1-3,  $\Phi$ 3 mm) and 780 nm (LFD780-5-3,  $\Phi$ 3.5 mm) and a computer with the image acquisition software Pax-It

(PAX cam, Villa Park, IL, USA). To minimize the direct laser light reflection and optimize the laser light penetration into the porous discs, the incident angles of the lasers were set at  $13^\circ$ . This angle could avoid direct reflection but keep the incident laser light beam close to vertical (Mollazade et al., 2012; Udomkun et al., 2014). The LBI system was installed in a climate-controlled laboratory at  $23^\circ\text{C}$  and operated within a darkened housing to avoid the influence of ambient light. The distance between the upper surface of the porous disc and the camera lens was 248 mm. The exposure time of the camera for the laser light with the wavelengths of 405, 635 and 780 nm was set to 321, 70 and 178 ms, respectively. The images captured with this system setup contained  $2592 \times 1944$  pixels (5MP) with a 79.6 pixel/mm resolution. For each setting, nine images were taken at three positions of the disc. In total, 1350 images were taken.

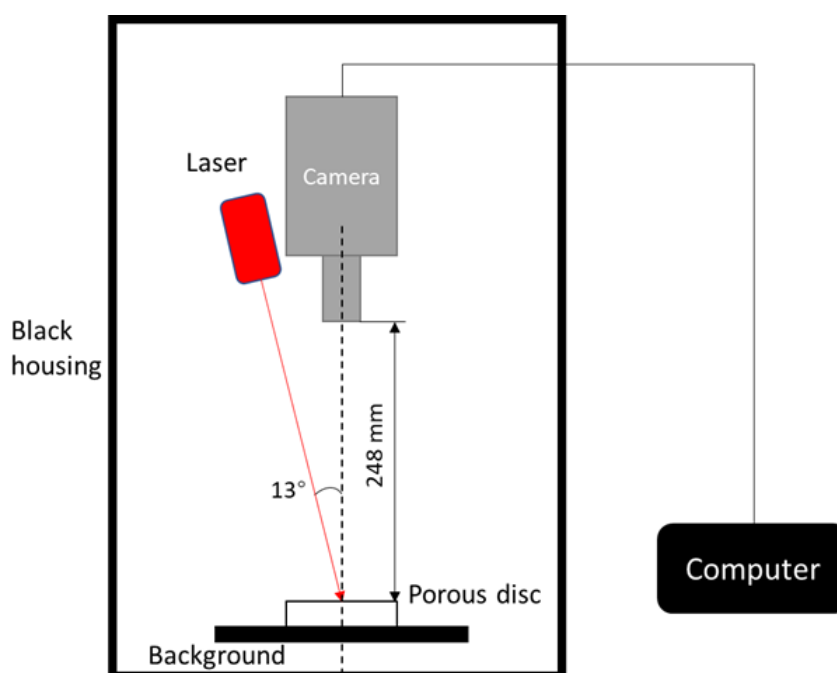


**Figure 2.3** Setup of laser backscattering imaging system.

### 2.3.4 Image analysis

To characterize the different backscattering patterns caused by the various settings of pore size, solution and laser wavelength, the obtained images of the light spot on the surface of the porous discs were analyzed. Figure 2.4a shows exemplarily RGB images on P100 porous discs with distilled water. Refraction, reflection and scattering create a halo-like light pattern

on the surface of the porous disc. Using 635 nm as an example, a bright white central light spot is surrounded by a narrow concentric yellow ring, followed by a wider red ring. The border of the backscattering area is not clearly delineated, but the intensity decreases continuously. In Figure 2.4c the RGB light intensities on a scale of 0-255 are plotted against the radial distance from the center of the halo. Unexpectedly, for the 635 nm laser and the 780 nm laser, G- and B-values were measured, although only monochrome red and infrared light was applied. This is caused by overexposure of the camera due to the high light intensity in the center of the halo. The center appears white by superimposing red, green and blue light and changes to yellow by superimposing red and green light and finally appears red. Similar phenomenon existed for 405 nm laser. Consequently, the grey value  $I_{Grey}$  shows a sigmoidal profile, in which  $I$  is calculated as:

$$I_{Grey} = \frac{I_R + I_G + I_B}{3} \quad (2-1)$$

where  $I_R$ ,  $I_G$ ,  $I_B$  are the intensities of the red, green and blue lights on a scale of 0-255. Thus, the values of  $I_{Grey}$  also range between 0 and 255. Pre-tests revealed a radially symmetric pattern of the light intensity on the porous discs. Therefore, this radial distribution of light intensity was simplified by an averaged radial 1D-profile (Figure 2.4c,d), calculated with the average of four orthogonal profiles: 0-L1, 0-L2, 0-L3 and 0-L4 (Lorente et al., 2015). All original 1D-profiles were smoothed with a moving average function with the period parameter set to 31. The backscattering area  $A$  was measured as sum of all pixels with a red channel intensity between 105 and 255 (635 and 780 nm laser) or a blue channel intensity between 155 and 255 (405 nm laser) by using Photoshop's Magic Wand tool (CS4, Adobe Inc., San Jose, USA). The edge of the area was smoothed by the tool. Symbols  $A_{405}$ ,  $A_{635}$ ,  $A_{780}$  were used to represent the backscattering area of 405 nm, 635 nm and 780 nm laser, respectively.



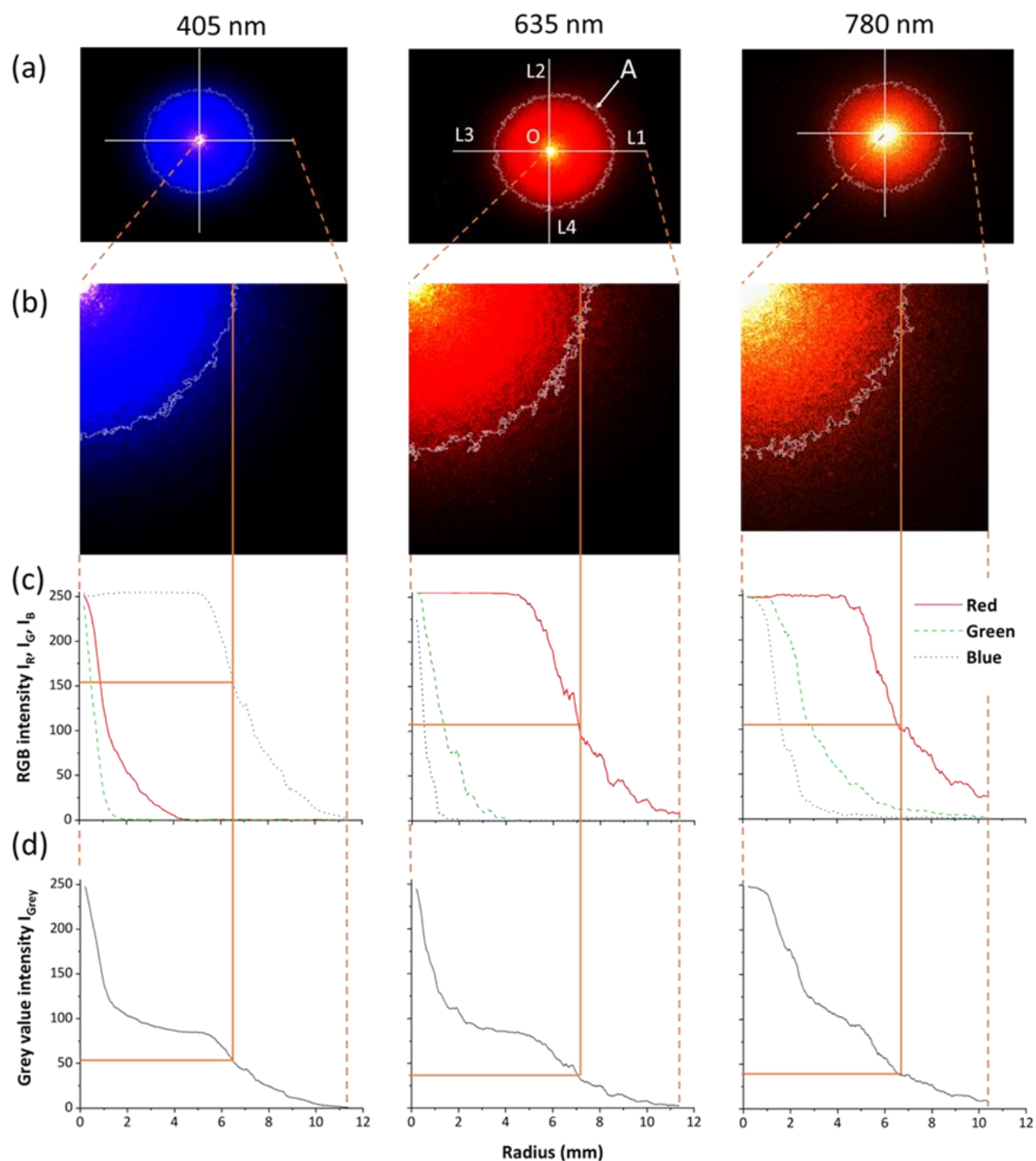


**Figure 2.4** Laser light backscattering imaging (LBI) of a P100 disc saturated with distilled water; (a) original images with identification of area A and transects O-L1, O-L2, O-L3, and O-L4. The average intensity of these four transects was used to plot the histograms; (b) enlargements according to the length of the transects; (c) corresponding intensity profiles of the red, green and blue channel (0-255); and (d) grey value intensity profiles (0-255). The dashed ochre lines mark the ranges of the histograms, the full ochre lines mark the radius of the illuminated area and the corresponding intensity values.

### 2.3.5 Statistical analysis

Linear regression analyses between the concentration  $C$  of the pore fluids and the corresponding backscattering area  $A$  were performed with Matlab (R2021b, MathWorks, Natick, Massachusetts, USA). Slope comparison of the linear regression was made using analysis of variance (ANOVA). Logarithmic regressions between pore diameter and area  $A$  were done in Origin software (Origin2000, OriginLab, Northampton, Massachusetts, USA). The root mean square error (RMSE) and relative root mean square error (RRMSE) were reported as measures of model accuracy (Despotovic et al., 2016). Multiple regression was applied using Matlab's curve fitting toolbox (3.6, MathWorks, Natick, Massachusetts, USA) with the backscattering area  $A$  as the dependent variable, pore diameter  $P$  as one independent variable, and the refractive index difference (RID) between the solutions and the porous disc material as the other independent variable. The significance level of all statistics in this study was  $p \leq 5\%$ .

## 2.4 Results

### 2.4.1 Influence of pore size

The influence of the pore size (P1.6 – P160) on LBI is shown in Figure 2.5 for porous discs soaked with distilled water (blanks). Figure 2.5a shows the images of P16 and P40 were similar, while the others displayed clear differences. Furthermore, the central white light spots were the largest for P16 and P40 while the central light spots for P160 and P100 in contrast were very weak. The edges of the circular light rings around the central light spots generally became more blurred with increasing pore diameters. Finally, P160 with the largest pores had no clear round boundary shape. Contrary to this, P1.6 revealed a relatively large and sharp central light spot with a rather small surrounding light ring, which has a clear and sharp edge. The data plots in Figure 2.5 show the derived grey value profiles with differences between the pore diameters, even for P16 and P40 at radii between 5 and 11 mm. Finally, it suggests that the backscattering area has a logarithmic relationship for pore diameter P1.6 – P100, with the highest regression p-value of 1.6 %. However, P160 with the largest pores did not fit this

relationship. The behavior of the three different wavelengths were similar in the study.

### **2.4.2 Influence of type and concentration of solute**

The influence of the solutes (NaCl and NaH<sub>2</sub>PO<sub>4</sub>) and their concentrations is shown in Figure 2.6 for pore size P100 and the laser wavelength of 635 nm. Figure 2.6a shows the sigmoidal radial profiles of the grey values. The solute-induced effects are shown by the differences between the grey value obtained with distilled water and with the respective solute concentrations (Figure 2.6b). Linear regression was performed between the solute concentration and the grey value for the different radii. The coefficient of determination ( $R^2$ ) and slope of the regression are shown in Figure 2.6c. Between 0.5 and 9.5 mm from the center, the  $R^2$  values were above 0.8. The corresponding absolute slopes of the regression revealed the lowest values between 4 mm and 8 mm from the center compared to the neighboring regions.

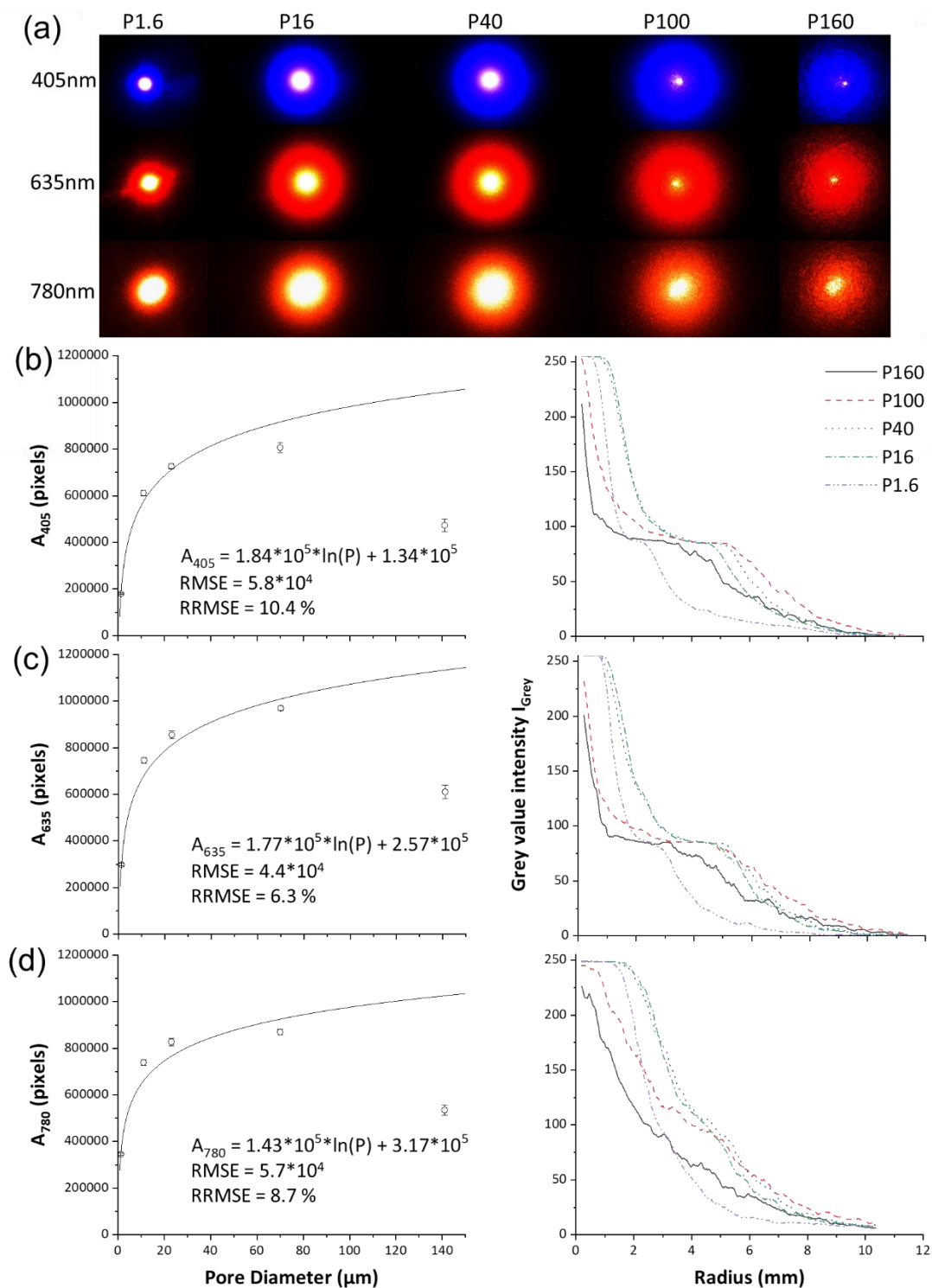


**Figure 2.5** LBI of porous discs of different pore size saturated with distilled water: (a) RGB images of P1.6 – P160; and correlation between backscattering area and pore diameter  $P$ ; and intensity profiles for 450 nm (b), 635 nm (c), and 780 nm (d). The logarithm regression lines were estimated omitting P160 as an outlier. RMSE represents root mean square error, RRMSE represents relative root mean square error.

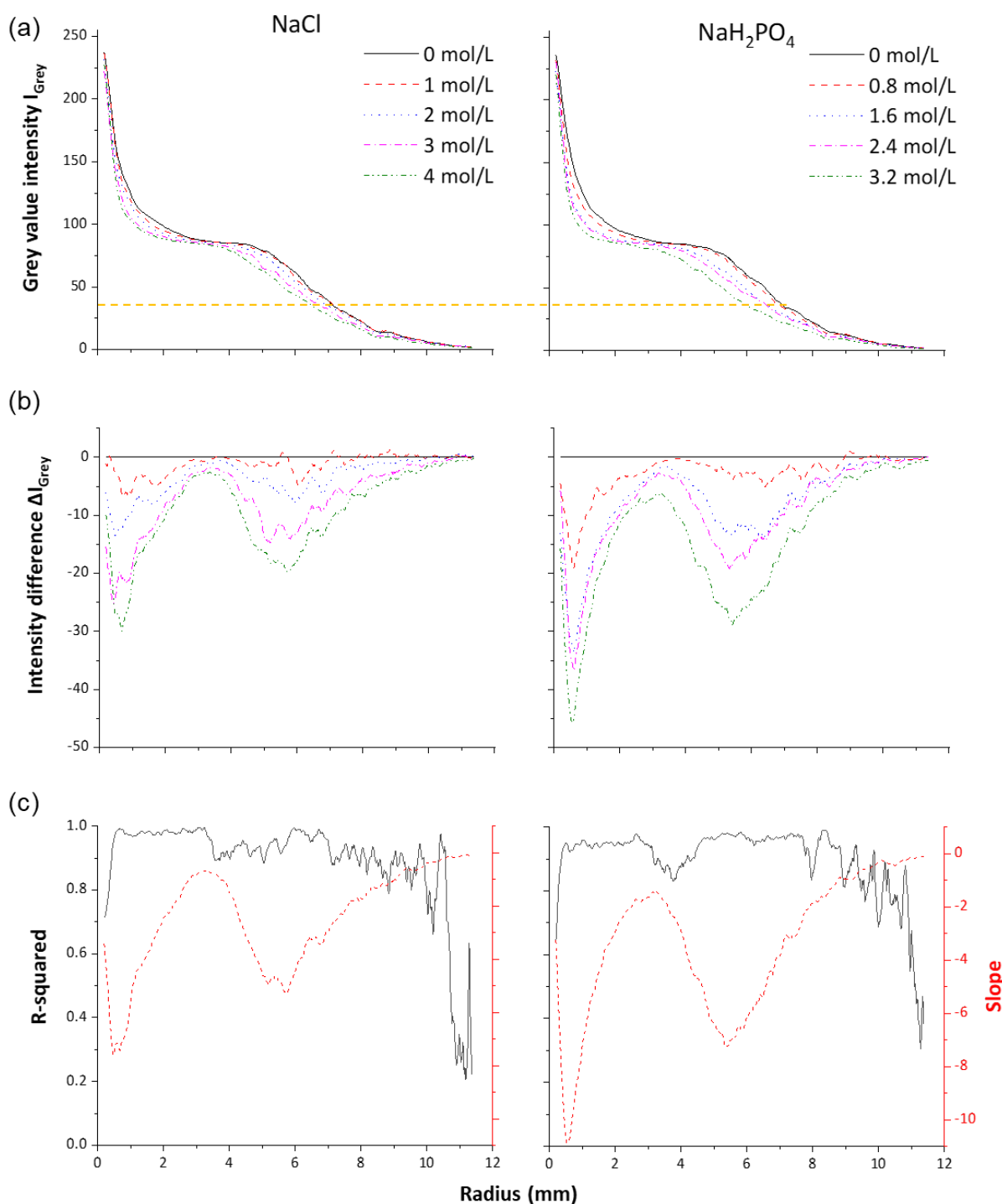


**Figure 2.6** (a) Grey value intensity profiles at 635 nm of P100 saturated with NaCl and NaH<sub>2</sub>PO<sub>4</sub> solution with five different concentrations; (b) grey value intensity differences between results obtained with different concentrations and distilled water; and (c) R<sup>2</sup> and slope of linear regression between concentration and intensity at different radii, with the solid curve representing R<sup>2</sup> and the dotted curve representing slope.

### 2.4.3 Synopsis of pore size, solute and wavelength

Figure 2.7 summarizes the effects of: i) five pore sizes (P1.6-P160), ii) two solutes (NaCl, NaH<sub>2</sub>PO<sub>4</sub>) and varying concentrations and iii) three laser light wavelengths (405, 635 and 780 nm) in the backscattering area *A*. In general, different wavelengths did not cause distinctive scattering pattern differences in LBI. Even though the backscattering area changed with the wavelength due to differences in laser light energy, the trends of the correlations between backscattering area and the different concentrations of the saline solutions were similar. In contrast, changes in pore diameter led to clear differences in the trend of the regression lines. The differences are particularly evident between P160 and P100 with a negative correlation and P40, P16 and P1.6 with positive position. ANOVA was applied to distinguish if a significant slope difference existed between the two solutions. In P160 and P100, the p-values were lower than 0.3 %. In contrast, in P40, P16 and P1.6, all the p-values were higher than 5 %, except for P1.6 with blue laser.

For all porous discs wavelengths, and solutes, the backscattering area showed significant linear relationships. The highest coefficient of determination ( $R^2=0.98$ ) was found using the P160 with the NaH<sub>2</sub>PO<sub>4</sub> solution, while the lowest  $R^2$  of 0.50 was observed with P40 (Table 2.2). When the pore size and wavelength were fixed, the p-values for the linear regression between the refractive index difference (*RID*) and area *A*, were below 0.04 %. Table 2.3 shows the interactive effect of pore diameter *P* and *RID* between solutions and porous disc material. According to equations in Table 2.3, the influence of the *RID* is linear. However, the influence of pore diameter *P* contains two parts: When pore diameter *P* is small, the term  $\ln(P)$  has greater influence than *P*; when pore diameter *P* is bigger, the influence of *P* takes over.

**Table 2.2 Coefficient of determination ( $R^2$ ) for linear relationships between concentration and backscattering area  $A$  (data of Figure 2.7).**

		P160	P100	P40	P16	P1.6
405 nm	NaCl	0.91	0.82	0.56	0.76	0.92
	NaH <sub>2</sub> PO <sub>4</sub>	0.98	0.92			0.89
635 nm	NaCl	0.93	0.86	0.59	0.71	0.81
	NaH <sub>2</sub> PO <sub>4</sub>	0.98	0.87			
780 nm	NaCl	0.93	0.83	0.50	0.68	0.88
	NaH <sub>2</sub> PO <sub>4</sub>	0.98	0.94			

**Table 2.3 Regression equations for backscattering area  $A$  as a function of pore diameter  $P$  ( $\mu\text{m}$ ) and refractive index difference RID between solutions and porous disc material.**

Wavelength (nm)	Equation	$R^2$	Adjusted $R^2$
405 (blue)	$A_{405} = 1.99 \times 10^6 * RID * \ln(P) - 5.88 \times 10^4 * RID * P + 1.40 \times 10^5$	0.90	0.89
635 (red)	$A_{635} = 2.07 \times 10^6 * RID * \ln(P) - 6.29 \times 10^4 * RID * P + 2.72 \times 10^5$	0.87	0.87
780 (infrared)	$A_{780} = 1.75 \times 10^6 * RID * \ln(P) - 5.85 \times 10^4 * RID * P + 3.42 \times 10^5$	0.86	0.86

**Table 2.4 Reported cell sizes found in common horticultural crops: apple, cucumber and potato.**

Food variety	Unit	Outer layer	Middle layer	Inner layer
Apple cv. Granny Smith (Bain and Robertson, 1951)	$\mu\text{m}$	100	60	110
Cucumber cv. Corona (Marcelis and Baan Hofman-Eijer, 1993)	Relative unit	0.7	1.2	0.6
Potato cv. Russet Burbank (Reeve et al., 1971)	$\mu\text{m}$	160-220	200-300	180 -240

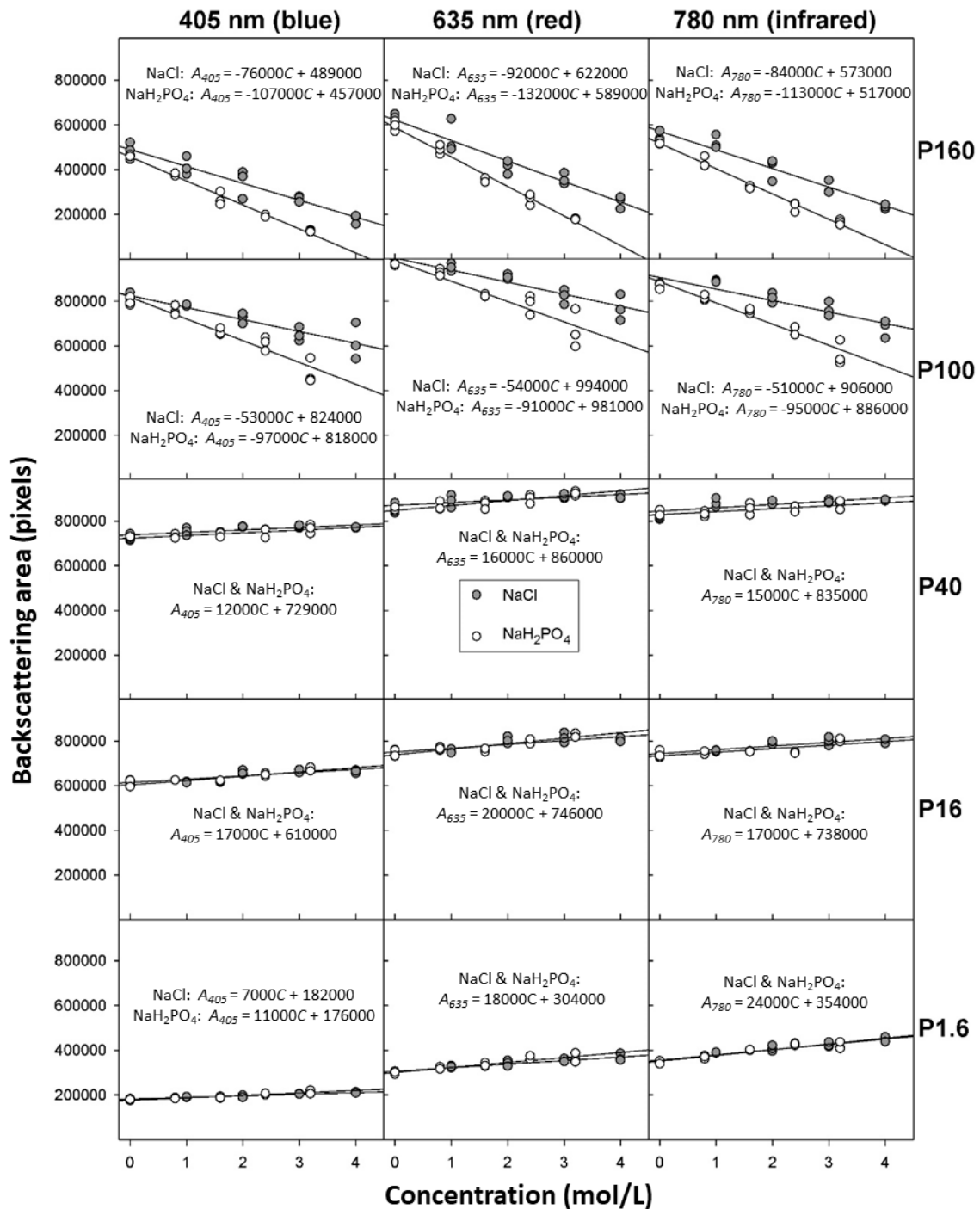


**Figure 2.7** Correlations of backscattering area  $A$  and two different saline solutions (NaCl, NaH<sub>2</sub>PO<sub>4</sub>) with varying concentrations  $C$  for five different pore diameters (P1.6 – P160) and three different laser light wavelengths (405, 635, 780 nm). Joint regression equations for both NaCl and NaH<sub>2</sub>PO<sub>4</sub> were given when the slope of NaCl and NaH<sub>2</sub>PO<sub>4</sub> were not significantly different.



## 2.5 Discussion

### 2.5.1 Backscattering area

The backscattering area  $A$  was used to compare the influence of the experimental treatment levels (i.e. different pore size, pore filling and wavelengths) on LBI. Observably, not all of the backscattered signal should be used for the evaluation. For example, information derived from the central white or bright yellow light spot of the RGB image reflects the erroneous color image acquisition of the camera due to overexposure. This is demonstrated in Figure 2.6, which shows that there are differences in the grey value intensity in the first 3 mm from the center, reflecting concentration variances caused solely by differences in blue and green light intensity, which do not actually exist but are displayed on the RGB image. Hence, these data were not used. It is worth mentioning that this imaging information might also be suitable for LBI differentiation in further research. According to present results, the best image information is found in the subsequent concentric regions where the light intensity of the applied wavelength falls below its maximum value (grey value intensity  $< 85$ ). Here LBI differences are only caused by varying lateral light propagation of the laser light used. This is evident e.g. in Figure 2.6b, where the grey value intensities indicate different salt concentrations. It could be confirmed that the grey value profiles are different in their shape, as already described in the literature (Lorente et al., 2015; Romano et al., 2008, 2011) and that certain sections along the radial profiles could be influenced by the different experimental treatments as also found by Van Beers et al. (2015). In this study, it was additionally shown, that grey values below 85 were suitable for LBI differentiation and that backscattering area  $A$  was a suitable indicator for differences in pore size and pore filling.

### 2.5.2 Influencing and non-influencing experimental factors

The results revealed that three of the four investigated experimental factors influence LBI, specifically: (i) the pore diameter, (ii) the solutes and (iii) their concentrations. In contrast, the different laser light wavelengths applied in the blue, red and infrared range did not cause any

obvious LBI pattern differences. Regarding pore diameter, the highest p-value among the three regressions was 1.6 %. Thus, the influence of pore diameter was confirmed. Regarding the solute, the influence could be confirmed for P160 and P100 by slope comparison with p-values smaller than 5 %. However, no significant differences could be found for P1.6, P16 and P40 (Figure 2.7). Regarding solute concentration, the influence could be demonstrated because all the p-values for the linear regression were below 5 %. The correlations determined with LBI for pore diameter and solutes are partly consistent with findings of Tu et al. (2000), who found smaller backscattering areas on tomatoes with smaller intercellular spaces. Romano et al. (2011) argued that decreasing backscattering areas on apples during drying were caused by the shrinking tissue (i.e. reduced cells size). Qing et al. (2008) could predict dissolved solid constituents in fresh apples with LBI.

The structured research approach of this study allowed targeted investigations on the influence of pore diameter and solutes on LBI. The influence of pore diameter on LBI is visible in Figure 2.5. Theoretically, the scattering area is bigger as the pore size increases, however, in practice this effect is weakened due to the following two reasons: i) the detector has limitations in detecting low-intensity light when it is scattered over a large area; ii) increasing scattering also leads to an increase in light transmission through the porous discs. These reasons might explain the logarithmic relationship between backscattering area  $A$  and pore diameter. Specifically, light penetrates less deeply in porous discs with smaller pores, because it is already scattered to a larger extend in the uppermost area of the discs. This explanation fits the everyday experience: many materials are transparent when whole but when powdered they appear white rather than transparent. Similarly, less laser light traveled to the backside of cheese during curdling due to the pore diameter contraction (Verdú et al., 2021). However, due to this low penetration depth, more light can escape through the top of the porous disc. This phenomenon is visible in the form of a larger white central light spot and contribute to a smaller backscattering area due to less light being available within the porous discs. An exception was P160 with the largest pores. It showed the smallest white central light spot and no clear round boundary shape, as also reported by Qin and Lu (2009), which can be explained by the depth of light penetration. But contrary to expectations, P160 did not show the largest but second-smallest backscattering area. This observation can be explained by the

fact that the light penetrates very deeply through the larger pores and could transmit through the porous discs. Consequently, light losses through the bottom of the porous discs, as seen by a visible light circle on the bottom surface and more unregular edge of the LBI for P160 (Figure 2.5), reduced the remaining available light to such an extent that the lateral light propagation within the porous discs was strongly reduced.

As the concentration of NaCl or NaH<sub>2</sub>PO<sub>4</sub> in the solution increases, the refractive indexes difference inside the porous glass discs becomes smaller (Figure 2.2). This reduces refraction and supports light propagation within the porous disc and thus the backscattering area becomes larger. A corresponding increase of backscattering area can be observed for P40, P16 and P1.6 (Figure 2.7). According to equations in Table 2.3, when  $R/D$  is equal to 0, pore diameter  $P$  will lose influence. This phenomenon is also known as “refractive index matching”. Further research should try to consider sample thickness as an influencing factor to complete these equations. It should be noted however, that this explanation is based on refractive indexes measured at 589 nm. Since no obvious influence of the wavelength was detected, the validity of these values under conditions of this study could be assumed.

Table 2.4 illustrates the cell size distribution along a transection radius of apple, potato and cucumber. In addition, the cell sizes will certainly vary between different cultivars and growth stages. Based on the finding of this research, the influence of cell size at different depths from the fruit skin surface deserves more attention. For example, if LBI is used to detect pore size or the liquid refractive index in apples, the laser light might reach the middle layer for small apples but only the outer layer for large apples. In this case, applying additional correction factors based on apple size is a possible direction to increase the accuracy of LBI systems on fruit measurements. Furthermore, addressing fruit surface curvature is another important research direction in LBI (Qing et al., 2007). The cylindrical shape porous discs used in this research are available at different thickness and diameter. Using the cylindrical surface in addition to the plain surface might help to gain knowledge about the influence of the surface curvature under controlled conditions.

## 2.6 Conclusions

Though no influence of wavelength was found, pore diameter and solution as solution properties were confirmed to dynamically influence LBI. When the solution concentration was zero, the pore diameter (1-100  $\mu\text{m}$ ) seemed to have a logarithm relationship with backscattering area. When pore diameter was fixed, backscattering area was influenced by solution concentration in a linear way. However, the linear trend could be positive or negative depending on the pore diameter. Refractive index difference between the solutions and the porous matrix could explain the phenomenon. The difference in refractive index became low when solution concentration increased and resulted in longer light transmission depth. This helped to increase the backscattering area. However, when the depth was larger than the thickness of the matrix, light escaped from the backside of the disc, changing the trend of the linear relationship from positive to negative.

In practice, this research demonstrates the importance of cell size when applying LBI to horticultural crops. Any postharvest process with significant cell size change might influence the measurements with LBI. Furthermore, the intensity profile along the radius of the back scattering area showed potential to measure the solution concentration of the pore fluid. Further research should focus on the impact of sample thickness, the transmission image at material backside, more solutes with different refractive index and special radii of interest to test for surface curvature.

### **Declaration of competing interest**

The authors report no potential conflict of interest.

### **Acknowledgements**

This work was financially supported by the China Scholarship Council (No. 201406350068). Special thanks to Alice Reineke and Ute Waldeck for their technical support as well as to Kiat Intani, Zhichong Wang and Sebastian Romuli for their helpful suggestions.

## 2.7 References

- Adebayo, S. E., Hashim, N., Abdan, K., & Hanafi, M. (2016). Application and potential of backscattering imaging techniques in agricultural and food processing – A review. *Journal of Food Engineering*, 169, 155–164. <https://doi.org/10.1016/J.JFOODENG.2015.08.006>
- Bai, J. W., Zhang, L., Cai, J. R., Wang, Y. C., & Tian, X. Y. (2021). Laser light backscattering image to predict moisture content of mango slices with different ripeness during drying process. *Journal of Food Process Engineering*, 44(12), 1–10. <https://doi.org/10.1111/jfpe.13900>
- Bain, J. M., & Robertson, R. N. (1951). The physiology of growth in apple fruits. I. Cell size, cell number, and fruit development. *Australian Journal of Scientific Research. Ser. B: Biological Sciences*, 4(2), 75–107. <https://doi.org/10.1071/bi9510075>
- Baranyai, L., & Zude, M. (2008). Analysis of laser light migration in apple tissue by Monte Carlo simulation. *Progress in Agricultural Engineering Sciences*, 4(1), 45–59. <https://doi.org/10.1556/Progress.4.2008.3>
- Baranyai, L., & Zude, M. (2009). Analysis of laser light propagation in kiwifruit using backscattering imaging and Monte Carlo simulation. *Computers and Electronics in Agriculture*, 69(1), 33–39. <https://doi.org/10.1016/j.compag.2009.06.011>
- Despotovic, M., Nedic, V., Despotovic, D., & Cvetanovic, S. (2016). Evaluation of empirical models for predicting monthly mean horizontal diffuse solar radiation. *Renewable and Sustainable Energy Reviews*, 56, 246–260. <https://doi.org/10.1016/j.rser.2015.11.058>
- Glover, F. A., & Goulden, J. D. S. (1963). Relationship between refractive index and concentration of solutions. *Nature*, 200, 1165–1166. <https://doi.org/10.1038/2001165a0>
- Hashim, N., Pflanz, M., Regen, C., Janius, R. B., Abdul Rahman, R., Osman, A., Shitan, M., & Zude, M. (2013). An approach for monitoring the chilling injury appearance in bananas by means of backscattering imaging. *Journal of Food Engineering*, 116(1), 28–36. <https://doi.org/10.1016/j.jfoodeng.2012.11.018>
- Hussain, A., Pu, H., & Sun, D. W. (2018). Innovative nondestructive imaging techniques for ripening and maturity of fruits – A review of recent applications. *Trends in Food Science and Technology*, 72, 144–152. <https://doi.org/10.1016/j.tifs.2017.12.010>
- Haynes, W. M. (Ed.). (2014). *Thermochemistry, Electrochemistry, and Solution Chemistry*. In *CRC Handbook of Chemistry and Physics (95th ed.)*, CRC Press, Boca Raton, pp. 142,144
- ISO 4793. (1980). Laboratory sintered (fritted) filters — Porosity grading, classification and designation.

Lorente, D., Zude, M., Idler, C., Gómez-Sanchis, J., & Blasco, J. (2015). Laser-light backscattering imaging for early decay detection in citrus fruit using both a statistical and a physical model. *Journal of Food Engineering*, 154, 76–85. <https://doi.org/10.1016/j.jfoodeng.2015.01.004>

Lorente, D., Zude, M., Regen, C., Palou, L., Gómez-Sanchis, J., & Blasco, J. (2013). Early decay detection in citrus fruit using laser-light backscattering imaging. *Postharvest Biology and Technology*, 86, 424–430. <https://doi.org/10.1016/j.postharvbio.2013.07.021>

Marcelis, L. F. M., & Baan Hofman-Eijer, L. R. (1993). Cell division and expansion in the cucumber fruit. *Journal of Horticultural Science*, 68(5), 665–671. <https://doi.org/10.1080/00221589.1993.11516398>

Martelli, F., Binzoni, T., Pifferi, A., Spinelli, L., Farina, A., & Torricelli, A. (2016). There's plenty of light at the bottom: statistics of photon penetration depth in random media. *Scientific Reports*, 6(1), Article 27057. <https://doi.org/10.1038/srep27057>

McGlone, V. A., Abe, H., & Kawano, S. (1997). Kiwifruit firmness by near infrared light scattering. *Journal of Near Infrared Spectroscopy*, 5(2), 83–89. <https://doi.org/10.1255/jnirs.102>

Mohd Ali, M., Hashim, N., & Abdul Hamid, A. S. (2020a). Combination of laser-light backscattering imaging and computer vision for rapid determination of oil palm fresh fruit bunches maturity. *Computers and Electronics in Agriculture*, 169, Article 105235. <https://doi.org/10.1016/j.compag.2020.105235>

Mohd Ali, M., Hashim, N., Bejo, S. K., & Shamsudin, R. (2020b). Comparison of laser backscattering imaging and computer vision system for grading of seedless watermelons. *Journal of Food Measurement and Characterization*, 14(1), 69–77. <https://doi.org/10.1007/s11694-019-00268-4>

Mollazade, K., Omid, M., Tab, F. A., & Mohtasebi, S. S. (2012). Principles and Applications of Light Backscattering Imaging in Quality Evaluation of Agro-food Products: a Review. *Food and Bioprocess Technology*, 5, 1465–1485. <https://doi.org/10.1007/s11947-012-0821-x>

Onwude, D. I., Hashim, N., Abdan, K., Janius, R., & Chen, G. (2018). The potential of computer vision, optical backscattering parameters and artificial neural network modelling in monitoring the shrinkage of sweet potato (*Ipomoea batatas* L.) during drying. *Journal of the Science of Food and Agriculture*, 98(4), 1310–1324. <https://doi.org/10.1002/jsfa.8595>

Qin, J., & Lu, R. (2009). Monte Carlo simulation for quantification of light transport features in apples. *Computers and Electronics in Agriculture*, 68(1), 44–51. <https://doi.org/10.1016/j.compag.2009.04.002>

Qing, Z., Ji, B., & Zude, M. (2007). Predicting soluble solid content and firmness in apple fruit by means of laser light backscattering image analysis. *Journal of Food Engineering*, 82(1), 58–67. <https://doi.org/10.1016/j.jfoodeng.2007.01.016>

Qing, Z., Ji, B., & Zude, M. (2008). Non-destructive analyses of apple quality parameters by means of laser-induced light backscattering imaging. *Postharvest Biology and Technology*, 48(2), 215–222. <https://doi.org/10.1016/j.postharvbio.2007.10.004>

Reeve, R. M., Timm, H., & Weaver, M. L. (1971). Cell size in Russet Burbank potato tubers with various levels of nitrogen and soil moisture tensions. *American Potato Journal*, 48(12), 450–456. <https://doi.org/10.1007/BF02862060>

ROBU Glasfilter- Geräte GmbH. (2022a). Poreneigenschaften Und Permeabilität. Retrieved from <https://www.robuglas.com/service/downloads.html>. Accessed June 9, 2022

ROBU Glasfilter- Geräte GmbH. (2022b). Technische Daten. Retrieved from <https://www.robuglas.com/service/technische-daten.html>. Accessed June 9, 2022

Romano, G., Argyropoulos, D., Nagle, M., Khan, M. T., & Müller, J. (2012). Combination of digital images and laser light to predict moisture content and color of bell pepper simultaneously during drying. *Journal of Food Engineering*, 109(3), 438–448. <https://doi.org/10.1016/J.JFOODENG.2011.10.037>

Romano, G., Baranyai, L., Gottschalk, K., & Zude, M. (2008). An approach for monitoring the moisture content changes of drying banana slices with laser light backscattering imaging. *Food and Bioprocess Technology*, 1(4), 410–414. <https://doi.org/10.1007/s11947-008-0113-7>

Romano, G., Nagle, M., Argyropoulos, D., & Müller, J. (2011). Laser light backscattering to monitor moisture content, soluble solid content and hardness of apple tissue during drying. *Journal of Food Engineering*, 104(4), 657–662. <https://doi.org/10.1016/j.jfoodeng.2011.01.026>

Sanchez, P. D. C., Hashim, N., Shamsudin, R., & Mohd Nor, M. Z. (2020a). Laser-light backscattering imaging approach in monitoring and classifying the quality changes of sweet potatoes under different storage conditions. *Postharvest Biology and Technology*, 164, Article 111163. <https://doi.org/10.1016/j.postharvbio.2020.111163>

Sanchez, P. D. C., Hashim, N., Shamsudin, R., & Mohd Nor, M. Z. (2020b). Potential application of laser-based imaging technology in the quality evaluation of agricultural products : A review. *Advances in Agricultural and Food Research Journal*, 1(2). <https://doi.org/10.36877/aafjr.a0000127>

Tu, K., Jancsok, P., Nicolai, B., & De Baerdemaeker, J. (2000). Use of laser-scattering imaging to

study tomato-fruit quality in relation to acoustic and compression measurements. *International Journal of Food Science and Technology*, 35(5), 503–510. <https://doi.org/10.1046/j.1365-2621.2000.00407.x>

Udomkun, P., Nagle, M., Mahayothee, B., & Müller, J. (2014). Laser-based imaging system for non-invasive monitoring of quality changes of papaya during drying. *Food Control*, 42, 225–233. <https://doi.org/10.1016/j.foodcont.2014.02.010>

Van Beers, R., Aernouts, B., León Gutiérrez, L., Erkinbaev, C., Rutten, K., Schenk, A., Nicolaï, B., & Saeys, W. (2015). Optimal Illumination-Detection Distance and Detector Size for Predicting Braeburn Apple Maturity from Vis/NIR Laser Reflectance Measurements. *Food and Bioprocess Technology*, 8(10), 2123–2136. <https://doi.org/10.1007/s11947-015-1562-4>

Verdú, S., Gallego, M., Barat, J. M., Talens, P., & Grau, R. (2022). Modelling in vitro gastrointestinal digestion of egg white gel matrix by laser-backscattering imaging. *Journal of Food Engineering*, 316, Article 110839. <https://doi.org/10.1016/j.jfoodeng.2021.110839>

Verdú, S., Perez, A. J., Barat, J. M., & Grau, R. (2021a). Laser-backscattering imaging for characterising the dairy matrix in different phases during curd processing. *Food Control*, 128, Article 108193. <https://doi.org/10.1016/j.foodcont.2021.108193>

Verdú, S., Pérez, A. J., Barat, J. M., & Grau, R. (2019). Laser backscattering imaging as a control technique for fluid foods: Application to vegetable-based creams processing. *Journal of Food Engineering*, 241, 58–66. <https://doi.org/10.1016/j.jfoodeng.2018.08.003>

Verdú, S., Pérez, A. J., Barat, J. M., & Grau, R. (2021b). Non-destructive control in cheese processing: Modelling texture evolution in the milk curdling phase by laser backscattering imaging. *Food Control*, 121, Article 107638. <https://doi.org/10.1016/j.foodcont.2020.107638>



# 3

## **Investigating crude sesame oil sedimentation and its monitoring using laser backscattering imaging (LBI)**

Zhangkai Wu <sup>a</sup>, Sebastian Romuli <sup>a</sup>, Kiatkamjon Intani <sup>a,b</sup> and Joachim Müller <sup>a</sup>

<sup>a</sup> University of Hohenheim, Institute of Agricultural Engineering,  
Tropics and Subtropics Group, Stuttgart, 70599, Germany

<sup>b</sup> Kasetsart University, Faculty of Agriculture,  
Department of Farm Mechanics, Bangkok 10900, Thailand

*Published in Applied Sciences (Switzerland), 13(15), August 2023*  
<https://doi.org/10.3390/app13159013>

### 3.1 Abstract

Sesame oil is a food and energy resource that is not used enough. Sedimentation of crude oil after pressing can remove particles and happens regardless of the producer's intention. However, sedimentation of crude plant oil and its sensing technology are rarely studied. This research studied crude sesame oil sedimentation and monitored it with low-cost laser backscattering imaging (LBI). In the discontinuous measurement, a 30-day sedimentation was conducted with oil samples sent to the lab LBI system for image capture. A scattering spot and an increasing Tyndall effect along the light path were seen. In the continuous measurement, an LBI system was mounted on a sedimentation tank for 30 days. The sedimentation curve, scattering images, and oil properties were checked. The sedimentation speed was about  $-7$  mm/h, then less than  $-2$  mm/h. The image features correlated well with the sedimentation interface height ( $R^2 = 0.97$ ) when the height was above  $-100$  mm. The oil-particle-related properties (ash content, phosphorus content, carbon residue, and total contamination) dropped by at least 87%, water content decreased by 90%, and the oxidation-related properties (oxidation stability,  $\gamma$ -tocotrienol,  $\delta$ -tocopherol,  $\gamma$ -tocopherol, and acid value) changed less significantly. The crude sesame oil sedimentation had two stages: diluted and hindered sedimentation. This research can help improve sedimentation tank and LBI system design and prevent unwanted sedimentation.

### 3.2 Introduction

In 2020, global sesame oil production was 1 million metric tons, with Sudan being the leading producer of sesame seeds [1]. Sesame oil is widely known for its use in the cosmetic industry, cooking, and medicine [2–4]. Langyan et al. suggested that the nutritional and health benefits of sesame oil are not fully utilized [5]. Furthermore, due to the growing demand for renewable energy, researchers are considering using sesame oil as a source of biodiesel [6–8].

Gravity separation, also known as sedimentation [9], is a simple method for removing solid impurities from crude plant oil [10,11]. It is a physical process where suspended solid particles in a liquid undergo gravitational settling and accumulate at the bottom of the container, resulting in a clearer supernatant. Sedimentation for crude oil purification is not commonly

used in the industry due to its low efficiency, while the filtration process is prevalent [10,12]. However, Altieri et al. suggested that applying an assisted sedimentation system could save energy and improve olive oil quality on an industrial scale [13]. Additionally, sedimentation is a suitable method to reduce total contamination in plant oil for energy use in rural areas [14,15]. Short term oil sedimentation could be used as a preprocessing step before filtering [16]. In the last decade, the technology for designing sedimentation tanks has developed a lot in the field of treating wastewater [17], which has the potential to also benefit the design of oil sedimentation tanks. Notably, once plant oils are pressed and stored in a container, sedimentation occurs regardless of the producer's intention. For instance, sediment in unrefined oil products requires additional explanation from sellers to reassure consumers [18]. The fundamental theory of sedimentation in physics indicates that the sedimentation process might encompass several distinct stages. These stages include diluted sedimentation, which is characterized by a constant sedimentation speed, and hindered sedimentation, distinguished by the evolution of a distinct supernatant–sediment interface [19]. However, the sedimentation process could vary depending on practical situations. For example, Pietsch et al. found that no diluted sedimentation occurred in a biogas fermenter due to the fibrous structure of the substrate particles [20]. Few studies have been conducted to investigate the sedimentation stages of plant oil; therefore, further research is needed to help maximize the potential use and minimize the drawbacks.

Laser backscattering imaging (LBI) is a non-destructive optical technique that exploits the scattering effect of porous objects when illuminated by a laser beam. The resulting scattering pattern images are analyzed to extract object information. LBI exhibits potential in numerous agricultural domains [21–23]. Since the concentration of suspended solid particles in sedimentation fluctuates, LBI may have the potential to monitor the oil sedimentation process. Additionally, the affordability and non-invasive nature of LBI make it particularly suitable for application in rural areas or small scale factories. Thus, the objective of this study was to investigate the crude sesame oil sedimentation process with an LBI system.

## **3.3 Materials and Methods**

### **3.3.1 Sesame Oil**

Sesame seeds (Sesame S42 White) were imported from Bobo-Dioulasso (Burkina Faso). The seeds, with an initial moisture content of 3%, were remoistened to 8% at 10 kg per unit, by adding distilled water as described in [24]. Sesame oil was mechanically extracted by pressing the seeds with a spindle press (KK20 F Universal, Kern Kraft oil press GmbH & Co. KG, Reut, Germany) and stored in 10 L containers.

### **3.3.2 Experimental Setup for Discontinuous LBI Measurement**

A discontinuous LBI measurement experiment was conducted to investigate the interaction between the laser and sesame oil during the sedimentation process. The sedimentation lasted for 30 days, with the room temperature ranging from 20 to 25 °C. Twenty-nine liters of crude sesame oil, stored at a temperature below 5 °C, was warmed up under room temperature for 24 h and then poured into a 30 L open container. The container was left open to promote oxidation of the oil. A stirrer was used to homogenize the oil. At Day 0, Day 5, Day 20, and Day 30, oil samples were taken out from the top of the sedimentation tank and filled in transparent plastic cylindrical bottles (34 mm diameter, 69 mm height) at a height of 66 mm for the LBI system to capture images. The LBI system in a black box, as illustrated in Figure 3.1, consisted of two lasers with wavelengths of 635 nm (LFD635-1-3, Picotronic, Koblenz, Germany) and 405 nm (DD405-1-3, Picotronic, Koblenz, Germany), and a camera (PX5-CM, PAX cam, Villa Park, IL, USA) equipped with a zoom lens. The size of the images was 2592 × 1944 pixels. The distance between the camera lens and the surface of the oil sample was 190 mm, enlarging the scattering phenomenon while ensuring that the image boundary was not exceeded. To ensure stable laser light during measurement, the laser was turned on for a minimum of 15 min before image capture.

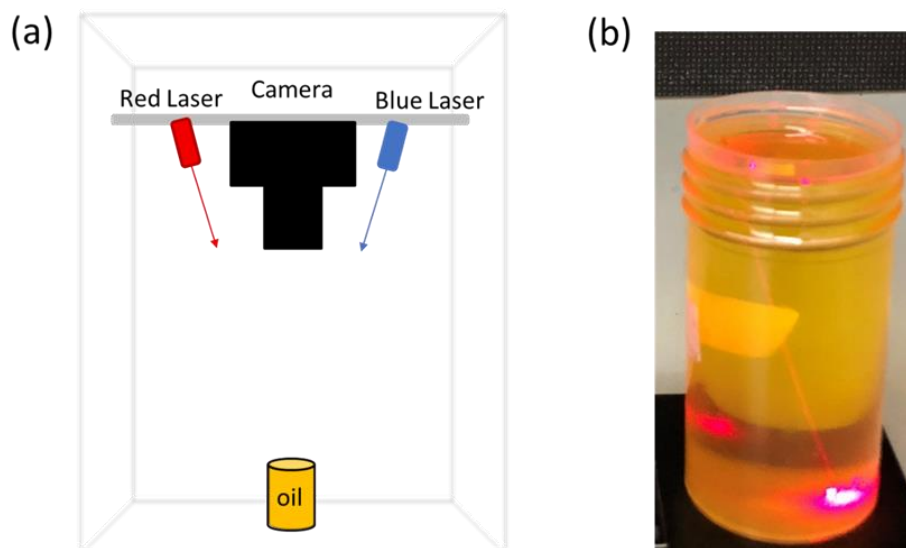


**Figure 3.1** (a) The imaging system setup employed for discontinuous LBI (laser backscattering imaging) measurement; (b) the experimental phenomena with clean sesame oil when subjected to red laser illumination.

### 3.3.3 Experimental Setup for Continuous LBI Measurement

In addition, an LBI system was directly mounted on a sedimentation tank to perform continuous LBI measurements during the sedimentation process (Figure 3.2). The sedimentation process lasted for 30 days; during the experiment, the oil temperature was  $21 \pm 3$  °C. About 120 L of pressed crude oil was homogenized and poured into a transparent acrylic glass cylindrical tank (500 mm diameter, 1000 mm height), with a transparent acrylic glass lid put on the top. The crude oil height in the tank was 592 mm. The LBI system mounted on top of the tank consisted of a red laser (DC650-1-3-HT-CON-JST, Picotronic, Koblenz, Germany) and camera 1 (ELP-USBFHD01M-BFV, Ailipu, Shenzhen, China). To minimize the direct laser light reflection and at the same time optimize the laser light penetration into the sesame oil, the incident angles of the lasers were set at  $15^\circ$  to vertical direction [21]. The image taken by camera 1 had a size of 1920 x 1080 pixels with a resolution of 0.3 mm/pixel. A one-meter rule was pasted onto the oil tank, and camera 2 and camera 3 (same type as camera 1) were mounted at side positions to observe the interface between sediment and supernatant. All three cameras and lights were connected to a computer. As cameras 2 and 3 could not capture the complete view of the tank, manual images were taken from a larger distance every 24 h. Images were automatically taken every hour by camera 2 and camera 3

to measure the sediment's height. Afterwards, the light was automatically turned off for camera 1 to take an LBI image. When the oil interface height changed by 1 mm or more, the corresponding time was recorded. Both the time and interface height were used for further data analysis.

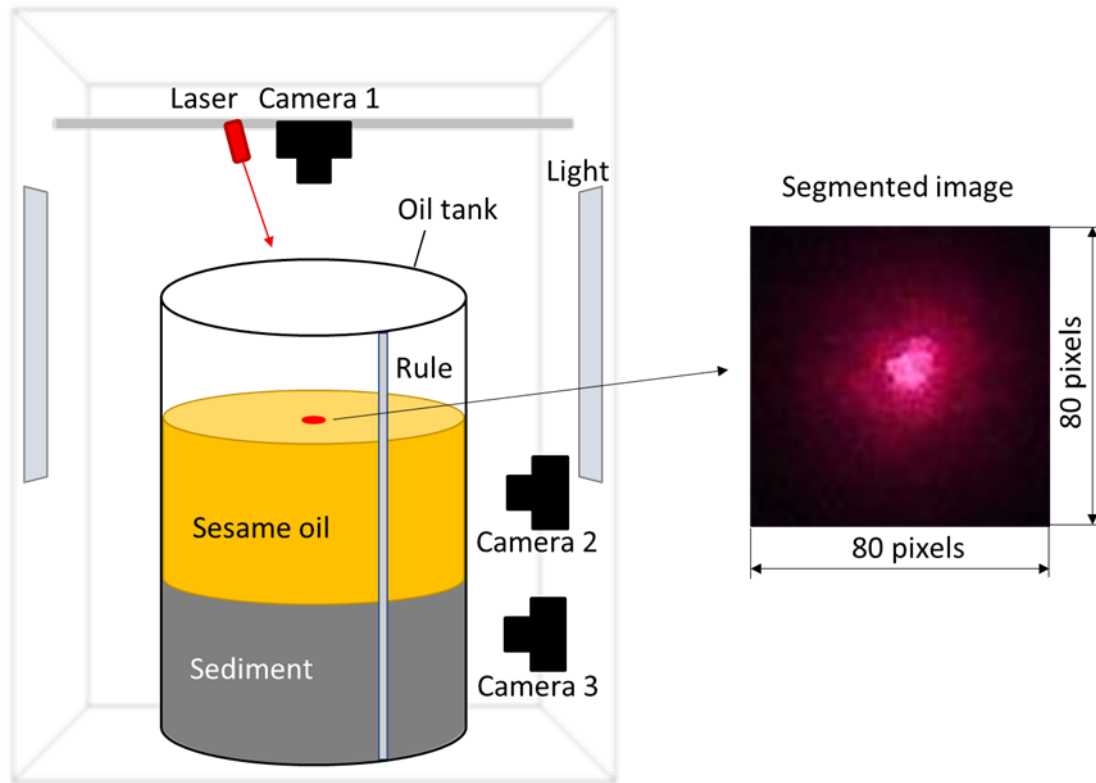


**Figure 3.2** The system setup used for continuous LBI measurements, with an example image captured by camera 1 and segmented by an  $80 \times 80$  pixel box.

### 3.3.4 Image Analysis

For the analysis of the LBI images in the continuous experiment, an  $80 \times 80$  pixel box at a fixed position in the image was used to segment the backscattering area from the background (Figure 3.2) followed by a  $3 \times 3$  median filter to reduce the noise in the images. The mean grey value of the segmented image was used as the feature of the LBI images:

$$I_{mean} = \frac{I_R + I_G + I_B}{3} \times \frac{1}{80 \times 80} \quad (3-1)$$

where  $I_R$ ,  $I_G$ ,  $I_B$  are the red, green, and blue channel intensity, respectively, on a scale of 0–255.

### 3.3.5 Chemical Analysis

At the beginning and end of the continuous LBI measurement, the following chemical properties were measured (Table 3.1): ash content, phosphorus content, carbon residue, total contamination, water content, oxidation stability, vitamin E ( $\gamma$ -tocotrienol,  $\delta$ -tocopherol and  $\gamma$ -tocopherol), and acid value.

**Table 3.1 Measurement methods used for continuous LBI measurement.**

Oil Parameter	Unit	Method or Instrument
Ash content	% (m/m)	ISO 6884 [25]
Phosphorus content	mg/kg	DIN EN ISO 11885 <sup>1</sup> [26] DIN EN 14107 [27]
Carbon residue	% (m/m)	DIN EN ISO 10370 [28]
Total contamination	mg/kg	DIN EN 12662 [29]
Water content	% (m/m)	DIN 12937 [30]
Oxidation stability	h	DIN EN 14112 [31]
$\gamma$ -Tocotrienol	$\mu\text{g/g}$	Grebenstein and Frank, 2012 [32]
$\delta$ -Tocopherol	$\mu\text{g/g}$	Grebenstein and Frank, 2012 [32]
$\gamma$ -Tocopherol	$\mu\text{g/g}$	Grebenstein and Frank, 2012 [32]
Acid value	mg KOH/g	SI Analytics [33]

<sup>1</sup> Performed after microwave digestion due to the high presence of particles in the crude oil.

### 3.3.6 Statistical Analysis

The statistical analysis in this research was performed with OriginPro (Version 2020, OriginLab, Northampton, MA, USA). R squared ( $R^2$ ) was used as the indicator of goodness of fit. To smoothen the plot of sedimentation velocity vs. time, a moving average function was applied with the period parameter set to 8.

## 3.4 Results and Discussion

### 3.4.1 Discontinuous LBI Measurement

Figure 3.3 shows the backscattering images of oil samples from discontinuous LBI measurement. At Day 0, the crude oil displayed a typical backscattering pattern on the sample surface. Gradually, the laser images showed a linear shape with increasing length over time, indicating the path of the laser light (Tyndall effect). The intensity of the linear pattern decreased in the direction of light transmission. For the red laser, an additional scattering pattern was observed on the right side of the image due to excessive light reaching the bottom of the sample container. Notably, yellow hues were visible between the overexposed center and the surrounding scattering area for the red laser, and purple hues for the blue laser.

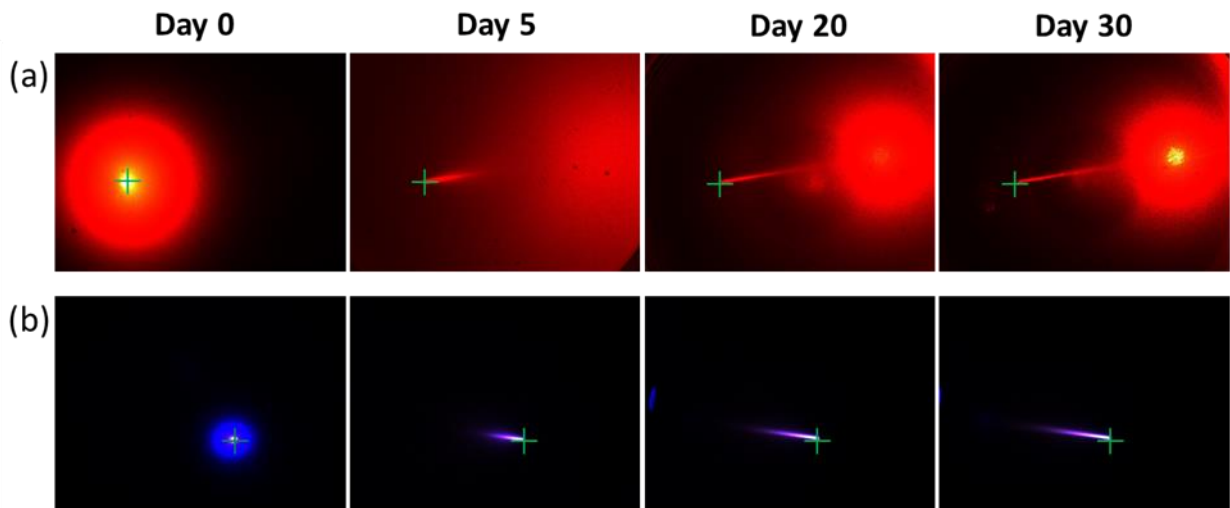


**Figure 3.3** Backscattering images of oil samples under (a) the 635 nm laser and (b) the 405 nm laser. The crosses in the images indicate the incident points where the laser light entered the surface of the oil. Note that the light from the 635 nm laser transmitted from left to right, reaching the bottom of the container as the oil became clearer. The 405 nm laser transmitted light from right to left.

At Day 0 of sedimentation, the round scattering spot can be attributed to the laser light interacting with particles that were still uniformly dispersed in the crude oil. Similar scattering spots were observed by other scientists when handling bio-materials [34–36] due to the porous nature of bio-materials. Wu et al. suggested that this scattering spot should be related to the particle size of the material [37]. As the oil became clearer, laser light could travel



deeper because there were fewer particles present to scatter and absorb the light, causing the scattering spot at the incident point to shrink. The Tyndall effect suggests that some particles remained within the oil even after sedimentation, which aligns with the research findings by Karaj and Müller [15]. They found that the sedimentation process predominantly impacts particles of substantial size. Huang et al. applied the Tyndall effect to detect  $\text{Hg}^{2+}$  in a colloidal solution and found that this method increased accuracy by 5400 times compared to the traditional approach [38].

### **3.4.2 Continuous LBI Measurement**

#### **3.4.2.1 Sesame Oil Sedimentation Dynamics**

During the sedimentation process of crude sesame oil, the oil and the sediment were divided, with an increasingly distinct interface (Figure 3.4). After 720 h of sedimentation, 493 mm of clear oil was obtained from the initial height of the crude oil layer of 592 mm. The change in interface height and sedimentation velocity over time are illustrated in Figure 3.5. The sedimentation velocity remained close to  $-7$  mm/h until about 25 h of the sedimentation. Afterwards, the velocity decreased to  $-2$  mm/h within about 15 h, then gradually dropped to a value close to 0. Linear and exponential regressions were performed to fit the curves within 0–39 h and 39–720 h, respectively. The timepoint 39 h was fitted as the turning point, since the  $R^2$  of the linear regression remained above 0.999 between 0 and 39 h and dropped below 0.999 after 40 h. Both regressions showed an  $R^2$  value close to 1.

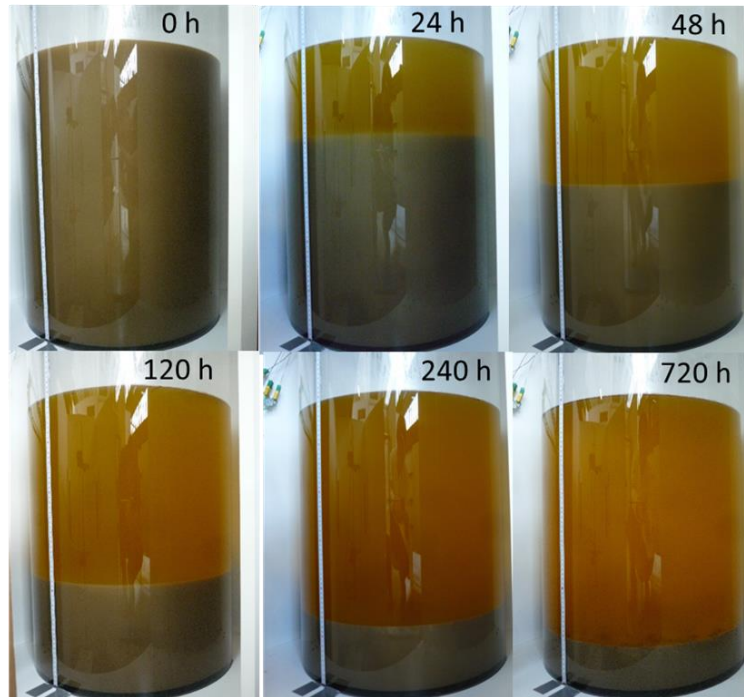


**Figure 3.4** Images of the entire tank during the sedimentation process.

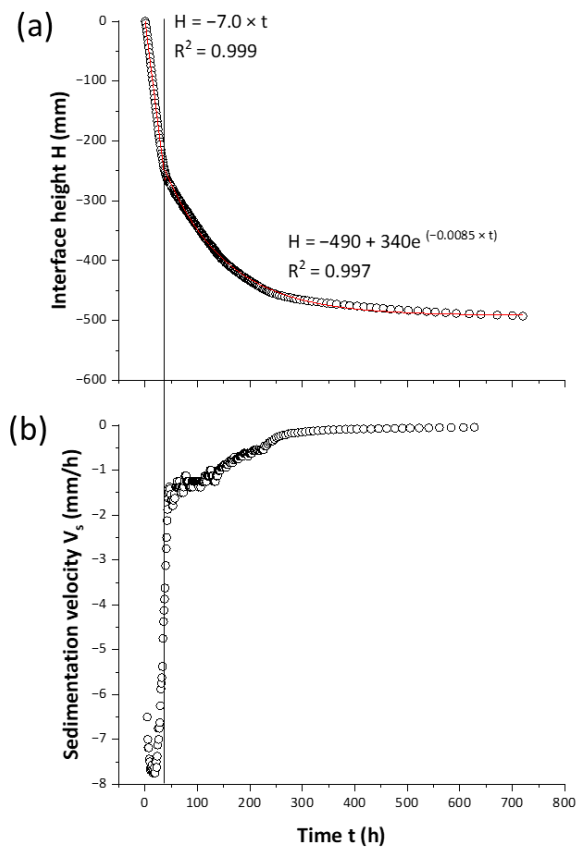


**Figure 3.5** Plot of the (a) interface height vs. time and (b) the sedimentation velocity vs. time.

At 24 h, the interface was still blurred. This is likely because, as sedimentation continued, particles within the sample mainly settled individually at varying speeds due to differences in particle size or shape within the crude oil, resulting in a slightly spatial difference for the particles and a blurred interface. As the particles approached each other, their settling patterns became increasingly influenced by their proximity, leading them to settle more collectively as a whole. This resulted in a clearer interface and a sedimentation velocity smaller than  $-2$  mm/h at 48 h. As the sedimentation process persisted, the particles were increasingly compacted, thereby causing a continual decrease in the sedimentation velocity. According to the features of different sedimentation stages, we could confirm that at least diluted sedimentation and hindered sedimentation exist for the sesame oil sedimentation process.

The sedimentation velocity of diluted sedimentation is not related to the sedimentation tank's cross-sectional area. Karaj and Müller also found that both horizontal and vertical sedimentation system had the same sedimentation speed at the beginning of their sedimentation process [15]. Further, it is interesting that oil sedimentation velocity is at a magnitude millimeter per hour, while for wastewater it is millimeter per minute [39]—this could be explained by the much higher viscosity of edible oil compared with water. In practice, when combining sedimentation with other oil refining techniques, the rapid sedimentation velocity changing period could be a possible option to switch from sedimentation to other techniques. Additionally, for unrefined sesame oil producers (who typically only filter the oil after pressing), due to the nature of diluted sedimentation, it is possible for them to predict and control the time when an obvious sediment could be seen by customers.

### **3.4.2.2 Backscattering Images**

In Figure 3.6a, the temporal changes in backscattering images are illustrated. At the initial timepoint (0 h), the backscattering was characterized by a large scattering area with an overexposed center. As time progressed to 1 h, the scattering area notably reduced but the central region became even brighter. Subsequently, both the central brightness and the scattering area diminished, and at time 720 h, the overexposed center was no longer present. Figure 3.6b shows an “L” shape, where the backscattering shows a sharp change followed by a gradual decrease over time. Notably, purplish hues were observed between the center and the surrounding scattering area, while in the discontinuous LBI measurement, it was yellow.

Wu et al. indicated that this was caused by the different sensitivities of the camera color channels [37]. Additionally, the discontinuous LBI measurement showed the Tyndall effect (Figure 3.3) but it was not observed in Figure 3.6. This could be due to the lid on top of the sedimentation tank, which caused a reduction in laser light intensity when reaching the oil.

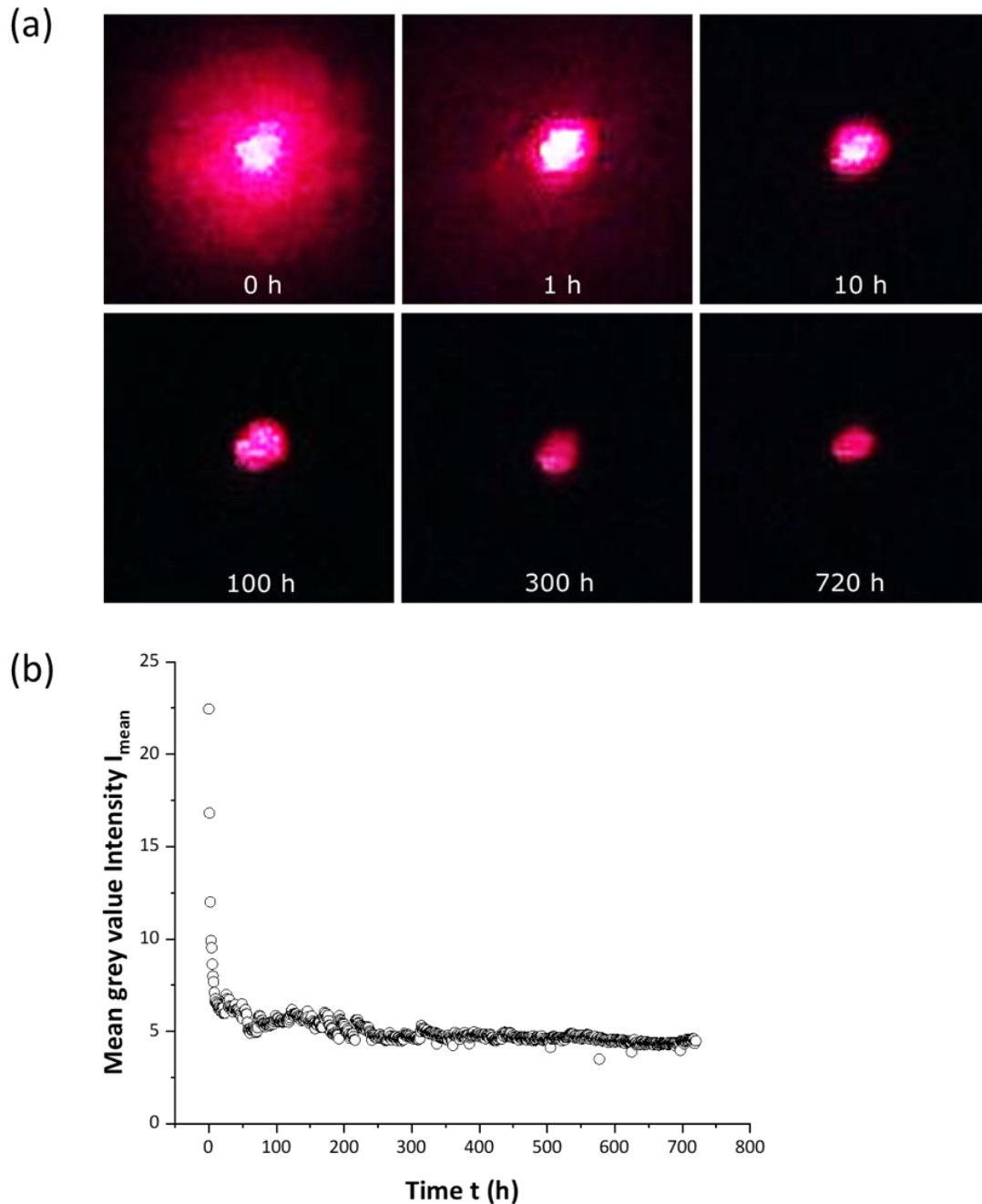


**Figure 3.6** (a) Backscattering images during sedimentation in in situ experiment. (b) Plot of mean grey value of the segmented image vs. time.

### 3.4.2.3 Correlation between Backscattering Images and Oil Interface Height

Figure 3.7 illustrates the correlation between the height of the oil–sediment interface and the backscattering images. The scattering phenomenon decreased as the interface moved to a lower position, particularly when the interface height ranged between 0 and –100 mm. When the interface was lower, e.g., at –450 mm, a laser signal fluctuation could be observed. An exponential curve was initially used to fit this correlation, resulting in an  $R^2$  value of 0.73 (Figure 3.7a). As the sedimentation process progressed, the influence on the scattering spot located on the oil surface diminished, thereby increasing the difficulty of predicting the interface height based on the scattering spot. However, fitting the data with interface heights only between 0 and –100 mm using a power function resulted in an  $R^2$  of 0.97 (Figure 3.7b). This indicates that the scattering spots at the oil surface were more suitable for measuring the sedimentation process in the early stage of the diluted sedimentation. The Tyndall effect (Figure 3.3) may be more suitable for monitoring the entire sedimentation process. The laser’s traveling depth should be crucial for observation, indicating that decreasing the height of the sedimentation tank may not only speed up the sedimentation process [15] but also make laser scattering technology more suitable for monitoring the sedimentation process.

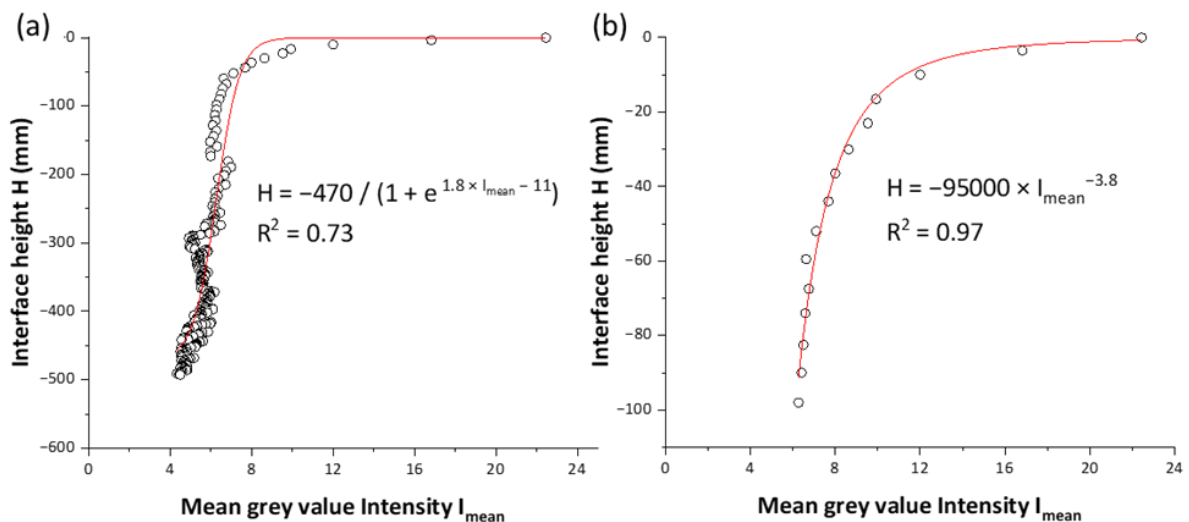


**Figure 3.7** (a) Regression between interface height and mean grey value intensity  $I_{mean}$  of segmented images. (b) Regression when the interface height is less than 100 mm.

### 3.4.2.4 Chemical Properties

Table 3.2 presents the results of the comparison between the chemical properties before (Day 0) and after sedimentation (Day 30). Most of the parameters studied showed significant differences before and after sedimentation, with the exception of  $\delta$ -tocopherol and  $\gamma$ -tocopherol. Among all the changes in chemical properties, the ash content was not detectable after sedimentation. The total contamination decreased by 99.9% and the phosphorus content decreased by 99.5%, followed by water content (90%) and carbon residue (87%). The chemical properties that were strongly associated with the oil oxidation process—i.e., oxidation stability, vitamin E, and acid value—changed to a lesser degree. For pressed sesame oil, Mohammed et al. reported a phosphorus content of 1.14–3.94 mg/kg [40]; Melo et al. found an oxidation stability of 5.8 h and  $\gamma$ -tocopherol of 456  $\mu\text{g/g}$  [41]; Kheirati Rounizi et al. recorded an acid value of 3.68 mg/kg [42]. Differences between these values and those in our study may be attributed to variations in sesame seed quality or variety, extraction conditions, or storage methods.

**Table 3.2 Chemical values of sesame oil measured before (Day 0) and after sedimentation (Day 30).**

Parameter	Day 0	Day 30
Ash content (% m/m)	0.84 <sup>a</sup> $\pm$ 0.02	0.00 <sup>b</sup> $\pm$ 0.00
Phosphorus content (mg/kg)	921 <sup>a</sup> $\pm$ 13	4.8 <sup>b</sup> $\pm$ 0.0
Carbon residue (% m/m)	2.68 <sup>a</sup> $\pm$ 0.04	0.34 <sup>b</sup> $\pm$ 0.00
Total contamination (mg/kg)	48,170 <sup>a</sup> $\pm$ 1836	71 <sup>b</sup> $\pm$ 9
Water content (% m/m)	0.86 <sup>a</sup> $\pm$ 0.02	0.09 <sup>b</sup> $\pm$ 0.00
Oxidation stability (h)	19.8 <sup>a</sup> $\pm$ 0.2	9.6 <sup>b</sup> $\pm$ 0.1
$\gamma$ -Tocotrienol ( $\mu\text{g/g}$ )	1.106 <sup>a</sup> $\pm$ 0.108	0.858 <sup>b</sup> $\pm$ 0.088
$\delta$ -Tocopherol ( $\mu\text{g/g}$ )	5.200 <sup>a</sup> $\pm$ 0.512	4.717 <sup>a</sup> $\pm$ 0.272
$\gamma$ -Tocopherol ( $\mu\text{g/g}$ )	333.32 <sup>a</sup> $\pm$ 26.07	314.80 <sup>a</sup> $\pm$ 12.59
Acid value (mg KOH/g)	0.98 <sup>a</sup> $\pm$ 0.02	1.82 <sup>b</sup> $\pm$ 0.03

Note: Values are means of replications  $\pm$  standard deviation. Values in the same row with the same letter are not significantly different at  $p < 0.05$ .

Among all the measured chemical properties, ash content, phosphorus content, total contamination, and carbon residue should be mostly related to the particles present inside the crude oil. The settling of the particles caused more than an 86% drop in these values in the sesame oil. As for the 90% decrease in water content, Karaj and Müller related it to high-temperature evaporation [15]. Since the sesame oil was within  $21 \pm 3$  °C, it is more likely that the decrease in water content was also influenced by the consumption of H<sub>2</sub>O in the oil hydrolysis process. The decrease in oxidation stability and the increase in acid value are typical changes that occur during oil oxidation. However, the values of the two types of vitamin E ( $\delta$ -tocopherol,  $\gamma$ -tocopherol) did not change significantly during the oxidation process. This could be because sesame oil contains additional antioxidants such as sesamin, sesamol, and sesamolol, which protected vitamin E from decomposition [6]. After sedimentation, the measured chemical values did not meet the requirements of combustion engines (total contamination upper limitation, 24 mg/kg) [43] but were suitable for food (acid value) [44] and pressure stoves (acid value and total contamination) [14,45].

### 3.5 Conclusions

In the application of LBI to the sedimentation process of sesame oil, two types of scattering effects were observed. The first was a typical scattering spot at the oil's surface, and the second was a Tyndall effect with an increasingly extended path as the sedimentation process continued. The scattering spot at the surface of the oil should be more suitable for monitoring the early stage of diluted sedimentation while the Tyndall effect should be better suited for monitoring the entire process. The crude sesame oil sedimentation process consists of at least two stages: diluted sedimentation and hindered sedimentation. In this study, the sedimentation speed was about  $-7$  mm/h during the diluted sedimentation stage and then dropped to less than  $-2$  mm/h, indicating the transition into the hindered sedimentation stage. During the sedimentation process, three factors influenced the oil properties: settling of the particles, oxidation, and hydrolysis. The low change in vitamin E content may be due to the antioxidants of the sesame oil.

It is implied that when the volume of a sedimentation tank is fixed, increasing the cross section and decreasing the height can speed up the sedimentation process and benefit the application

of low-cost laser backscattering technology. For producers who make unrefined sesame oil, confirming the diluted sedimentation stage can help them control the time when the customer will see the sedimentation. The laser's power was 1 mW in the continuous LBI measurement. Further research could use a higher power laser source to enhance both the scattering on the oil surface and the Tyndall effects inside the oil. Additionally, experiments with more plant oil varieties could be conducted to extend the applicability of the LBI technology. It is worth noting that the sedimentation tank design method was greatly improved in the field of wastewater treatment. People interested in plant oil sedimentation may benefit from the similarity between these two processes.

### Conflicts of Interest

The authors declare no conflict of interest.

### Acknowledgments

Special thanks to Tsubasa Mitsui, Ute Waldeck, Olga Gotra, Sarah Fleischmann, and Nadine Grebenstein for their assistance in conducting the experiment.

## 3.6 References

1. FAO, Food and Agriculture Organization of the United Nations. Available online: <https://www.fao.org/faostat/en/#data/QCL> (accessed on 6 March 2023).
2. Rezaei, M.; Ramezani, M. Physicochemical Properties of Heavy Metals and Aflatoxin Levels in Sesame Oil: A Review Study. *J. Nutr. Fasting Health* 2018, 6, 45–51. <https://doi.org/10.22038/jnfh.2018.33801.1128>.
3. Sallam, K.I.; Abd-Elghany, S.M.; Imre, K.; Morar, A.; Herman, V.; Hussein, M.A.; Mahros, M.A. Ensuring Safety and Improving Keeping Quality of Meatballs by Addition of Sesame Oil and Sesamol as Natural Antimicrobial and Antioxidant Agents. *Food Microbiol.* 2021, 99, 103834. <https://doi.org/10.1016/j.fm.2021.103834>.
4. Alshahrani, S.; Al Sreaya, A.A.; Mashyakhi, M.Y.; Alqahtani, S.; Sivakumar, S.M.; Alhazmi, H.A.; Rehman, Z.; Alam, F. Chemical Characterization and Antibacterial Efficacy of Saudi Sesame Oil against Human Pathogenic Bacteria. *Environ. Conserv. J.* 2020, 21, 19–29. <https://doi.org/10.36953/ecj.2020.211203>.



5. Langyan, S.; Yadava, P.; Sharma, S.; Gupta, N.C.; Bansal, R.; Yadav, R.; Kalia, S.; Kumar, A. Food and Nutraceutical Functions of Sesame Oil: An Underutilized Crop for Nutritional and Health Benefits. *Food Chem.* 2022, 389, 132990. <https://doi.org/10.1016/j.foodchem.2022.132990>.
6. Mujtaba, M.A.; Muk Cho, H.; Masjuki, H.H.; Kalam, M.A.; Ong, H.C.; Gul, M.; Harith, M.H.; Yusoff, M.N.A.M. Critical Review on Sesame Seed Oil and Its Methyl Ester on Cold Flow and Oxidation Stability. *Energy Reports* 2020, 6, 40–54. <https://doi.org/10.1016/j.egy.2019.11.160>.
7. Soltani, H.; Karimi, A.; Falahatpisheh, S. The Optimization of Biodiesel Production from Transesterification of Sesame Oil via Applying Ultrasound-Assisted Techniques: Comparison of RSM and ANN-PSO Hybrid Model. *Chem. Prod. Process Model.* 2022, 17, 55–67. <https://doi.org/10.1515/cppm-2020-0076>.
8. Mahloujifar, M.; Mansournia, M. A Comparative Study on the Catalytic Performances of Alkali Metals-Loaded KAlSiO<sub>4</sub> for Biodiesel Production from Sesame Oil. *Fuel* 2021, 291, 120145. <https://doi.org/10.1016/j.fuel.2021.120145>.
9. Ahmad, R. Gravity Separation/Sedimentation. In *Water Encyclopedia*; Wiley: Hoboken, NJ, USA, 2005; pp. 259–261; ISBN 9780471478447.
10. Vaisali, C.; Charanyaa, S.; Belur, P.D.; Regupathi, I. Refining of Edible Oils: A Critical Appraisal of Current and Potential Technologies. *Int. J. Food Sci. Technol.* 2015, 50, 13–23. <https://doi.org/10.1111/ijfs.12657>.
11. Santori, G.; Di Nicola, G.; Moglie, M.; Polonara, F. A Review Analyzing the Industrial Biodiesel Production Practice Starting from Vegetable Oil Refining. *Appl. Energy* 2012, 92, 109–132. <https://doi.org/10.1016/j.apenergy.2011.10.031>.
12. Gupta, M.K. Refining. In *Practical Guide to Vegetable Oil Processing*; Elsevier: Amsterdam, The Netherlands, 2017; pp. 79–128; ISBN 9781630670504.
13. Altieri, G.; Di Renzo, G.C.; Genovese, F.; Tauriello, A.; D'Auria, M.; Racioppi, R.; Viggiani, L. Olive Oil Quality Improvement Using a Natural Sedimentation Plant at Industrial Scale. *Biosyst. Eng.* 2014, 122, 99–114. <https://doi.org/10.1016/j.biosystemseng.2014.04.007>.
14. Karaj, S.; Müller, J. Influence of Total Contamination of Jatropha Curcas Oil on Deposits and Performance of Plant Oil Pressure Stoves. In Proceedings of the European Biomass Conference and Exhibition Proceedings, Milan, Italy, 18–22 June 2012; pp. 1311–1315.
15. Karaj, S.; Müller, J. Effect of Container Depth and Sedimentation Time on Quality of Jatropha Curcas L. Oil. *Fuel* 2014, 118, 206–213. <https://doi.org/10.1016/j.fuel.2013.10.066>.

16. Davis, J.P.; Geller, D.; Faircloth, W.H.; Sanders, T.H. Comparisons of Biodiesel Produced from Unrefined Oils of Different Peanut Cultivars. *JAOCS, J. Am. Oil Chem. Soc.* 2009, *86*, 353–361. <https://doi.org/10.1007/s11746-009-1353-z>.
17. Hrom, K.; Devi, T.T. Application of Computational Fluid Dynamics in Sedimentation Tank Design and Its Recent Developments: A Review. *Water, Air, Soil Pollut.* 2022, *233*, 22. <https://doi.org/10.1007/s11270-021-05458-9>.
18. Oleador GmbH. Available online: <https://www.oleador.com/en/contact/faq-detail-Oils,deposit-66.html> (accessed on 10 March 2023).
19. Rushton, A.; Ward, A.S.; Holdich, R.G. Sedimentation Fundamentals. In *Solid-Liquid Filtration and Separation Technology*; Wiley-VCH: Weinheim, Germany, 1996.
20. Pietsch, T.; Mehrwald, R.; Grajetzki, R.; Sens, J.; Märkl, H. Sedimentation Behaviour of Sludge Particles in a Biogas Tower Reactor and the Function of a Hydrostatically Pressurized Sedimenter. *Water Res.* 2003, *37*, 1071–1079. [https://doi.org/10.1016/S0043-1354\(01\)00512-7](https://doi.org/10.1016/S0043-1354(01)00512-7).
21. Mollazade, K.; Omid, M.; Tab, F.A.; Mohtasebi, S.S. Principles and Applications of Light Backscattering Imaging in Quality Evaluation of Agro-Food Products: A Review. *Food Bioprocess Technol.* 2012, *5*, 1465–1485. <https://doi.org/10.1007/s11947-012-0821-x>.
22. Lu, B.; Dao, P.D.; Liu, J.; He, Y.; Shang, J. Recent Advances of Hyperspectral Imaging Technology and Applications in Agriculture. *Remote Sens.* 2020, *12*, 2659. <https://doi.org/10.3390/RS12162659>.
23. Sanchez, P.D.C.; Hashim, N.; Shamsudin, R.; Mohd Nor, M.Z. Potential Application of Laser-Based Imaging Technology in the Quality Evaluation of Agricultural Products: A Review. *Adv. Agric. Food Res. J.* 2020, *1*, 243–256. <https://doi.org/10.36877/aafjr.a0000127>.
24. Kiliçkan, A.; Üçer, N.; Yalçın, I. Moisture-Dependent Physical Properties of Grape (*Vitis Vinifera* L.) Seed. *Sci. Res. Essays* 2010, *5*, 2226–2233.
25. *ISO 6884*; Animal and Vegetable Fats and Oils—Determination of Ash; ISO: Geneva, Switzerland, 1985.
26. *DIN EN ISO 11885*; Water Quality—Determination of Selected Elements by Inductively Coupled Plasma Optical Emission Spectrometry (ICP-OES) (ISO 11885:2007); Beuth: Berlin, Germany, 2009. <https://dx.doi.org/10.31030/1530145>.
27. *DIN EN 14107*; Fat and Oil Derivatives—Fatty Acid Methyl esters (FAME)—Determination of Phosphorus Content by Inductively Coupled Plasma (ICP) Emission Spectrometry; Beuth: Berlin, Germany, 2003. <https://dx.doi.org/10.31030/9393419>

28. *DIN EN ISO 10370*; Petroleum Products—Determination of Carbon Residue—Micro Method (ISO 10370:1993); Beuth: Berlin, Germany, 1995.
29. *DIN EN 12662*; Liquid Petroleum Products—Determination of Contamination in Middle Distillates; Beuth: Berlin, Germany, 2008.
30. *DIN EN ISO 12937*; Petroleum Products—Determination of Water—Coulometric Karl Fischer Titration Method (ISO 12937:2000) ; Beuth: Berlin, Germany, 2002. <https://dx.doi.org/10.31030/9131845>.
31. *DIN EN 14112*; Fat and Oil Derivatives—Fatty Acid Methyl Esters (FAME)—Determination of Oxidation Stability (Accelerated Oxidation Test); Beuth: Berlin, Germany, 2016. <https://dx.doi.org/10.31030/2427347>
32. Grebenstein, N.; Frank, J. Rapid Baseline-Separation of All Eight Tocopherols and Tocotrienols by Reversed-Phase Liquid-Chromatography with a Solid-Core Pentafluorophenyl Column and Their Sensitive Quantification in Plasma and Liver. *J. Chromatogr. A* 2012, *1243*, 39–46. <https://doi.org/10.1016/j.chroma.2012.04.042>.
33. SI Analytics. Determination of Acid Number and Free Fatty Acids (FFA) in Fats and Oils. (DGF-Einheitsmethoden C-V 2) Available online: [https://uk.vwr.com/m-uk.vwr.com/en\\_GB/images/Acidity-in-fats-and-oils-FFA\\_285KB\\_English-PDF.pdf](https://uk.vwr.com/m-uk.vwr.com/en_GB/images/Acidity-in-fats-and-oils-FFA_285KB_English-PDF.pdf) (accessed on 6 April 2023).
34. Lorente, D.; Zude, M.; Idler, C.; Gómez-Sanchis, J.; Blasco, J. Laser-Light Backscattering Imaging for Early Decay Detection in Citrus Fruit Using Both a Statistical and a Physical Model. *J. Food Eng.* 2015, *154*, 76–85. <https://doi.org/10.1016/j.jfoodeng.2015.01.004>.
35. Adebayo, S.E.; Hashim, N.; Abdan, K.; Hanafi, M. Application and Potential of Backscattering Imaging Techniques in Agricultural and Food Processing—A Review. *J. Food Eng.* 2016, *169*, 155–164. <https://doi.org/10.1016/J.JFOODENG.2015.08.006>.
36. Sanchez, P.D.C.; Hashim, N.; Shamsudin, R.; Mohd Nor, M.Z. Quality Evaluation of Sweet Potatoes (*Ipomoea Batatas* L.) of Different Varieties Using Laser Light Backscattering Imaging Technique. *Sci. Hortic.* 2020, *260*, 108861. <https://doi.org/10.1016/j.scienta.2019.108861>.
37. Wu, Z.; Spohrer, K.; Nagle, M.; Müller, J. Investigating the Influence of Pore Size, Pore Fluid and Wavelength on Backscattering Images with Sintered Glass Filter Matrices as Experimental Models. *Postharvest Biol. Technol.* 2023, *200*, 112329. <https://doi.org/10.1016/j.postharvbio.2023.112329>.
38. Huang, J.; Mo, X.; Fu, H.; Sun, Y.; Gao, Q.; Chen, X.; Zou, J.; Yuan, Y.; Nie, J.; Zhang, Y. Tyndall-Effect-Enhanced Supersensitive Naked-Eye Determination of Mercury (II) Ions with Silver Nanoparticles. *Sensors Actuators, B Chem.* 2021, *344*, 130218.

<https://doi.org/10.1016/j.snb.2021.130218>.

39. Song, Z.; Williams, C.J.; Edyvean, R.G.J. Sedimentation of Tannery Wastewater. *Water Res.* 2000, *34*, 2171–2176. [https://doi.org/10.1016/S0043-1354\(99\)00358-9](https://doi.org/10.1016/S0043-1354(99)00358-9).

40. Mohammed, F.; Abdulwali, N.; Guillaume, D.; Tenyang, N.; Ponka, R.; Al-Gadabi, K.; Bchitou, R.; Abdullah, A.H.; Naji, K.M. Chemical Composition and Mineralogical Residence of Sesame Oil from Plants Grown in Different Yemeni Environments. *Microchem. J.* 2018, *140*, 269–277. <https://doi.org/10.1016/j.microc.2018.04.011>.

41. Melo, D.; Álvarez-ortí, M.; Nunes, M.A.; Costa, A.S.G.; Machado, S.; Alves, R.C.; Pardo, J.E.; Oliveira, M.B.P.P. Whole or Defatted Sesame Seeds (*Sesamum Indicum* L.)? The Effect of Cold Pressing on Oil and Cake Quality. *Foods* 2021, *10*, 2108. <https://doi.org/10.3390/foods10092108>.

42. Kheirati Rounizi, S.; Akrami Mohajeri, F.; Moshtaghi Broujeni, H.; Pourramezani, F.; Jambarsang, S.; Kiani, H.; Khalili Sadrabad, E. The Chemical Composition and Heavy Metal Content of Sesame Oil Produced by Different Methods: A Risk Assessment Study. *Food Sci. Nutr.* 2021, *9*, 2886–2893. <https://doi.org/10.1002/fsn3.2245>.

43. *DIN 51623*; Fuels for Vegetable Oil Compatible Combustion Engines—Fuel from Vegetable Oil—Requirements and Test Methods; Beuth: Berlin, Germany, 2020. <https://dx.doi.org/10.31030/3178561>.

44. CXS 210-1999—Standard for Named Vegetable Oils; FAO: Rome, Italy, 2022. Available online: <https://www.fao.org/fao-who-codexalimentarius/codex-texts/list-standards/en/> (accessed on 6 March 2023).

45. Kratzeisen, M.; Müller, J. Influence of Free Fatty Acid Content of Coconut Oil on Deposit and Performance of Plant Oil Pressure Stoves. *Fuel* 2010, *89*, 1583–1589. <https://doi.org/10.1016/j.fuel.2009.08.038>.

# 4

## **A novel method for leaf wetness measurement with laser-induced light reflection and RGB imaging**

Zhangkai Wu <sup>a</sup>, Zhichong Wang <sup>a</sup>, Klaus Spohrer <sup>a</sup>,  
Steffen Schock <sup>a</sup>, Xiongkui He <sup>b,c</sup>, Joachim Müller<sup>a</sup>

<sup>a</sup> University of Hohenheim, Institute of Agricultural Engineering,  
Tropics and Subtropics Group, Stuttgart, 70599, Germany

<sup>b</sup> China Agricultural University, College of Science, Beijing, 100193, China;

<sup>c</sup> China Agricultural University, College of Agricultural Unmanned System,  
Beijing, 100193, China.

*Submitted to Biosystems Engineering, October 2023*

## 4.1 Abstract

Leaf wetness duration is a crucial factor in plant disease management. Current optical methods classify leaf wetness as a binary problem, i.e., wet or dry. In this study, an experimental platform was built to semi-automatically measure droplet deposition on grape leaves while capturing red laser images using an RGB camera. Water mass per leaf area was used to represent leaf wetness value. A generalized additive model (GAM) was employed to predict the leaf wetness value with extracted features (image leaf area, mean red channel intensity and identified number of droplets) from the laser images. The R-squared ( $R^2$ ) value for the prediction of the test dataset was 0.78. Image resolution and leaf orientation were identified as factors that influenced the model accuracy. The measurement method presented in this study has the potential to quantify leaf wetness accurately.

## 4.2 Introduction

Duration of free water on leaf surfaces, also known as leaf wetness duration, plays a crucial role in many plant diseases (Chungu et al., 2001; Huber and Gillespie, 1992; Neufeld and Ojiambo, 2012). Leaf wetness can change frequently due to events such as dew formation, rainfall, and sprinkler irrigation. Therefore, real-time leaf wetness information is essential for predicting and managing diseases.

The most common tool for measuring leaf wetness is the leaf wetness sensor (LWS). The LWS is an electronic circuit that mimics a leaf in its natural environment and collects electronic properties influenced by water. Many researchers have attempted to improve the performance and feasibility of LWS by, for example, painting it (Sentelhas et al., 2004b), adjusting installation parameters (Sentelhas et al., 2004a), or reducing its cost with compact designs, flexible substrates, or passive radio-frequency identification (Hornero et al., 2017; Patle et al., 2021; Dey et al., 2020). However, due to the complexity and cost of using LWS, some scientist also tried to bypass LWS measurement with either an empirical model (Sentelhas et al., 2008; Wang et al., 2020), physical model (Shin et al., 2021), or a hybrid model (Gama et al., 2022).

Besides LWS and models, more leaf wetness measurement methods should be developed since they provide true value for model building (Liu et al., 2022; Park et al., 2019; Shin et al., 2021), have the potential to be refined due to the rising of optical methods (Osroosh & Peters, 2019; Ranjan et al., 2022), and can help in various applications, such as estimating spray deposition (Foqué et al., 2018) and monitoring leaf litter interception of water (Acharya et al., 2017).

Specifically, scientists have attempted to measure leaf wetness with imaging techniques for a long time (Duvdevani, 1947). Human observation is viewed as the most accurate way to estimate leaf wetness rather than using an artificial leaf to measure leaf wetness indirectly (Rowlandson et al., 2014). This suggests the potential advantage of optical methods. Researchers such as Patel et al. (2021), Wen et al. (2020) and Swarup et al. (2020) have used RGB and thermal camera to detect leaf wetness and fruit surface wetness, and Wen et al. (2020) attempted to use a thermal camera to obtain leaf wetness of cucumber in a solar greenhouse. These studies based on optical methods took leaf wetness measurement as a classification problem, i.e., whether the leaf was dry or wet. This is sufficient for calculating leaf wetness duration. However, quantifying leaf wetness could further develop the potential of optical methods, help optimization of classification and expand their application.

Since leaves would absorb red light, meanwhile water would reflect red light, the object of this study is to evaluate the potential for quantifying leaf wetness using red laser imaging. Specifically, the mass of water droplets per leaf area was used as a standard value, with an attempt to measure it using RGB images and a red laser as a light source.

## **4.3 Materials and methods**

### **4.3.1 Experiment platform set-up**

To obtain accurate leaf wetness values and capture images simultaneously, an experimental platform was constructed as shown in Figure 4.1. The platform was designed to support a leaf with three Teflon rods, which were placed on a balance with a precision of 0.1 mg (WKR204C-S, Mettler Toledo, Greifensee, Switzerland). Teflon was chosen as the material to minimize the adherence of water drops. The balance was shielded from water spray using a lid. For each

measurement, one grape leaf (c.v. Pinot Meunier, vineyard University of Hohenheim, Germany) was placed on the Teflon rods. Two red lasers with opening angle of  $50^\circ$  and a laser dot of  $<400$  mm at 0.3 m (EJ658-10-3 (14x26)-AWL, Picotronic, Koblenz, Germany) were positioned above the container to illuminate the entire leaf. The red lasers were used to minimize the light reflected by the green leaf and emphasize the light reflected by water droplets. The horizontal distance between the two lasers was 20 cm, and the vertical distance between the lasers and leaf was 31 cm. The angle between the laser axis and perpendicular direction was 12 degrees. An RGB camera (puA2500-14uc, Basler, Ahrensburg, Germany) was placed 27 cm above the leaf to capture images. The size of the captured images was 2592 x 1944 pixels, with a resolution of 0.1 mm/pixel. A sprayer (332000, Lux, Wermelskirchen, Germany) was used to spray water droplets onto the leaf surface. The nozzle diameter was 1.3 mm, and a 2 kg weight was placed on the piston of the sprayer to maintain a stable pressure.

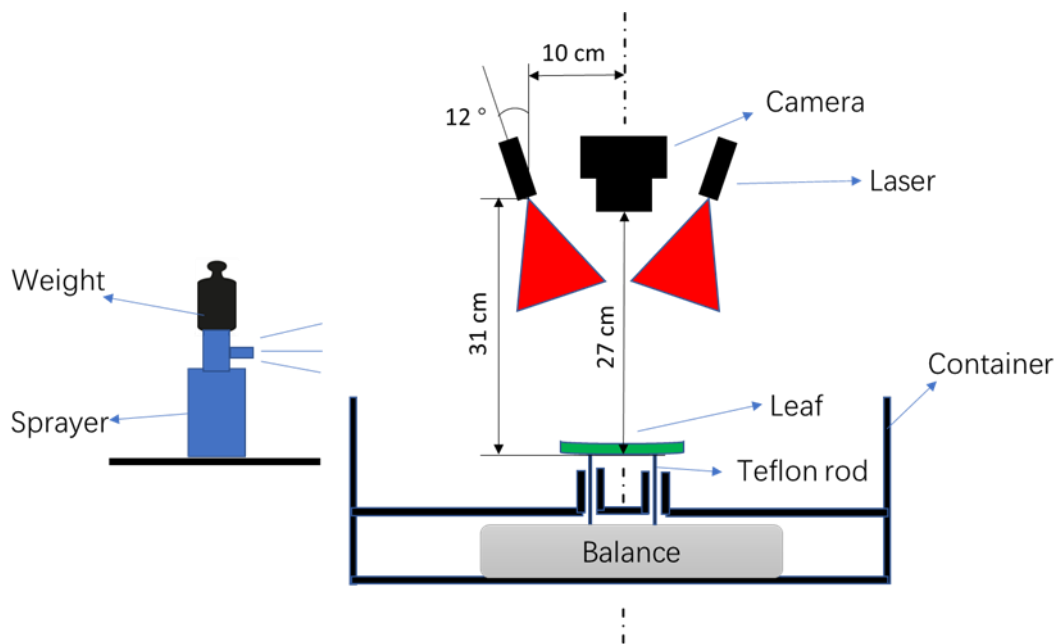


**Figure 4.1** Experimental setup with a balance supporting a leaf, a sprayer used to apply water droplets on the leaf surface and an optical device to measure its wetness.

### 4.3.2 Experimental procedure

Laser lights were turned on for at least 15 minutes before starting the measurements to ensure stability. The experiment procedure is shown in Figure 4.2. Throughout the experiment, the balance continuously recorded mass data with corresponding time stamps (Figure 4.4). After



each spraying, the mass and image information of the leaf were recorded simultaneously. The leaf was sprayed six times in total. The water mass per leaf area and image features were then utilized to construct the prediction model. In total 100 leaves were used in this research.

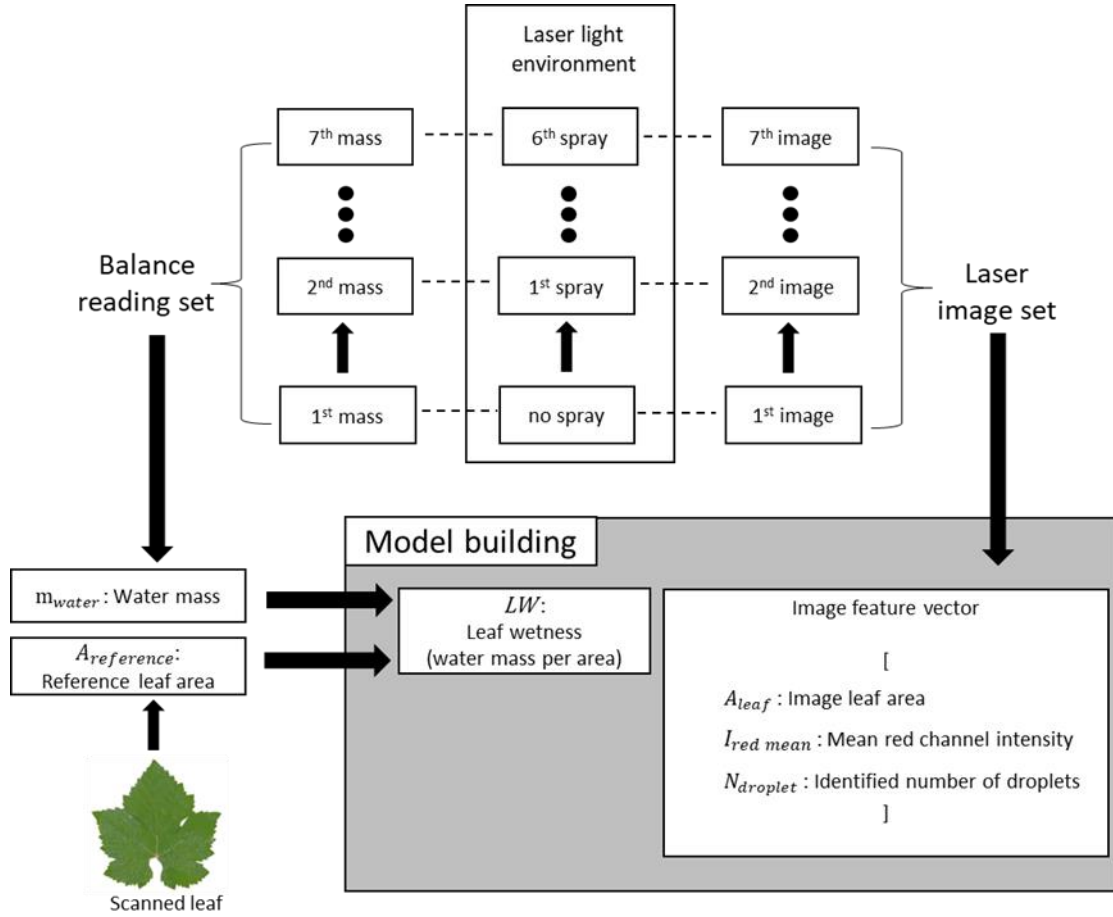


Figure 4.2 Experiment procedure.

### 4.3.3 Deposition measurement

The mass of water that was deposited on the leaf was measured by the balance. As a reference for the camera measurements, the leaf area was determined after the measurement by cutting each leaf into smaller pieces to compensate for curvatures, scanning the pieces with a scanner (bizhub 454e, Konica Minolta, Tokyo, Japan), and then segmenting them from the scanned images. Pixels occupied by the leaf were used to calculate the leaf area as:

$$A_{reference} = \frac{Leaf\ pixels}{dpi^2} \times 2.54^2 \quad (4-1)$$

where  $A_{reference}$  is the leaf area determined by the scanner in  $cm^2$ , and dpi equals to 300 dot

per inch in this research. Finally, the leaf wetness value was calculated as:

$$LW = \frac{m_{water}}{A_{reference}} \quad (4-2)$$

where  $LW$  is the leaf wetness in  $\text{mg}/\text{cm}^2$ ,  $m_{water}$  is the mass of deposited water in  $\text{mg}$ .

To measure the droplet size distribution, red ink was added to water and sprayed onto white paper under the same pressure and direction as before (Wang et al., 2021). The paper with ink was scanned at 600 dots per inch. The scanned images were processed and measured with ImageJ (Schneider et al., 2012) and the USDA-ARS plugin to obtain the distribution (Zhu et al., 2011).

#### 4.3.4 Image analysis and features extraction

The process of image analysis and features extraction was carried out using Matlab (R2021b, MathWorks, Massachusetts, USA). To separate the leaves in the laser images from the background, the red channel of images was processed in several steps. First, the images were subjected to median filtering twice using a 3 x 3 window. Image binarization was then performed using the threshold determined by the Otsu method (Otsu, 1979). This binarized image was labeled as  $I_0$ . Connected pixels smaller than 50000 pixels were set to 0 (background). The image was then dilated with a disk-shaped element of radius 10 pixels. Afterwards, the image was subjected to hole filling, followed by erosion with a disk-shaped element of 20 pixels. The original holes in the image were recovered using the dot product with  $I_0$ . After these processes, a segmentation matrix  $I_s$  was obtained for each laser image, which was used to separate the leaf from the background.

Following segmentation, the image leaf area ( $A_{leaf}$ ) and mean intensity per pixel in the red channel ( $I_{red\ mean}$ ) could be directly calculated. The droplet amount ( $N_{droplet}$ ) and positions were obtained from the green channel by applying a median filter with a 3 x 3 window, followed by a threshold value 28.5. Areas that were connected by at least 2 pixels horizontally or vertically were identified as a droplet and positioned accordingly.

Although no green light was used in this study, the green channel could be used to obtain  $N_{droplet}$  for the following reason: the red light could pass the green filter of the camera due to

its intensity and thus artifactually captured as green light. However, this also means that the detected green light can be attributed to very intense red light (Wu et al., 2023). This provides the possibility to use information from different color channels in a red laser experiment to improve data analysis (Verdú et al., 2021).

### **4.3.5 Model building**

A generalized additive model (GAM) based on gradient boosting decision tree was used to build a regression between the image features and leaf wetness with Matlab (R2021b, MathWorks, Massachusetts, USA). The default settings in Matlab were used when building the GAM model. The 100 leaves were randomly divided into two sets, with 70% used for calibration and 30% for validation. To avoid bias from the dataset division, the dataset division and model building process were run 1000 times. Then, the average value and standard error of  $R^2$ , root mean square error (RMSE), relative root mean square error (rRMSE) were reported (Despotovic et al., 2016).

## **4.4 Results and discussion**

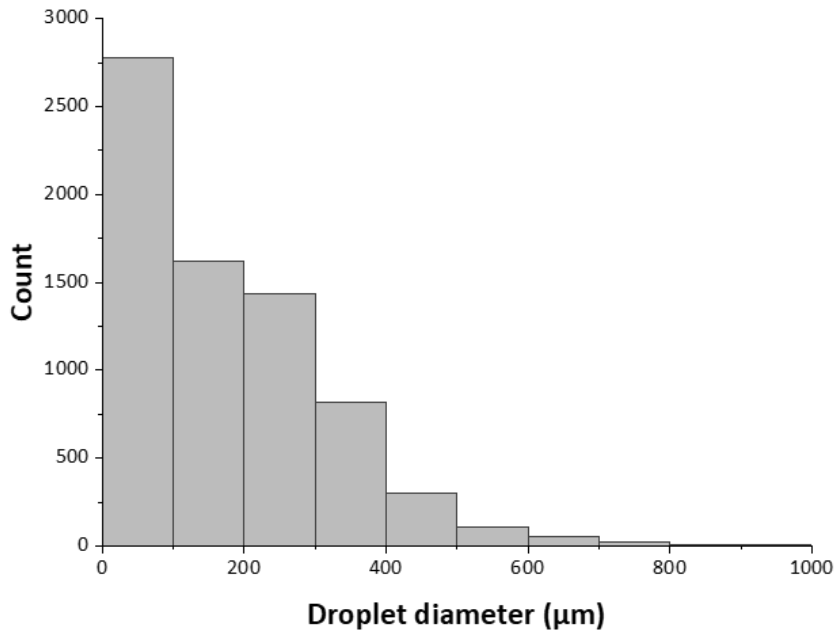
### **4.4.1 Droplet size distribution**

The distribution of the diameter of the droplets deposited on paper after the 1<sup>st</sup> spray is shown in Figure 4.3, with the largest number of droplets (>2750) recorded in the 0 –100  $\mu\text{m}$  class. The number of droplets in each size class decreased sharply as the droplet diameter increased, with only approximately 300 droplets found in the 400-500  $\mu\text{m}$  class. Therefore, the majority of droplets (> 92%) had a diameter of less than 400  $\mu\text{m}$  and few droplets (0.3%) had a diameter greater than 800  $\mu\text{m}$ .

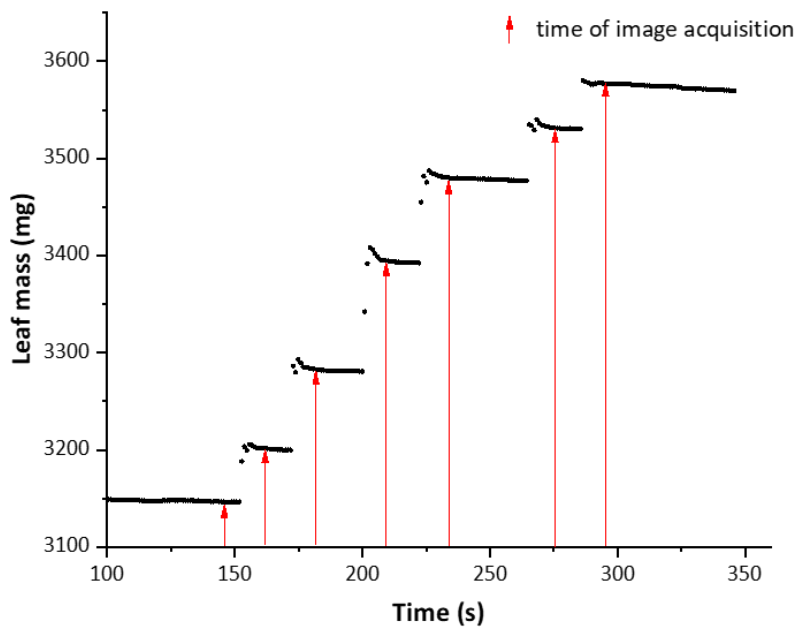
### **4.4.2 Water deposition on the leaves**

Figure 4.4 shows the stepwise increase in leaf mass with each spray. The initial mass of the leaf before spraying was 3150 mg, and it increased to over 3550 mg after 6 sprays. After each spray, the measured mass decreased first quickly and then slowly which can be explained by evaporation. To ensure consistent image acquisitions, the readings were always taken after

the initial rapid mass decrease. The corresponding image acquisition times are indicated with red arrows in Figure 4.4.

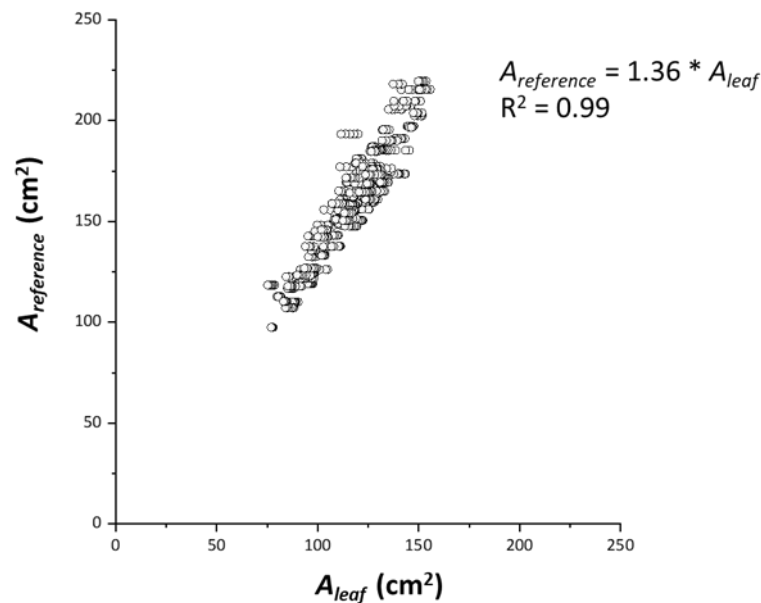


**Figure 4.3** Droplet size distribution after the 1<sup>st</sup> spray.



**Figure 4.4** Initial mass of a leaf before spraying and the stepwise increase in leaf mass after each of the 6 sprays. The red arrows indicate the times of image acquisition.

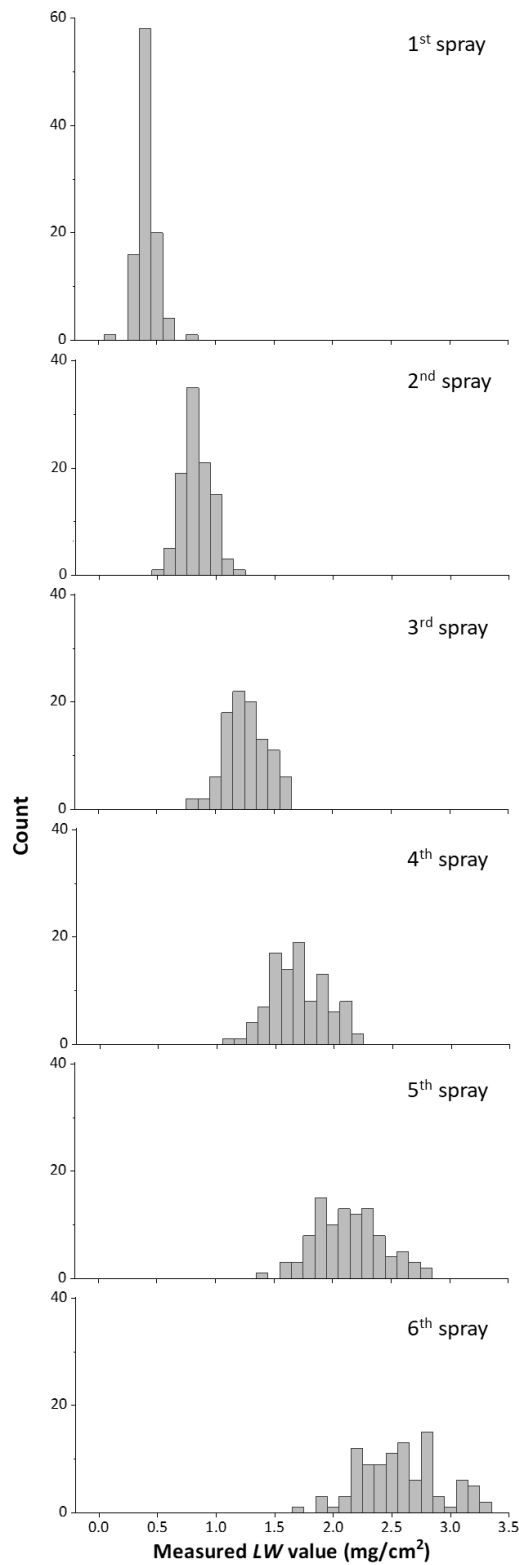
Figure 4.5 illustrates the comparison between  $A_{leaf}$  and  $A_{reference}$  measurements. The area of the scanned leaf had an average value of  $159 \text{ cm}^2$ , with a standard deviation of  $29 \text{ cm}^2$ . An  $R^2$  of 0.99 for the linear relationship underscores the appropriateness of utilizing  $A_{leaf}$  to construct the predictive model. It is notable that  $A_{leaf}$  is smaller than  $A_{reference}$ . This discrepancy can be attributed to two factors: (1) by cutting the leaf,  $A_{reference}$  captured the 3D curvature of the leaf surface, while  $A_{leaf}$  only provided the 2D projection of the leaf, (2) some parts of the leaves are excluded to the background by the  $A_{leaf}$  determination algorithm to avoid false positives. Since the exclusion of certain leaf areas would correspondingly exclude the droplets present in those regions, the  $LW$  will remain unaffected.



**Figure 4.5** Leaf area segmented from the laser image ( $A_{leaf}$ ) vs leaf area measured by the scanner ( $A_{reference}$ ).

In total, 700  $LW$  values were recorded, with 100 readings (100 leaves) for each spraying status, from no spray to the 6<sup>th</sup> spray. Figure 4.6 illustrates the distribution of  $LW$  following each spray. It has to be noted that the 100  $LW$  values without spray consequently had a value of  $0 \text{ mg/cm}^2$ , which is not shown in Figure 4.6. Across all 700  $LW$  values, the average and maximum were  $1.3 \text{ mg/cm}^2$  and  $3.3 \text{ mg/cm}^2$ , respectively. The distribution of  $LW$  showed a higher variance as the number of sprays increased. To understand this trend, it has to be considered that after every spray, the  $LW$  conformed to a normal distribution,  $N(\mu, \sigma^2)$ . Thus, for  $n$  times spraying,

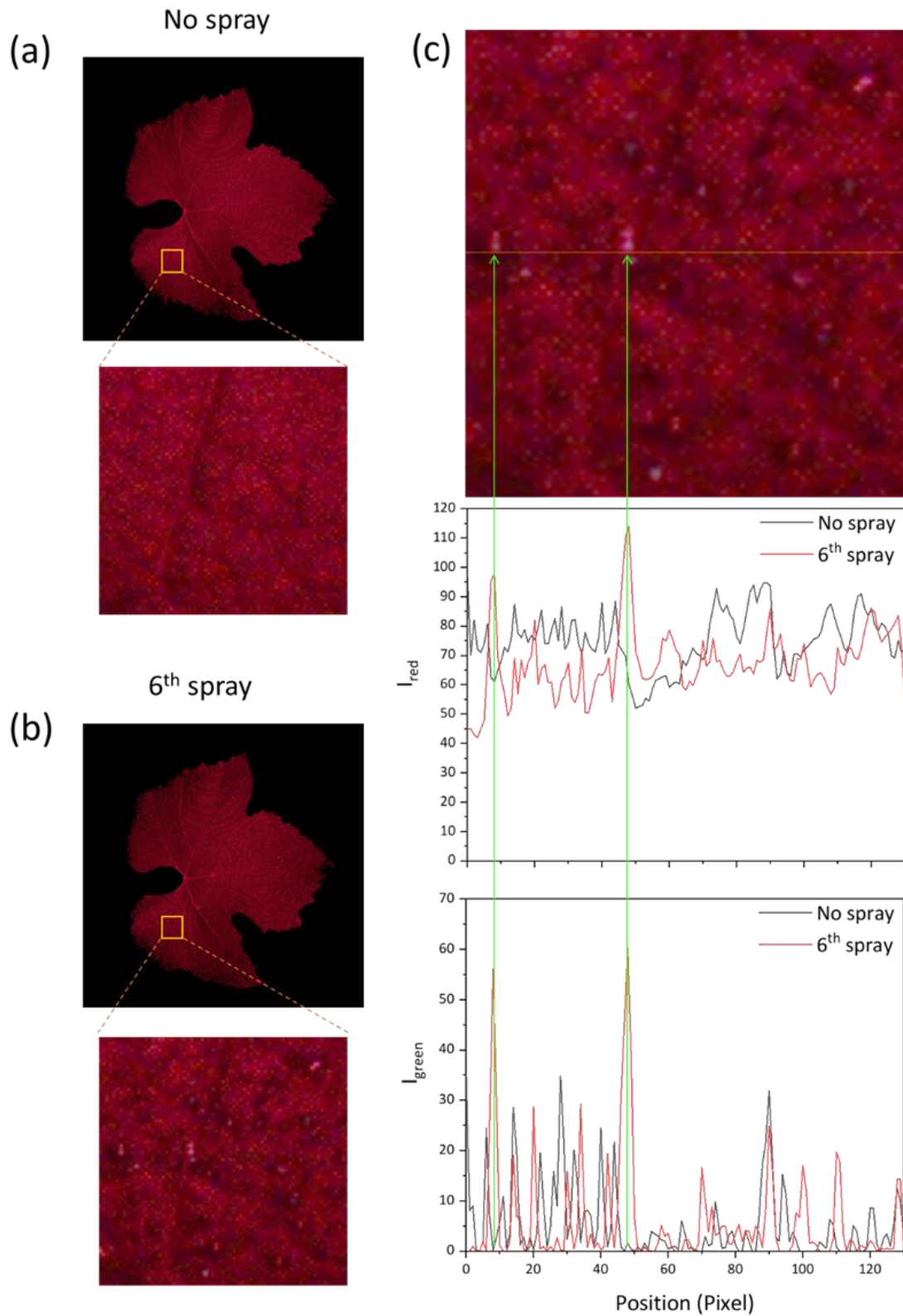
the distribution became  $N(n\mu, n\sigma^2)$ , indicating a higher variance.



**Figure 4.6** Distribution of the measured leaf wetness (*LW*) values after each spray.

### 4.4.3 Image analysis

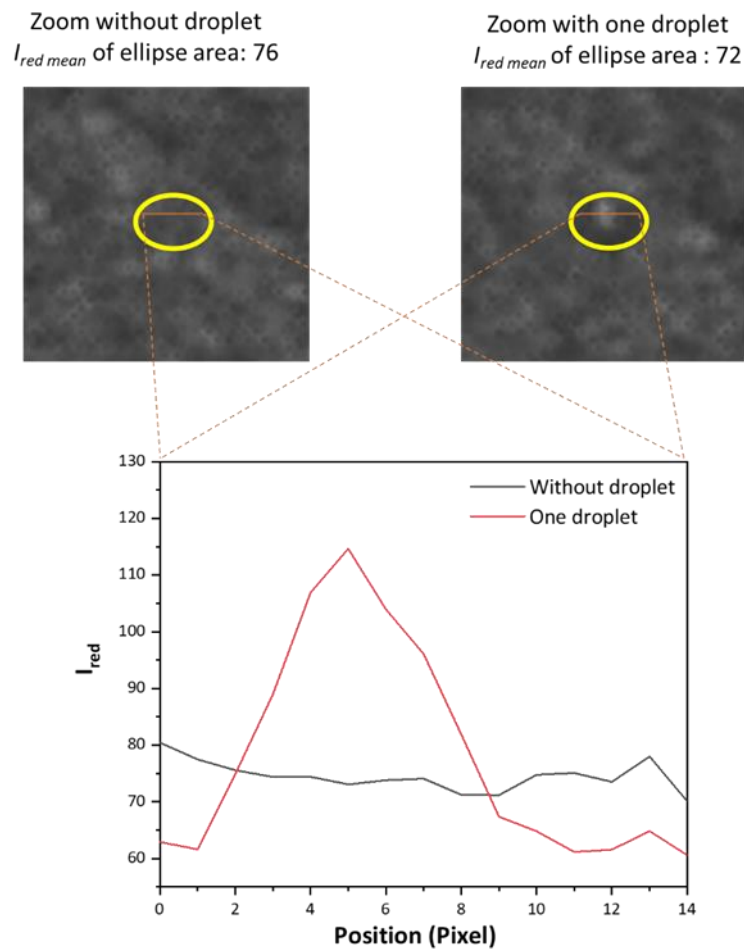
Figure 4.7 displays exemplarily images of a leaf before and after the 6<sup>th</sup> spray. When zooming in on the same area (Figure 4.7a, b), it became apparent that the spatial pattern of light reflections differed. Before spraying, there were only slight differences in brightness across the leaf. In contrast, after the 6<sup>th</sup> spray, the differences in brightness were much more pronounced, particularly in the form of darker areas and a few strongly reflecting points. These differences were even more noticeable when the red channel intensity ( $I_{red}$ ) and the green channel intensity ( $I_{green}$ ) are displayed along a line from the original RGB image (Figure 4.7c). With water present on the leaf,  $I_{red}$  were generally smaller after spraying. However, a few positions on the sprayed leaf show bright reflection peaks that were larger than those of the leaf before spraying. These bright reflection peaks were even more detectable with  $I_{green}$ , due to relatively weaker background noise in the green channel information. Thus, we used the green channel information to identify and count the number of droplets ( $N_{droplet}$ ) in this study.



**Figure 4.7** Image of a leaf and zoomed-in view of the marked area with no spray (a) and after the 6<sup>th</sup> spray (b); (c) The profiles of red channel intensities ( $I_{red}$ ) and green channel intensities ( $I_{green}$ ).

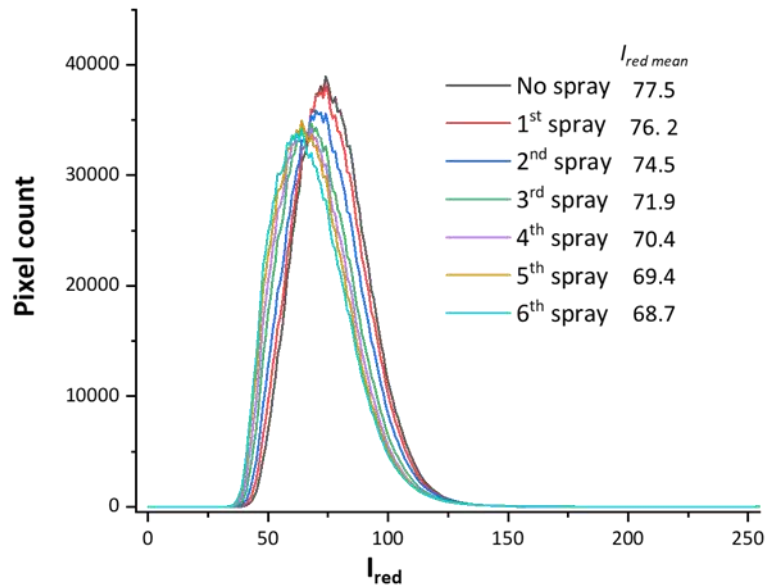


Figure 4.8 shows profiles of  $I_{red}$  of the same leaf area with and without a droplet. The droplet, about 14 pixels in diameter (1.4 mm at 0.1 mm/pixel resolution), had  $I_{red}$  ranging from 60 to 115. A pronounced peak, indicating high reflection, was present at its center, which was also observed by Foday Jr et al. (2022). Without the droplet,  $I_{red}$  was more uniform across the diameter with values between 70 and 80.  $I_{red\ mean}$  of the ellipse area was 72 with the droplet and 76 without it, revealing a lesser average reflection for the droplet-covered area, despite its central peak.



**Figure 4.8** Profiles of the red channel intensity  $I_{red}$  of the same leaf area (marked with ellipse) with and without droplet.

Figure 4.9 shows exemplarily distributions of  $I_{red}$  for one leaf at different spraying status (0 -6 sprays). All distributions had a unimodal curve. After each spray the maximum pixel count decreased, the vertex moved to the left., and  $I_{red\ mean}$  decreased. Similarly, Swarup et al. (2020) also showed darker images when the strawberry leaves became wet.



**Figure 4.9** Smoothed intensity distributions (moving average of period 9) of a leaf's red channel at different spraying status (0 – 6 sprays).

The reduction in  $I_{red\ mean}$  for the entire leaf after spraying could be attributed to two factors: (1) for a large droplet, the image directly showed that the peripheral area of the droplet could reflect light away from the camera; (2) for a small droplet whose size was close to or less than the camera resolution, although the droplets' shape become indistinguishable in their occupied pixels, the light intensity of those pixels might also be reduced due to the average reflection effect of the whole droplet.

Figure 4.10 shows the difference of identified droplets on a sample leaf before and after the 6<sup>th</sup> spray. There were 9 droplets detected as false positives on the leaf before spraying. On closer investigation, the identification error could be attributed to white dots on the leaf. Conversely, this means that the developed method for droplet identification is not suitable if the leaf is diseased and has white dots, such as those resulting from powdery mildew. On the leaf after the 6<sup>th</sup> spray 338 droplets were identified but they were not evenly distributed. Droplets were rarely identified at the rightmost position of the leaf. Since larger droplets were also present at this position, the poor droplet detection might be explained by the leaf curvature. By an inclined leaf surface, the reflection of the droplets can be deflected in such a way that a reflection peak in the center of the droplet (Figure 4.8) cannot be detected by the camera (Butt et al., 2022; Wang et al., 2015). In practical settings, leaf orientation is randomly

distributed, and therefore, to obtain more accurate predictions, this technology may need to scan a larger number of leaves.

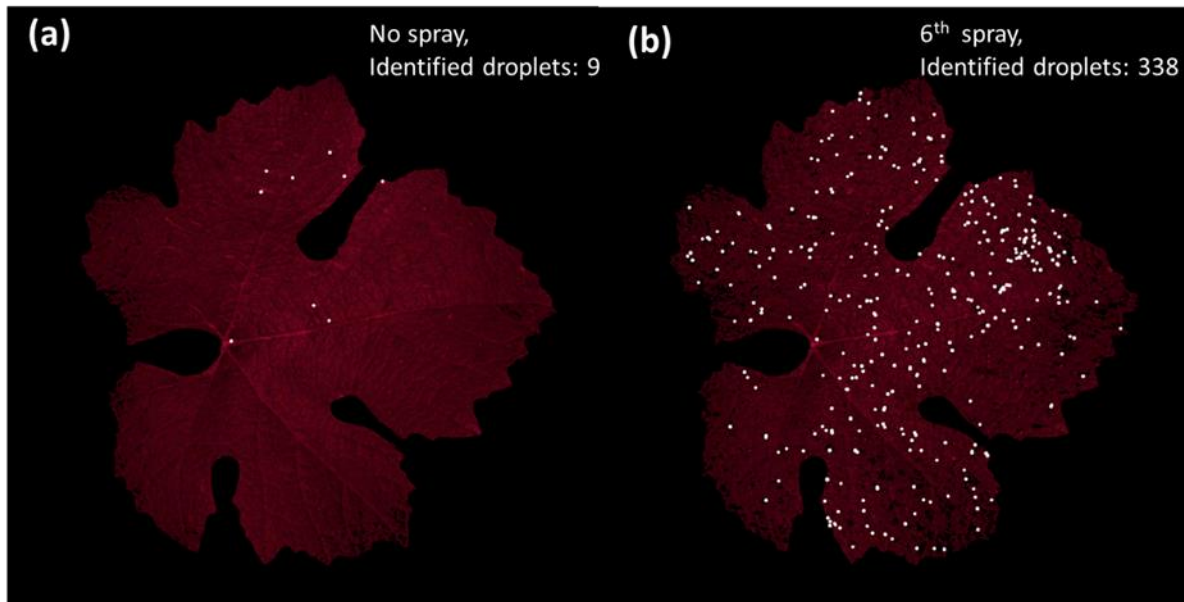


**Figure 4.10** Droplets Identified by image processing on a leaf before spraying (left) and after the 6<sup>th</sup> spray (right).

#### 4.4.4 The prediction of *LW* values

Based on the measurements and the results obtained, three parameters were identified and used to predict water deposition on the leaf, namely  $A_{leaf}$ ,  $I_{red\ mean}$  and  $N_{droplet}$ . Figure 4.11 shows the results of the GAM model with different input parameter combinations after 1000 times modeling. When  $A_{leaf}$  and  $I_{red\ mean}$  were used as parameter input, a prediction was obtained with an  $R^2$  of 0.083 (Figure 4.11a). With  $A_{leaf}$  and  $N_{droplet}$ , the prediction was distinctly better ( $R^2 = 0.713$ ) (Figure 4.11b), while best prediction was obtained by including all three parameters ( $A_{leaf}$ ,  $I_{red\ mean}$  and  $N_{droplet}$ ;  $R^2 = 0.779$ ) (Figure 4.11c). Still, some *LW* values that were actually 0 were predicted to be about 0 - 0.6 mg/cm<sup>2</sup>, indicating a potential for false positive predictions.

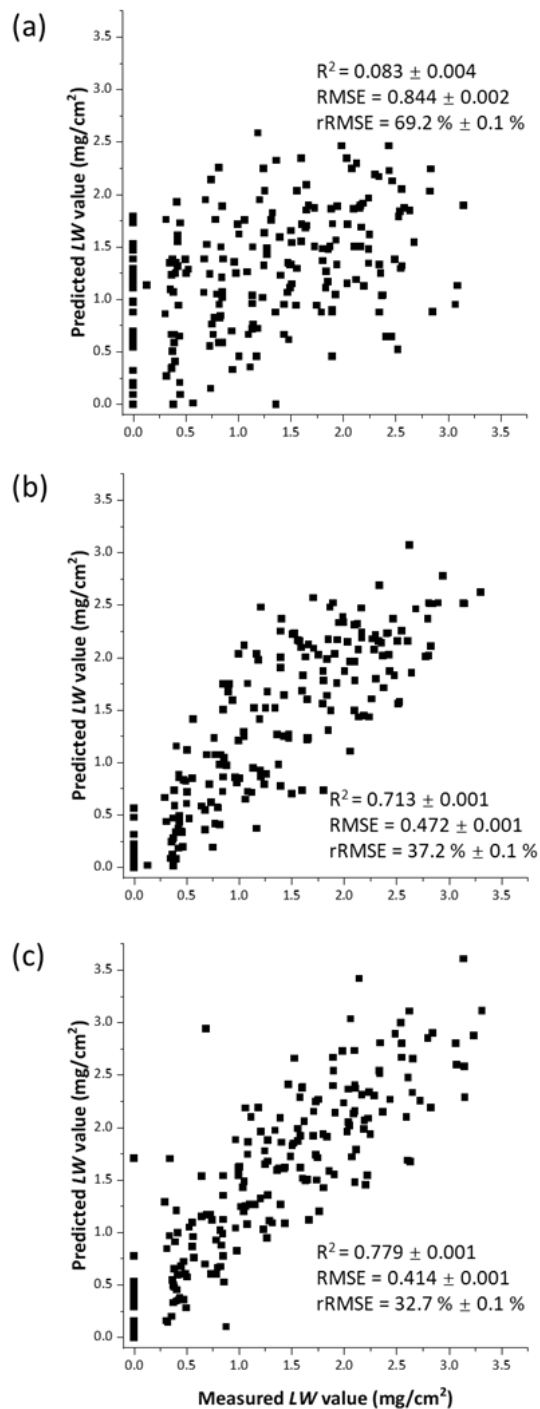


**Figure 4.11** Prediction results of the GAM model, using different combinations of input image features: (a)  $A_{leaf}$ ,  $I_{red\ mean}$ ; (b)  $A_{leaf}$ ,  $N_{droplet}$ ; (c)  $A_{leaf}$ ,  $I_{red\ mean}$ ,  $N_{droplet}$ , where  $A_{leaf}$  represents image leaf area,  $I_{red\ mean}$  represents mean red channel intensity,  $N_{droplet}$  represents identified number of droplets. The  $R^2$ , RMSE and rRMSE shown in the figures are the average of 1000 times modeling.

As discussed above, information of droplets smaller than or close to the image resolution are included by  $I_{red\ mean}$ , while droplets much larger than image resolution are more accurately represented by using the green channel. Therefore, the best prediction for  $LW$  values ( $R^2 = 0.779$ ) was obtained when both small and large droplets were included (Figure 4.11c). In contrast, when building the model with only  $A_{leaf}$  and  $I_{red\ mean}$ , the prediction became worse with an  $R^2 = 0.083$  (Figure 4.11a). Using  $I_{red\ mean}$  alone to represent water information might have been influenced by the variability between leaves, leading to significant uncertainty in the prediction. A much better prediction ( $R^2 = 0.713$ ) was achieved with only leaf area and  $N_{droplet}$  as captured by the green channel for model building (Figure 4.11b).

## 4.5 Conclusions

This study demonstrates a novel no-contact method for leaf wetness measurement for quantifying leaf wetness. Under a 658 nm laser, increased water droplets on leaves resulted in decreased leaf mean intensity in the red channel of the RGB camera, and more easily measurable high-brightness pixels in the green channel. By applying a generalized additive model based on machine learning to these features, the study achieved an  $R^2$  of 0.779 with an rRMSE of 32.7 %. The study also revealed that, both image resolution and leaf orientation can impact these features, providing valuable insights for practice implementation. Besides measuring leaf wetness, this research could also aid in evaluating spray performance without requiring an extra tracer. However, the study did not investigate the measurement of water film, another form of leaf wetness, which requires further investigation.

### Conflicts of Interest

The authors declare no conflict of interest.

### Acknowledgements

Funding: The project “Prognose und Detektion von Pilzerkrankungen im Weinbau durch feinmaschige Messung des Mikroklimas und Einsatz bildgebender Messverfahren (FungiSens)” (FKZ 281B200516) is supported by funds of the Federal Ministry of Food and Agriculture (BMEL) based on a decision of the Parliament of the Federal Republic of Germany via the Federal Office for Agriculture and Food (BLE) under the innovation support program.

## 4.6 References

- Acharya, B. S., Stebler, E., & Zou, C. B. (2017). Monitoring litter interception of rainfall using leaf wetness sensor under controlled and field conditions. *Hydrological Processes*, *31*(1), 240–249. <https://doi.org/10.1002/hyp.11047>
- Butt, H.-J., Liu, J., Koynov, K., Straub, B., Hinduja, C., Roismann, I., Berger, R., Li, X., Vollmer, D., Steffen, W., & Kappl, M. (2022). Contact angle hysteresis. *Current Opinion in Colloid & Interface Science*, *59*, 101574. <https://doi.org/https://doi.org/10.1016/j.cocis.2022.101574>
- Chungu, C., Gilbert, J., & Townley-Smith, F. (2001). Septoria tritici blotch development as affected by temperature, duration of leaf wetness, inoculum concentration, and host. *Plant Disease*, *85*(4), 430–435. <https://doi.org/10.1094/PDIS.2001.85.4.430>
- Despotovic, M., Nedic, V., Despotovic, D., & Cvetanovic, S. (2016). Evaluation of empirical models for predicting monthly mean horizontal diffuse solar radiation. *Renewable and Sustainable Energy Reviews*, *56*, 246–260. <https://doi.org/10.1016/j.rser.2015.11.058>
- Dey, S., Amin, E. M., & Karmakar, N. C. (2020). Paper based chipless RFID leaf wetness detector for plant health monitoring. *IEEE Access*, *8*, 191986–191996. <https://doi.org/10.1109/ACCESS.2020.3033191>
- Duvdevani, S. (1947). An optical method of dew estimation. *Quarterly Journal of the Royal Meteorological Society*, *73*(317–318), 282–296. <https://doi.org/https://doi.org/10.1002/qj.49707331705>
- Foday Jr, E. H., Sesay, T., Koroma, E. B., Kanneh, A. A. G. S., Chineche, E. B., Jalloh, A. Y., & Koroma, J. M. (2022). Biotemplate Replication of Novel *Mangifera indica* Leaf (MIL) for Atmospheric Water Harvesting: Intrinsic Surface Wettability and Collection Efficiency. *Biomimetics*, *7*(4), 147. <https://doi.org/10.3390/biomimetics7040147>
- Foqué, D., Dekeyser, D., Langenakens, J., & Nuyttens, D. (2018). Evaluating the usability of a leaf wetness sensor as a spray tech monitoring tool. *Aspects of Applied Biology*, *137*(100848).
- Gama, A. B., Perondi, D., Dewdney, M. M., Fraisse, C. W., Small, I. M., & Peres, N. A. (2022). Evaluation of a multi-model approach to estimate leaf wetness duration: an essential input for disease alert systems. *Theoretical and Applied Climatology*, *Pitblado 1992*. <https://doi.org/10.1007/s00704-022-04036-1>
- Hornero, G., Gaitán-Pitre, J. E., Serrano-Finetti, E., Casas, O., & Pallas-Areny, R. (2017). A novel low-cost smart leaf wetness sensor. *Computers and Electronics in Agriculture*, *143*(April), 286–292. <https://doi.org/10.1016/j.compag.2017.11.001>

Huber, L., & Gillespie, T. J. (1992). Modeling Leaf Wetness in Relation to Plant Disease Epidemiology. *Annual Review of Phytopathology*, 30(1), 553–577. <https://doi.org/10.1146/annurev.py.30.090192.003005>

Liu, R., Wang, H., Guzmán, J. L., & Li, M. (2022). A model-based methodology for the early warning detection of cucumber downy mildew in greenhouses: An experimental evaluation. *Computers and Electronics in Agriculture*, 194. <https://doi.org/10.1016/j.compag.2022.106751>

Neufeld, K. N., & Ojiambo, P. S. (2012). Interactive effects of temperature and leaf wetness duration on sporangia germination and infection of cucurbit hosts by *pseudoperonospora cubensis*. *Plant Disease*, 96(3), 345–353. <https://doi.org/10.1094/PDIS-07-11-0560>

Osroosh, Y., & Peters, R. T. (2019). Detecting fruit surface wetness using a custom-built low-resolution thermal-RGB imager. *Computers and Electronics in Agriculture*, 157(January), 509–517. <https://doi.org/10.1016/j.compag.2019.01.023>

Otsu, N. (1979). A Threshold Selection Method from Gray-Level Histograms. *IEEE Transactions on Systems, Man, and Cybernetics*, 9(1), 62–66. <https://doi.org/10.1109/TSMC.1979.4310076>

Park, J., Shin, J. Y., Kim, K. R., & Ha, J. C. (2019). Leaf wetness duration models using advanced machine learning algorithms: Application to farms in Gyeonggi Province, South Korea. *Water (Switzerland)*, 11(9). <https://doi.org/10.3390/w11091878>

Patel, A., Lee, W. S., Peres, N. A., & Fraisse, C. W. (2021). Strawberry plant wetness detection using computer vision and deep learning. *Smart Agricultural Technology*, 1(September), 100013. <https://doi.org/10.1016/j.atech.2021.100013>

Patle, K. S., Saini, R., Kumar, A., Surya, S. G., Palaparthi, V. S., & Salama, K. N. (2021). IoT Enabled, Leaf Wetness Sensor on the Flexible Substrates for In-Situ Plant Disease Management. *IEEE Sensors Journal*, 21(17), 19481–19491. <https://doi.org/10.1109/JSEN.2021.3089722>

Ranjan, R., Sinha, R., Khot, L. R., & Whiting, M. (2022). Thermal-RGB imagery and in-field weather sensing derived sweet cherry wetness prediction model. *Scientia Horticulturae*, 294(November 2021), 110782. <https://doi.org/10.1016/j.scienta.2021.110782>

Rowlandson, T., Thomas, C., Gillespie, T., Hornbuckle, B., Sentelhas, P., & Gleason, M. (2014). Reconsidering Leaf Wetness Duration Determination for Plant Disease Management. *Plant Disease*, 99(3), 310–319. <https://doi.org/10.1094/pdis-05-14-0529-fe>

Schneider, C. A., Rasband, W. S., & Eliceiri, K. W. (2012). NIH Image to ImageJ: 25 years of image analysis. *Nature Methods*, 9(7), 671–675. <https://doi.org/10.1038/nmeth.2089>

- Sentelhas, P. C., Dalla Marta, A., Orlandini, S., Santos, E. A., Gillespie, T. J., & Gleason, M. L. (2008). Suitability of relative humidity as an estimator of leaf wetness duration. *Agricultural and Forest Meteorology*, *148*(3), 392–400. <https://doi.org/10.1016/j.agrformet.2007.09.011>
- Sentelhas, P. C., Gillespie, T. J., Gleason, M. L., Monteiro, J. E. B. A., & Helland, S. T. (2004a). Operational exposure of leaf wetness sensors. *Agricultural and Forest Meteorology*, *126*(1–2), 59–72. <https://doi.org/10.1016/j.agrformet.2004.05.009>
- Sentelhas, P. C., Monteiro, J. E. B. A., & Gillespie, T. J. (2004b). Electronic leaf wetness duration sensor: Why it should be painted. *International Journal of Biometeorology*, *48*(4), 202–205. <https://doi.org/10.1007/s00484-004-0200-z>
- Shin, J. Y., Park, J., & Kim, K. R. (2021). Emulators of a physical model for estimating leaf wetness duration. *Agronomy*, *11*(2), 1–18. <https://doi.org/10.3390/agronomy11020216>
- Swarup, A., Lee, W. S., Peres, N., & Fraise, C. (2020). Strawberry Plant Wetness Detection Using Color and Thermal Imaging. *Journal of Biosystems Engineering*, *45*(4), 409–421. <https://doi.org/10.1007/s42853-020-00080-9>
- Verdú, S., Perez, A. J., Barat, J. M., & Grau, R. (2021). Laser-backscattering imaging for characterising the dairy matrix in different phases during curd processing. *Food Control*, *128*, Article 108193. <https://doi.org/10.1016/j.foodcont.2021.108193>
- Wang, H., Sanchez-Molina, J. A., Li, M., & Berenguel, M. (2020). Development of an empirical tomato crop disease model: a case study on gray leaf spot. *European Journal of Plant Pathology*, *156*(2), 477–490. <https://doi.org/10.1007/s10658-019-01897-7>
- Wang, H., Shi, H., & Wang, Y. (2015). The Wetting of Leaf Surfaces and Its Ecological Significances. In M. Aliofkhazraei (Ed.), *Wetting and Wettability*. IntechOpen. <https://doi.org/10.5772/61205>
- Wang, Z., Zheng, C., Li, T., & He, X. (2021). Analysing the preference for pesticide spray to be deposited at leaf-tips. *Biosystems Engineering*, *204*, 247–256. <https://doi.org/10.1016/j.biosystemseng.2021.01.012>
- Wen, D., Ren, A., Ji, T., Flores-Parra, I. M., Yang, X., & Li, M. (2020). Segmentation of thermal infrared images of cucumber leaves using K-means clustering for estimating leaf wetness duration. *International Journal of Agricultural and Biological Engineering*, *13*(3), 161–167. <https://doi.org/10.25165/j.ijabe.20201303.4301>
- Wu, Z., Spohrer, K., Nagle, M., & Müller, J. (2023). Investigating the influence of pore size, pore fluid and wavelength on backscattering images with sintered glass filter matrices as experimental models. *Postharvest Biology and Technology*, *200*(March), 112329. <https://doi.org/10.1016/j.postharvbio.2023.112329>



Zhu, H., Salyani, M., & Fox, R. D. (2011). A portable scanning system for evaluation of spray deposit distribution. *Computers and Electronics in Agriculture*, 76(1), 38–43. <https://doi.org/10.1016/j.compag.2011.01.003>

# 5

## General discussion

Non-destructive optical sensor technology (NDOST) is a vital component of modern agriculture, enabling swift data collection without damaging subject matter. Laser technology, with its unique capabilities, has greatly advanced NDOST. One such promising and cost-effective technique is laser backscattering imaging (LBI). The scattering nature of agricultural products makes LBI a practical solution for many scenarios. However, the prevailing basic research concerning LBI tends to oversimplify the intricate interaction between light and food. To address this, we explored the effects of pore size and pore fluid on backscattering images, by employing sintered glass filter matrices as experimental models. LBI also holds potential for further applications. Therefore, we examined the feasibility of using LBI to monitor the plant oil sedimentation process and to measure leaf wetness.

### 5.1 The effects of pore size and pore fluid on LBI

While many scientists viewed food as a single entity and sought to understand its general optical parameters (Baranyai and Zude, 2009; Lorente et al., 2015; Zude-Sasse et al., 2019), this study aimed to delve into cell-level parameters to better understand the LBI phenomena. Under controlled conditions, we found that the refractive index difference between the pore fluid and the matrix affects the backscattering area under controlled conditions. This goes together with the predictions for the soluble solid content in fruit or vegetables (Mohd Ali et al., 2017; Qing et al., 2008; Sanchez et al., 2020). Furthermore, we found that the pore diameter and the difference in refractive index collectively influenced the scattering area.

Considering that cell sizes along the transection radius of fruit may vary (Bain and Robertson, 1951; Marcelis and Baan Hofman-Eijer, 1993; Reeve et al., 1971), this implies a potential strategy for better measurements by understanding how food cells affect laser light. This research direction would require meticulously prepared experimental conditions but could yield valuable fundamental knowledge. Interestingly, Nishio et al. (1985) developed a microscope laser light scattering spectroscopy for single cells.

One key challenge when conducting basic research on LBI is controlling variables due to the heterogeneity of agricultural products. In this research we used glass filter matrices with known and controlled pore sizes (1 - 160  $\mu\text{m}$ ). The matrices could further help understand other basic research problems related to LBI. For example, current methods used to correct the curvature of the food surface are evaluated, based on the accuracy of the final prediction model (Peng and Lu, 2006; Qing et al., 2007). Although this metric is practically useful, it's indirect. The cylindrical shape matrices used in this research, available in various sizes, could help directly understand surface curvature effects under controlled conditions.

This research still has its limitations. Using a glass filter matrix as a model for a bio-organism may inevitably lead to discrepancies compared to the actual structure of plants. Also, the experiment's result may be linked to the thickness of the porous matrix, since more light could transmit through the matrix when there was a larger pore size with a smaller refractive index difference. Therefore, future studies should also explore the influence of matrix thickness.

## **5.2 Applying LBI to oil sedimentation process**

In the exploration of using an LBI system for the sedimentation process of crude sesame oil, we observed two distinct laser light scattering phenomena: a scattering pattern at the oil surface and a Tyndall effect within the oil. The scattering pattern at the oil surface holds potential for predicting early stage sedimentation. Scattering image features were analyzed and related to the range of heights between 0 and -10 cm, using a power function. This approach resulted in a coefficient of determination ( $R^2$ ) of 0.97. At the onset of the sedimentation process, numerous particles were present at the surface of the crude oil, amplifying the scattering phenomenon. The Tyndall effect, on the other hand, suggests a promising approach for the continuous monitoring of the scattering effect. As the

sedimentation process advanced, the laser path demonstrated an increasing linear shape. Expanding the cross section of the sedimentation tank could not only expedite the sedimentation process (Karaj and Müller, 2014), but also reduce the power required for the laser to penetrate deeper.

Previous studies have shown the capability of LBI to continuously monitor the milk curdling process (Verdú et al., 2021a, 2021b). Coupled with our findings, it indicates that LBI may be applicable in additional agricultural scenarios when state transitions occur within colloids or suspensions. Utilizing the Tyndall effect, Huang et al., (2021) achieved a 5400-fold accuracy improvement over the conventional method for detecting  $\text{Hg}^{2+}$  in a colloidal solution, implying that the Tyndall effect has potential for high accuracy.

The existence of Tyndall effect essentially indicates the presence of numerous small particles inside the oil that have not yet sedimented. Hence, measuring the particle size and the optical properties of the oil could facilitate a deeper understanding of the scattering effect. Future research could also investigate more types of oil, as this study was conducted solely with sesame oil. Additionally, in the LBI system employed in this study, both the laser and the camera were cheap. However, image analysis was performed on a computer. The application of an embedded system for image analysis could potentially drive down the system's overall cost even further.

### **5.3 Applying LBI to leaf wetness measurement**

Leaf wetness duration is a crucial factor in plant fungi disease management. This study used an LBI system to measure grape leaf wetness. Unlike the conventional LBI methodology which uses dot lasers (Adebayo et al., 2016; Mollazade et al., 2012), this study used two expanded lasers and analyzed the variation in light behaviors caused by grape leaves and water droplets. Water droplets exhibited strong reflection of laser light—a property not shared by the leaves. The prediction model achieved an  $R^2$  of 0.78 on the test dataset. Geng et al., (2021) differentiated stones and clods from potatoes based on the variance in their scattering properties. Together with our findings, this suggests that LBI technology has potential for use in scenarios where materials with varying optical properties coexist.

We identified a negative correlation between the mean intensity of a laser image's red channel and the weight of water droplets on the surface. This is likely due to the droplets reflecting a substantial amount of light away from the camera. Furthermore, we found that the green channel could be used to quantify droplet information, as only intense light signals can trigger the pixels in the green channel. This suggests that, regardless of the laser's wavelength, all channels in an RGB image could potentially provide valuable information for LBI image analysis. Verdú et al., (2021a) also made use of data from different color channels to bolster their analysis.

The image resolution and leaf orientation should influence the features extracted from the image. In the image, droplets that were smaller than one pixel appeared as darker spots, while droplets much larger than one pixel could present reflective points. Also, the orientation of the leaf could alter the direction of reflected light. Therefore, before implementing this method in practical applications, further research is needed to understand the impact of image resolution and leaf orientation.

## **5.4 Conclusion**

The use of laser technology as a light source for NDOST is prevalent across various domains in contemporary agriculture. Light scattering, a fundamental phenomenon for numerous agricultural products, makes LBI an emerging technology that is particularly suitable for agriculture. This study aims to broaden fundamental knowledge and application scenarios of LBI within agricultural contexts. Our findings emphasize the importance of considering the cell size of agricultural products when implementing LBI. The porous matrix used in the research allowed experiments about LBI under controlled conditions. In addition, LBI was found to be useful in monitoring plant oil sedimentation and measuring leaf wetness. This suggests the suitability of LBI in scenarios involving state changes for suspensions or colloids, and where remarkable optical property differences are present when different materials coexist. Furthermore, our research reveals that different color channels can provide valuable insights when using an RGB camera, regardless of the laser wavelength.

In an effort to gain a fundamental understanding of LBI, we used materials with controllable pore and material properties. However, this approach may inherently introduce certain errors

into the research. In terms of the research on sesame oil sedimentation, the next steps could involve employing a sedimentation tank with a larger cross-sectional area but smaller height, and exploring various oil types. As for the measurement of leaf wetness, future investigations may focus on examining the impact of leaf orientation and image resolution.

## 5.5 Outlook

In the contemporary world, food safety is a critical issue under increasing pressure. This pressure arises from various factors such as climate change, geopolitical tensions, and the escalating demand for an improved quality of life. To confront these challenges and ensure a resilient food supply chain, the implementation of affordable and swift sensor technologies is crucial. A notable player in this realm could be LBI technology, an economical solution that contributes to food safety.

At present, foundational research primarily focuses on macro-level observations. To gain an in-depth understanding, emphasis needs to be placed on micro-level insights, specifically on understanding how plant cells interact with light. Given the vast array of plant cell and tissue types, it is paramount to construct a database detailing how light of varying wavelengths interacts with different plant cells and tissues. This database could enhance our understanding of the LBI and also many other optical measurement technologies in agriculture. Leveraging such a micro-level database, coupled with advancements in computer science, we could potentially simulate or build accurate prediction model based on a micro scale in the future. Although the simulation would require considerable computational resources, the rapid evolution of computer chips over the past decade makes this a promising proposition.

The scattering nature of agricultural products means that the applications of LBI are vast, and it is crucial to continue exploring new application scenarios. From an economic perspective, discovering more applications will attract further funding to this field, thereby propelling its development. The fundamental components of LBI, such as lasers and cameras, are becoming more affordable, which bodes well for the future development of LBI in agriculture. Optical measurement could potentially be a highly accurate method. However, noise from the camera, light sources, or vibrating environments could compromise this accuracy. Enhancing the stability of laser light and reducing camera-induced noise are key to improving the accuracy

of the system during application.

The advancement of optical techniques in medical technology may provide valuable guidance for their utilization in the agricultural sector. From a physical perspective, both medical and agricultural applications involve the use of light interacting with biological organisms. Given the typically higher level of funding in medical research, non-destructive sensor techniques have a good chance to mature faster in the medical field. For instance, nuclear magnetic resonance technology emerged as a medical technology before being adopted in agriculture. Therefore, it is suggested that future researchers engaged in the development of NDOST for agriculture also keep an eye on the relative advancements in medical technology, as these might offer useful insights for their work.

## 5.6 References

- Adebayo, S. E., Hashim, N., Abdan, K., & Hanafi, M. (2016). Application and potential of backscattering imaging techniques in agricultural and food processing – A review. *Journal of Food Engineering*, 169, 155–164. <https://doi.org/10.1016/J.JFOODENG.2015.08.006>
- Bain, J. M., & Robertson, R. N. (1951). The physiology of growth in apple fruits. I. Cell size, cell number, and fruit development. *Australian Journal of Scientific Research. Ser. B: Biological Sciences*, 4(2), 75–107. <https://doi.org/10.1071/bi9510075>
- Baranyai, L., & Zude, M. (2009). Analysis of laser light propagation in kiwifruit using backscattering imaging and Monte Carlo simulation. *Computers and Electronics in Agriculture*, 69(1), 33–39. <https://doi.org/10.1016/j.compag.2009.06.011>
- Geng, J., Min, H., & Rao, X. (2021). Separation of clods and stones from harvested potatoes using laser backscattering imaging technique. *Journal of Food Measurement and Characterization*, 15(4), 3262–3273. <https://doi.org/10.1007/s11694-021-00896-9>
- Huang, J., Mo, X., Fu, H., Sun, Y., Gao, Q., Chen, X., Zou, J., Yuan, Y., Nie, J., & Zhang, Y. (2021). Tyndall-effect-enhanced supersensitive naked-eye determination of mercury (II) ions with silver nanoparticles. *Sensors and Actuators, B: Chemical*, 344(March), 130218. <https://doi.org/10.1016/j.snb.2021.130218>
- Karaj, S., & Müller, J. (2014). Effect of container depth and sedimentation time on quality of *Jatropha curcas* L. oil. *Fuel*, 118, 206–213. <https://doi.org/10.1016/j.fuel.2013.10.066>

- Lorente, D., Zude, M., Idler, C., Gómez-Sanchis, J., & Blasco, J. (2015). Laser-light backscattering imaging for early decay detection in citrus fruit using both a statistical and a physical model. *Journal of Food Engineering*, 154, 76–85. <https://doi.org/10.1016/j.jfoodeng.2015.01.004>
- Marcelis, L. F. M., & Baan Hofman-Eijer, L. R. (1993). Cell division and expansion in the cucumber fruit. *Journal of Horticultural Science*, 68(5), 665–671. <https://doi.org/10.1080/00221589.1993.11516398>
- Mohd Ali, M., Hashim, N., Bejo, S. K., & Shamsudin, R. (2017). Quality evaluation of watermelon using laser-induced backscattering imaging during storage. *Postharvest Biology and Technology*, 123, 51–59. <https://doi.org/10.1016/j.postharvbio.2016.08.010>
- Mollazade, K., Omid, M., Tab, F. A., & Mohtasebi, S. S. (2012). Principles and Applications of Light Backscattering Imaging in Quality Evaluation of Agro-food Products: a Review. *Food and Bioprocess Technology*, 5, 1465–1485. <https://doi.org/10.1007/s11947-012-0821-x>
- Nishio, I., Peetermans, J., & Tanaka, T. (1985). Microscope laser light scattering spectroscopy of single biological cells. *Cell Biochemistry and Biophysics*, 7(2), 91–105. <https://doi.org/10.1007/BF02784485>
- Peng, Y., & Lu, R. (2006). Improving apple fruit firmness predictions by effective correction of multispectral scattering images. *Postharvest Biology and Technology*, 41(3), 266–274. <https://doi.org/10.1016/j.postharvbio.2006.04.005>
- Qing, Z., Ji, B., & Zude, M. (2007). Predicting soluble solid content and firmness in apple fruit by means of laser light backscattering image analysis. *Journal of Food Engineering*, 82(1), 58–67. <https://doi.org/10.1016/j.jfoodeng.2007.01.016>
- Qing, Z., Ji, B., & Zude, M. (2008). Non-destructive analyses of apple quality parameters by means of laser-induced light backscattering imaging. *Postharvest Biology and Technology*, 48(2), 215–222. <https://doi.org/10.1016/j.postharvbio.2007.10.004>
- Reeve, R. M., Timm, H., & Weaver, M. L. (1971). Cell size in Russet Burbank potato tubers with various levels of nitrogen and soil moisture tensions. *American Potato Journal*, 48(12), 450–456. <https://doi.org/10.1007/BF02862060>
- Sanchez, P. D. C., Hashim, N., Shamsudin, R., & Mohd Nor, M. Z. (2020). Quality evaluation of sweet potatoes (*Ipomoea batatas* L.) of different varieties using laser light backscattering imaging technique. *Scientia Horticulturae*, 260(July 2019), 108861. <https://doi.org/10.1016/j.scienta.2019.108861>



Verdú, S., Perez, A. J., Barat, J. M., & Grau, R. (2021a). Laser-backscattering imaging for characterising the dairy matrix in different phases during curd processing. *Food Control*, 128, Article 108193. <https://doi.org/10.1016/j.foodcont.2021.108193>

Verdú, S., Pérez, A. J., Barat, J. M., & Grau, R. (2021b). Non-destructive control in cheese processing: Modelling texture evolution in the milk curdling phase by laser backscattering imaging. *Food Control*, 121, Article 107638. <https://doi.org/10.1016/j.foodcont.2020.107638>

Zude-Sasse, M., Hashim, N., Hass, R., Polley, N., & Regen, C. (2019). Validation study for measuring absorption and reduced scattering coefficients by means of laser-induced backscattering imaging. *Postharvest Biology and Technology*, 153(March), 161–168. <https://doi.org/10.1016/j.postharvbio.2019.04.002>

## Summary

Non-destructive optical sensor technology (NDOST) is an essential part of agriculture. The unique capabilities of laser notably enhanced NDOST. Laser backscattering imaging (LBI) is a technology that captures light patterns scattered by a material to analyze its properties. It is particularly suitable for agriculture due to its affordability and the optical scattering nature of agricultural products. The images generated by LBI are related to the optical parameters of the examined objects. Crucial tasks in LBI include the selection of an appropriate laser, the extraction of image features, and the utilization of a prediction model for analysis. LBI has been employed in numerous scenarios, such as maturity detection and drying monitoring. The main challenges for LBI involve establishing a precise theoretical framework and uncovering new applications within agriculture. This study aims to enhance the foundational knowledge about LBI and explore additional application scenarios.

The first study focused on basic research about LBI. Currently, researchers rarely document the cell size of their samples and treat the optical coefficient as a constant within agricultural products, which is questionable. This study's purpose was to use glass filter matrices as controlled models and to evaluate the effects of pore size, different solutes, concentrations, and wavelength. The used porous glass discs had pore diameters ranging from 1 to 160  $\mu\text{m}$ . We applied aqueous solutions of NaCl (0, 1, 2, 3, and 4 mol/L) and  $\text{NaH}_2\text{PO}_4$  (0, 0.8, 1.6, 2.4, and 3.2 mol/L) to fill the pores. The LBI system incorporated laser modules at three different wavelengths (405, 635, 780 nm). The results illustrated that three of the four examined experimental factors (the pore diameter, the solutes, and their concentrations) have a substantial impact on LBI. However, no clear differences in LBI patterns were observed among the three utilized wavelengths. Consequently, when deploying LBI on fruits, for instance, a thorough consideration of cell sizes at various depths from the fruit surface is required.

The second study focused on a possible application scenario of LBI: the sedimentation process of crude sesame oil. Oil sedimentation is a process where gravity is used to remove solid impurities, resulting in a clearer oil. This study examined the sedimentation process in crude sesame oil using LBI. In situ and laboratory experiments were conducted over 30 days, involving an LBI system directly attached to a transparent sedimentation tank with 120L of

crude oil. Both the oil properties and sedimentation curve were analyzed along with the LBI images. There was a dramatic drop in oil particle-related properties (at least 87%), a 90% decrease in water content, and minor changes in oxidation-related properties. The sedimentation speed was about  $-7$  mm/h, then became less than  $-2$  mm/h, revealing two stages: diluted and hindered sedimentation. The crude oil's surface displayed a distinctive scattering spot and a Tyndall effect within the oil, showing an increasing path length as sedimentation proceeded. The findings offer practical insights for enhancing sedimentation tank and LBI system design.

The third study focused on another possible application scenario of LBI: leaf wetness measurement. Leaf wetness plays a pivotal role in managing plant fungi diseases. Existing optical techniques categorize leaf wetness as a binary problem – either wet or dry. In contrast, this research developed a platform capable of semi-automatically measuring droplet deposition on grape leaves using an LBI system. The leaf area, mean intensity per pixel in the red channel, and droplet count using information from the green channel were extracted from the scattering images. The study employed a generalized additive model (GAM) to predict leaf wetness with the extracted features. The prediction of the test dataset achieved an R-squared value of 0.78. The extraction of image features was found to be influenced by factors such as image resolution and leaf orientation. The method introduced in this study offers the potential for precise quantification of leaf wetness with an LBI system.

In conclusion, our study highlights the importance of considering cell size in agricultural applications of LBI. Besides, LBI was found useful in monitoring plant oil sedimentation and quantifying leaf wetness. This suggests its potential for scenarios involving state changes in suspensions or colloids and differentiating materials with distinct optical properties. However, using a porous matrix as a model introduces an inherent error. Additionally, advancements are necessary to transition the application studies into practical use. Future LBI development could be facilitated by building a comprehensive database on light interactions with diverse cells and tissues.

# Zusammenfassung

Nicht-destruktive optische Sensortechnologie (NDOST) ist ein wesentlicher Bestandteil der Landwirtschaft. Die einzigartigen Fähigkeiten des Lasers haben die NDOST deutlich verbessert. Laser-Rückstreuung (LBI) ist eine Technologie, die Lichtmuster erfasst, die von einem Material gestreut werden, um dessen Eigenschaften zu analysieren. Sie eignet sich besonders für die Landwirtschaft aufgrund ihrer Erschwinglichkeit und der optischen Streueigenschaften landwirtschaftlicher Produkte. Die von der LBI erzeugten Bilder hängen mit den optischen Parametern der untersuchten Objekte zusammen. Wesentliche Aufgaben bei der LBI sind die Auswahl eines geeigneten Lasers, die Extraktion von Bildmerkmalen und die Verwendung eines Vorhersagemodells zur Analyse. Die LBI wurde in zahlreichen Szenarien eingesetzt, wie beispielsweise zur Reifeerkennung und Trocknungsüberwachung. Die Haupt Herausforderungen für die LBI bestehen darin, einen genauen theoretischen Rahmen zu etablieren und neue Anwendungen in der Landwirtschaft zu entdecken. Diese Studie zielt darauf ab, das Grundlagenwissen über LBI zu vertiefen und zusätzliche Anwendungsszenarien zu erforschen.

Die erste Studie konzentrierte sich auf die Grundlagenforschung über LBI. Derzeit dokumentieren Forscher selten die Zellgröße ihrer Proben und behandeln den optischen Koeffizienten als Konstante innerhalb landwirtschaftlicher Produkte, was fragwürdig ist. Ziel dieser Studie war es, Glasfiltermatrizen als kontrollierte Modelle zu verwenden und die Auswirkungen von Porengröße, verschiedenen Lösungsmitteln, Konzentrationen und Wellenlänge zu bewerten. Die verwendeten porösen Glasplatten hatten Porendurchmesser von 1 bis 160  $\mu\text{m}$ . Wir verwendeten wässrige Lösungen von NaCl (0, 1, 2, 3 und 4 mol/L) und  $\text{NaH}_2\text{PO}_4$  (0, 0.8, 1.6, 2.4 und 3.2 mol/L) um die Poren zu füllen. Das LBI-System integrierte Lasermodule mit drei verschiedenen Wellenlängen (405, 635, 780 nm). Die Ergebnisse zeigten, dass drei der vier untersuchten experimentellen Faktoren (der Porendurchmesser, die Lösungsmittel und ihre Konzentrationen) einen erheblichen Einfluss auf LBI haben. Es wurden jedoch keine klaren Unterschiede in den LBI-Mustern zwischen den drei verwendeten Wellenlängen festgestellt. Daher ist bei der Anwendung von LBI auf Früchte beispielsweise eine gründliche Berücksichtigung der Zellgrößen in verschiedenen Tiefen von der Fruchtoberfläche erforderlich.

Die zweite Studie konzentrierte sich auf ein mögliches Anwendungsszenario von LBI: den Sedimentationsprozess von rohem Sesamöl. Die Ölsedimentation ist ein Prozess, bei dem die Schwerkraft genutzt wird, um feste Verunreinigungen zu entfernen, was zu einem klareren Öl führt. Diese Studie untersuchte den Sedimentationsprozess in rohem Sesamöl mit Hilfe von LBI. In-situ- und Laborversuche wurden über 30 Tage durchgeführt, wobei ein LBI-System direkt an einen transparenten Sedimentationstank mit 120L Rohöl angeschlossen war. Sowohl die Öleigenschaften als auch die Sedimentationskurve wurden zusammen mit den LBI-Bildern analysiert. Es gab einen starken Rückgang der ölpartikelbezogenen Eigenschaften (mindestens 87%), einen Rückgang des Wassergehalts um 90% und geringfügige Veränderungen der oxidationsbezogenen Eigenschaften. Die Sedimentationsgeschwindigkeit betrug etwa  $-7$  mm/h und wurde dann weniger als  $-2$  mm/h, was auf zwei Phasen hinweist: verdünnte und gehemmte Sedimentation. Die Oberfläche des rohen Öls zeigte einen ausgeprägten Streufleck und einen Tyndall-Effekt im Öl, der eine zunehmende Weglänge zeigte, während die Sedimentation fortschritt. Die Ergebnisse bieten praktische Einblicke für die Verbesserung des Sedimentationstanks und des LBI-Systemdesigns.

Die dritte Studie konzentrierte sich auf ein weiteres mögliches Anwendungsszenario von LBI: die Messung der Blattnässe. Blattnässe spielt eine entscheidende Rolle bei der Bekämpfung von Pilzkrankheiten bei Pflanzen. Bestehende optische Techniken kategorisieren Blattnässe als ein binäres Problem – entweder nass oder trocken. Im Gegensatz dazu entwickelte diese Forschung eine Plattform, die in der Lage ist, die Tropfenablagerung auf Weinblättern mit einem LBI-System halbautomatisch zu messen. Die Blattfläche, die durchschnittliche Intensität pro Pixel im roten Kanal und die Tropfenzählung anhand von Informationen aus dem grünen Kanal wurden aus den Streubildern extrahiert. Die Studie verwendete ein generalisiertes additives Modell (GAM), um die Blattnässe mit den extrahierten Merkmalen vorherzusagen. Die Vorhersage des Testdatensatzes erreichte einen R-Quadrat-Wert von 0,78. Es stellte sich heraus, dass die Extraktion von Bildmerkmalen von Faktoren wie Bildauflösung und Blatorientierung beeinflusst wurde. Die in dieser Studie vorgestellte Methode bietet das Potenzial für eine präzise Quantifizierung der Blattnässe mit einem LBI-System.

Abschließend betont unsere Studie die Bedeutung der Berücksichtigung der Zellgröße bei landwirtschaftlichen Anwendungen von LBI. Darüber hinaus erwies sich LBI als nützlich bei

der Überwachung der Sedimentation von Pflanzenöl und der Quantifizierung von Blattnässe. Dies deutet auf sein Potenzial für Szenarien hin, die Zustandsänderungen in Suspensionen oder Kolloiden und die Unterscheidung von Materialien mit unterschiedlichen optischen Eigenschaften betreffen. Allerdings führt die Verwendung einer porösen Matrix als Modell zu einem inhärenten Fehler. Zusätzlich sind Fortschritte notwendig, um die Anwendungsstudien in die praktische Anwendung zu überführen. Die zukünftige Entwicklung von LBI könnte durch den Aufbau einer umfassenden Datenbank über Lichtwechselwirkungen mit verschiedenen Zellen und Geweben erleichtert werden.

## Annex 3

### Declaration in lieu of an oath on independent work

**according to Sec. 18(3) sentence 5 of the University of Hohenheim's Doctoral Regulations for the Faculties of Agricultural Sciences, Natural Sciences, and Business, Economics and Social Sciences**

1. The dissertation submitted on the topic

Laser backscattering imaging in agriculture

is work done independently by me.

2. I only used the sources and aids listed and did not make use of any impermissible assistance from third parties. In particular, I marked all content taken word-for-word or paraphrased from other works.

3. I did not use the assistance of a commercial doctoral placement or advising agency.

4. I am aware of the importance of the declaration in lieu of oath and the criminal consequences of false or incomplete declarations in lieu of oath.

I confirm that the declaration above is correct. I declare in lieu of oath that I have declared only the truth to the best of my knowledge and have not omitted anything.

Zhangkai Wu

Stuttgart, 13 October 2023

# Curriculum Vitae

## Zhangkai Wu

Date of birth: 25 October 1990

Place of birth: Hubei Province, China

Nationality: Chinese

Gender: Male

E-mail: zhangkai@uni-hohenheim.de / ziyingsk1025@gmail.com

Address: Institute of Agricultural Engineering, Tropics and Subtropics Group (440e),  
Universität Hohenheim, Garbenstrasse 9, 70599 Stuttgart, Germany

## EDUCATION

**University of Hohenheim** Since 2015  
Stuttgart, Germany  
Institute of Agricultural Engineering, Tropics and Subtropics Group  
PhD candidate

**China Agricultural University** 2012-2014  
Beijing, China  
Degree: Master of Science (M.Sc.) in Agricultural Engineering  
Master's thesis on Design of automatic control system for electric-driven precise seeder in small areas

**China Agricultural University** 2007-2011  
Beijing, China  
Degree: Bachelor of Science (B.Sc.) in Mechatronic Engineering  
Bachelor's thesis on Design of automatic control System for trace-following car



## WORK EXPERIENCE

**Jiangxi Jindatong New Material Technology Co., Ltd**

2021

Jiangxi province, China

Position: Technical Developer

Task: Leading the transformation of a traditional production line into an advanced system. This upgraded production line features automatic image analysis for real-time quality control and performance evaluation

Zhangkai Wu

Stuttgart, 13 October 2023